IMPERIAL

Designing Photocathodes: Ab initio Modelling of the Photoemission Process in Materials for Next Generation Light Sources

Felix Constantin Mildner

Department of Materials
Imperial College London
United Kingdom

Supervisor : Prof. Nicholas M. Harrison

Department of Chemistry
Imperial College London
United Kingdom

Submitted in part fulfilment of the requirements
for the degree of *Doctor of Philosophy*,

13th January 2026

Abstract

Photocathodes are a vital component of free electron lasers (FELs) capable of producing coherent radiation pulses with lengths on the order of femtoseconds (fs). These pulse lengths are a temporal resolution synchrotron radiation light sources can not achieve, allowing measurements of protein dynamics, chemical reactions, electron dynamics and more. Challenges in developing photocathodes for FELs include extending photocathode lifetimes, improving quantum efficiency (QE), lowering emittance and mean transverse energy (MTE), and lowering work functions. While a substantial amount of experimental and theoretical work has been put towards these challenges, they still persist to this day.

Addressing these challenges includes a direct link between the electronic structure of *ab initio* modelled photocathode surfaces and experimentally measured photoemission (PE) spectra. With advances in *ab initio* methods and computing capabilities, modelling photocathode surface structures can now be performed routinely. Therefore, the link from model to experiment can be established by calculating the PE response with an appropriate emission model.

Such PE models exist, but are normally applied to modelled bulk materials. This ignores the effects of surface structures, adsorbates, and contaminants on the PE response. Within this thesis an emission model to calculate the PE spectrum of a surface is developed from previous work. Additional capabilities for angle resolved data are implemented, an approach to calculate the PE of supercell surface models is introduced, and the code implementation is optimised for the efficient modelling of large surface models. The PE spectrums for a series of metallic surfaces and heterogeneous interfaces are calculated. Experimental MTE spectra are compared to the calculated values and detailed atomic and electronic contributions are analysed. The detailed analysis of contributions allows for the linking of modelled electronic structure to experimentally observable changes in the PE spectrum.

Contents

1 Introduction **16**
- 1.1 Free Electron Lasers (FELs) . . . 17
- 1.2 Photocathodes . . . 19

2 Background and Theory **22**
- 2.1 The Energy of Quantum Mechanical Systems . . . 22
  - 2.1.1 The time-independent Schrödinger Equation . . . 22
  - 2.1.2 The Born-Oppenheimer Approximation . . . 22
- 2.2 Solving Schrödinger's Equation for Many Electron Systems . . . 23
  - 2.2.1 Hohenberg-Kohn Theorems and Kohn-Sham Approach . . . 23
  - 2.2.2 Exchange-Correlation Functionals . . . 25
- 2.3 Wavefunctions in Extended Systems : Bloch's Theorem . . . 26
- 2.4 Basis Sets . . . 26
  - 2.4.1 Plane Wave Basis Sets . . . 26
- 2.5 Atomic Pseudopotentials . . . 27
- 2.6 Monkhorst-Pack (MP) and other Grids . . . 28
- 2.7 Densities of States . . . 28
- 2.8 Brillouin Zone Sampling Schemes . . . 30
- 2.9 Modelling Surfaces . . . 30

3 Theoretical Models for Photoemission **32**
- 3.1 3-Step Model . . . 32
- 3.2 Dowell-Schmerge Model . . . 34
  - 3.2.1 Extension of D-S like model to $T > 0\,\mathrm{K}$ . . . 35
  - 3.2.2 DOS dependent 3-Step Model for Disordered Surfaces . . . 36
- 3.3 Emittance Model from individual States . . . 38
- 3.4 1-Step Model . . . 39
- 3.5 Dampened Plane-Wave Model . . . 41

4 The OptaDOS Photoemission Model **43**
- 4.1 Defining the Surface Geometry, Layers, and Work Function . . . 43
- 4.2 Calculating Optical Properties . . . 47
- 4.3 3-Step - Step 1 - Excitation Probability . . . 49
  - 4.3.1 3-Step Excitations . . . 49
  - 4.3.2 Light Polarisation Vector . . . 49
  - 4.3.3 Light Intensity . . . 49
  - 4.3.4 Band Occupations . . . 50
  - 4.3.5 Layer Projection . . . 50
- 4.4 3-Step - Step 2 - Transmission Probability . . . 51
  - 4.4.1 Internal Propagation and Angle . . . 51
  - 4.4.2 Scattering Probability . . . 51
- 4.5 3-Step - Step 3 - Surface Emission . . . 54
  - 4.5.1 External Emission Angles . . . 54
  - 4.5.2 Surface Transmission . . . 55
- 4.6 1-Step Model . . . 56
  - 4.6.1 Excitation and Optical Matrix Elements . . . 56
  - 4.6.2 Propagation, Emission Angle and finite Penetration Depth of Final State . . . 58
- 4.7 Applying Electrical Fields . . . 58
- 4.8 Bulk Approximation . . . 60
- 4.9 Putting it all together: QE and MTE . . . 61
- 4.10 Teasing out the Details: Calculating Angle-Resolved Contributions . . . 62
- 4.11 Calculating Photoemission from Supercell Models . . . 63

5 Photoemission code and modelling **69**
5.1 Discussion of Code Development . . . 69
5.2 The Issue of Convergence . . . 71
5.3 Metallic Surfaces . . . 72
5.3.1 Cu Bulk . . . 72
5.3.2 Cu(100) Surface . . . 74
5.3.3 Cu(110) Surface . . . 80
5.3.4 Cu(111) Surface . . . 84
5.3.5 Ag Bulk . . . 89
5.3.6 Ag(100) Surface . . . 90
5.4 Heterostructures with protective Coatings for Photocathodes . . . 93
5.4.1 MgO Bulk . . . 93
5.4.2 TiN Bulk . . . 94
5.4.3 MgO(100) on Ag(100) . . . 95
5.4.4 MgO(100) on Cu(100) . . . 100
5.4.5 TiN(100) on Ag(100) . . . 104

6 Conclusion **108**
6.1 Further Work . . . 108

References **110**

A Output from a Photoemission Calculation **117**

List of Figures

1.1 Picture of a card showing an illustration by Muybridge of the pictures he took of the horse "Sallie Gardner" galloping. Picture obtained from Library of Congress Prints and Photographs Divisions [4]. 16

1.2 Visualisation of the approximate electron path through an undulator in a free electron laser (FEL). In the bottom left the emission of incoherent radiation from a disordered electron bunch is visualised. In the bottom middle, the emission from coherent micro-bunches is shown. The bottom right gives an approximate curve for the amount of radiated power as a function of the length of the undulator. It takes time, and thus space, for the electron bunch to form the micro-bunches that emit the coherent radiation. This figure is adapted from Figure 1 in [22], and the radiation power curve is adapted from Figure 3 in [23]. 18

2.1 Conceptual representation of the circular dependence of quantities within the Kohn-Sham approach. The Hohenberg-Kohn theorems for a non-interacting system HK_0 allow the calculation of the Kohn-Sham potential V_{KS} from the non-interacting density $n_0(\mathbf{r})$, which acts on each of the single-particle Kohn-Sham equations $\psi_i(\mathbf{r})$, that taken together determine the density of non-interacting particles $n_0(\mathbf{r})$. Adapted from Figure 7.1 in Martin [58]. 25

2.2 left: visualisation of a surface cell with 3-dimensional PBCs applied. The repeated images are indicated by the dotted lines at each corner of the cell. right: Render of a possible SC geometry with one of the surface atoms removed to represent a defective surface. 31

3.1 Visualisation of the emission angles as they are assumed in the Berglund and Spicer 3-step model. θ is the polar emission angle w.r.t. the surface normal and the emission angle ϕ is the azimuthal angle. 32

3.2 A comparison of the MTE curve for three of the discussed emission models. The DOS dependent model was calculated using the DOS from the Cu(100) surface slab model described in Section 5.3.2. Note the discussion on the integral limits for the model by Saha et al. for the DOS dependent model. 38

4.1 Visualisation of the two options for assigning atoms to a set of layers for a MgO on Ag interface slab. The Mg, O, and Ag atoms are coloured light green, red, and grey, respectively. The two implemented approaches are visualised for the slab model and also where they can go wrong. Option 1 takes the *user defined slab top* and *user defined slab bottom* (not shown) as inputs, infers a slab middle and calculates the layer height based on the layer spacing in the middle. This option works well within a homogenous material, as the layers of Ag for option 1 are nicely aligned with atom spacing. At the interface and beyond, however, this spacing does not align any more and the layers of MgO are not well defined by the inferred slab layer height. Option 2 shows the approach of having the user define the boundaries for each of the layers, here the layer height varies slightly, but is able to accommodate both the Ag slab layer height, interface and MgO slab layers. 45

4.2 Exemplary plots used to determine the boundaries from the electronic density (left) and and WF from the one electron potential and E_F (right) for a Cu(100) surface slab with 16 layers. 46

4.3 Comparison of three different approaches to describe the scattering probability of an electron propagating through Cu. The orange TPP-2M[126, 127] curve clearly shows a severe underestimation of the expected IMFP values, while the curve by Nagy and Echenique [128] shows much more reasonable IMFP values. The constant approach is a very easily usable, but misses the energy dependence of the IMFP, as can be seen from the changing difference between the constant and Nagy-Echenique-curve. 54

4.4 Diagram of the electron momenta during propagation and after emission from the surface. The transverse momentum is conserved while passing from the cathode into the vacuum. The momentum along z is diminished when the electron looses the energy of the WF. Hence the internal propagation angle $\vartheta_{internal}$ is smaller than the emission angle $\vartheta_{external}$ w.r.t. the surface normal. Based on Figure 6.5 in the book "Photoemission Spectroscopy" by Hüfner [131]. 55
4.5 Plot showing the Schottky-Nordheim barrier's shape as a function of distance from the surface z at different field strengths. The gradual lowering of the barrier height with increasing field strength and alteration to the barrier shape are evident. . . . 59
4.6 Visual explanation for band folding using a single hypothetical band. left: In the primitive cell (PC) with side length a the periodicity of the band and the reciprocal cell are identical and a single band exists in the Brillouin zone (BZ). right: With a 2x supercell of side length $2a$ the reciprocal cell is halved, but the band retains its original periodicity. The bands from the other BZs move into the first BZ and the band appears to be *folded* towards the origin Γ. 64
4.7 Absorption coefficient curves for a Cu(100) PC and 2×2 SC. The curves are nearly identical until they start to diverge due to the lower upper bound for the SC system. This has an effect on lower energies due to the Kramers-Kronig relation used to calculate ε. 64
4.8 Visualisation of the Gkgrid contributions for each point in Cartesian coordinates for the bands in Table 4.2. The red box shows the reciprocal cell size for the PC. The pattern of higher and lower contributions aligns very well with the *folded* and *non-folded* band classification in Table 4.2. Since it is a 2×2 SC, the folded states originated from the edge of the PC BZ, which means, that the high contribution points now correspond to $\mathbf{G} = (N, N, N)^T \in [1, 3, 5, \ldots]$ in fractional coordinates. A non-folded band has the highest contribution for $\mathbf{G} = \vec{0}$ and the other higher contributions are located at $\mathbf{G} = (N, N, N)^T \in [2, 4, 6, \ldots]$ in fractional coordinates. 67
4.9 left: The entire set of $\mathbf{G}$+$\mathbf{k}$-grid points with $\vec{k} = \vec{0}$ for a Cu(100) cell with some points in the Z direction not shown for visual clarity. See Section 5.3.2 for exact cell size of Cu(100) surface. right: Set of $\mathbf{G}$+$\mathbf{k}$-grid points after summing all contributions with the same $\mathbf{G}_{x,y}$ coordinates. The selection zone has the lateral size of 3.799 $^1/\text{Å}$, corresponding to 55 eV of transverse energy. The extra points outside the selection zone are chosen to account for any possible offset due to the $\mathbf{k}$ point vector when creating the $\mathbf{G}$+$\mathbf{k}$-grid. The not included points have such a high transverse momentum, that they would not be able to contribute unless one calculates PE with photon energies beyond the UPS range. 68
5.1 Bandstructure plot for two Cu(100) surface models with 16 layers of Cu atoms and varying amounts of vacuum in between periodic images. The equal dispersion for the Cu based is evident and the notable change of the number of parabolic bands around Γ is notable. 71
5.2 Calculated band structure and DOS for the bulk fcc Cu structure. 73
5.3 Photoemission response calculated for a Cu(100) 16 layer slab using the 3-step and 1-step models. The energy axis is shown as both photon energy (top) and excess energy above the WF (bottom). The comparison with the extended DS model [95], as well as experimental data measured using the TESS instrument [151, 152] shows very good agreement in the comparable range. The varying oscillations in both curves can be attributed to discrete states rather than a continuum contributing to the calculated photoemission response. 75
5.4 Calculated band structure for the Cu(100) 16 layer slab and the corresponding DOS; the red dashed lines indicate the Fermi energy. 76
5.5 Broadened 3-step emissions for 4.60 eV and 5.30 eV showing the kinetic energy vs transverse momentum distribution. The first emission contributions near threshold originate from a state crossing the Fermi energy away from the origin, resulting in a high MTE value at threshold. At a higher energy of 5.3 eV, further states are able to contribute to the emission, lowering the calculated MTE value. 76

5.6 Calculated PE spectra for a Cu(100) surface with 16 and 64 layers. Both spectra show much smaller oscillations for the 64 layer model, but the QE spectrum appears to be suppressed for the 64 layer model. 77
5.7 Comparison of calculated PE curves for a Cu(100) 1x1 slab and a 2x2 SC of this exact same structure using both available momenta schemes. Comparing the `crystal` curves, it is evident that this approach fails to give comparable results. The `Gkgrid` approach, on the other hand, gives nearly identical QE and MTE values, although the values are changed compared to the `crystal` scheme. 78
5.8 Broadened 3-step emissions for 16 eV showing the kinetic energy vs transverse momentum distribution for the `crystal` (top) and `Gkgrid` (bottom) momentum options. The section of missing data in the left panel of both is due to the symmetry reduction of the MP grid. Reconstruction for the full MP grid has not yet been implemented for the kinetic energy vs transverse momentum map. 78
5.9 Constant binding energy maps for Cu(100) surface with a binding energy broadening of 0.026 eV. left: map using the *crystal* momentum scheme, showing the circular features for the parabolic bands near the origin and the flat bands near the edge of the BZ. The outer edges align with the edges of the BZ. The MP grid only extends to the outer edges of the BZ, so no calculated emission outside of these is expected. right: map using the *Gkgrid* momentum scheme, but the overall emission intensity is slightly reduced. The same features as in the *crystal* scheme case are present within the BZ boundaries. Furthermore, the emissions extend outside the first BZ, since the MP grid is extended for the *Gkgrid* momentum scheme, so this behaviour is as expected. 79
5.10 Photoemission Response calculated for a Cu(110) 16 layer slab using the 3-step and 1-step models. The energy axis is shown as both photon energy (top) and excess energy above the WF (bottom). The comparison with the extended DS model [95], as well as experimental data measured using the TESS instrument [151, 152]. The strong calculated 1-step MTE response can be attributed to flat states contributing early, see Figure 5.13 for map showing the 1-Step model emissions near threshold. The 3-step model shows a more comparable response until it starts deviating above ≈ 5.3 eV, but has very good agreement above ≈ 7 eV. 81
5.11 Calculated band structure and DOS for the Cu(110) 16 layer slab, the red dashed line indicates the Fermi energy. 82
5.12 Broadened 3-step emissions for Cu(110) at 4.65 eV and 5.10 eV showing the kinetic energy vs transverse momentum distribution. The first emission contributions originate from a flat state lying below the Fermi energy, which explains the onset of emission away from the threshold energy. At higher energies, more of the same state can contribute and a second state near the Fermi energy can contribute. . . . 82
5.13 Broadened 1-step emissions for Cu(110) at 4.40 eV and 5.10 eV showing the kinetic energy vs transverse momentum distribution. The first emission contributions originate from a flat state lying above the Fermi energy, which explains the onset of emission below the threshold energy. Further the high calculated MTE value at threshold is associated with emissions from states away from the Γ point. 83
5.14 Constant binding energy maps for Cu(110) surface with a binding energy broadening of 0.026 eV. left: map using the *crystal* momentum scheme, The MP grid only extends to the outer edges of the BZ, so no calculated emission outside of these is expected. The orthorhombic shape of the BZ is evident. right: map using the *Gkgrid* momentum scheme. The same features as in the *crystal* scheme case are present within the BZ boundaries, but the overall emission intensity is slightly reduced. Furthermore, the emissions extend outside the first BZ, since the MP grid is extended for the *Gkgrid* momentum scheme, so this behaviour is as expected. 83
5.15 Calculated band structure and DOS for the Cu(111) 16 layer slab, the red dashed line indicates the Fermi energy. 85

5.16 Photoemission Response calculated for a Cu(111) 16 layer slab using the 3-step and 1-step models. The energy axis is shown as both photon energy (top) and excess energy above the WF (bottom). The comparison with the extended DS model [95], as well as experimental data measured using the TESS instrument [151, 152] shows acceptable agreement for the comparable range for the 3-step model. The 1-step model has a very strong MTE response, which can be attributed to the low contributions from states away from the Γ point. The varying oscillations in both curves can be attributed to discrete states rather than a continuum contributing to the calculated photoemission response. 86
5.17 Broadened 1-step emissions for Cu(111) at 4.80 eV and 5.60 eV showing the kinetic energy vs transverse momentum distribution. The first calculated 1-step emissions are low intensity of emissions above the Fermi energy. This correlates with the high MTE value near threshold. At the higher energy the first parabolic state can fully contribute and a second state is also able to contribute. 87
5.18 Broadened 3-step emissions for Cu(111) at 4.90 eV and 5.50 eV showing the kinetic energy vs transverse momentum distribution. The first calculated 1-step emissions are low intensity of emissions above the Fermi energy. This correlates with the high MTE . At the higher energy the first parabolic state can fully contribute and a second state is also starting to contribute. 87
5.19 Constant binding energy maps for Cu(111) surface with a binding energy broadening of 0.026 eV. left: map using the *crystal* momentum scheme. The MP grid only extends to the outer edges of the BZ, so no calculated emission outside of these is expected. The hexagonal shape of the BZ is evident. right: map using the *Gkgrid* momentum scheme. The same features as in the *crystal* scheme case are present within the BZ boundaries, but the overall emission intensity is slightly reduced. Furthermore, the emission extends outside the first BZ, since the MP grid is extended for the *Gkgrid* momentum scheme, so this behaviour is as expected. 88
5.20 Calculated bulk Ag band structure and bulk DOS. The very sharp "peak" at 7 eV is due to the gradient dependent broadening scheme. The large set of flat bands across the BZ create this "peak", which should not be as prominent with a constant width broadening scheme. 89
5.21 Calculated band structures for the Ag(100) layer slab with the lattice parameters of TiN and MgO. The different amount of stretch shows up in slightly different band energies around the Γ point. 91
5.22 Calculated QE and MTE curves for different cell sizes and thus strain for a 16 layer Ag(100) slab. The late onset of the MTE and QE values is associated with the slightly different energies of states near the Fermi energy located at the Γ. The TiN cell structure has a band directly on the Fermi energy, while the MgO cell structure has the band dip just below the Fermi energy. See Figure 5.21 for more details. . . 91
5.23 Constant binding energy maps for Ag(100) surface using the unstrained cell with a binding energy broadening of 0.026 eV. The map uses the *crystal* momentum scheme. Since the MP grid of **k** points only extends to the outer edges of the BZ, no calculated emission outside of these is expected. The tetragonal shape of the BZ is evident. 92
5.24 Band structure and DOS for the MgO bulk structure. The band gap is a direct gap of 4.452 eV at the Γ point. The very sharp peaks around 4.5 eV, 7.5 eV and 9.8 eV are due to the gradient dependent broadening. The flat band sections in the BZ at these energies cause the broadening of these contributions to become as tight as possible, representing these peaks. 94
5.25 Band structure and DOS for the TiN bulk system. 95
5.26 Calculated QE and MTE curves for the bare Ag(100) surface compared to the interface structure with one, two, and six layers of MgO on both surfaces. The large MTE jumps for the MgO interfaces at ≈ 2.9 eV are quite prominent. For more detailed contributions see Figure 5.28 for specific state contributions. 97

5.27 Layer QE contributions for 16L Ag(100)/6L MgO interface structure. A clear distinction in the response curve exists and the rule, that the more outer layers contribute more, holds true. Interestingly the MgO layers contribute the majority of QE above $\approx 5\,\text{eV}$, while the Ag metal layers do this below this photon energy. . . . 97
5.28 Emission Maps of $E_{kinetic}$ vs $p_{\parallel}$ at energies representative of the large peak in the MTE curve for the 6L MgO(100)/16L Ag(100) model. The parabolic state on the right hand side is starting to emit around 4.7 eV and at 4.85 eV it is able to fully emit. This drastically increases the calculated MTE, as there is little emission around Γ. Once 5.05 eV are reached, however, the flat bands a near Γ are able to emit, which dramatically lowers the MTE, as now a large part of the emission is from near Γ. . 98
5.29 Calculated band structure and DOS for the 16L Ag(100)/6L MgO(100) on both surfaces. 99
5.30 left: Render showing the top half of the Cu(100)/MgO(100) interface supercell. right: Top view of the Cu(100) substrate supercell. 100
5.31 PDOS contributions broken down by layer. The innermost Cu layer shows good reproduction of the bulk DOS, while the inner MgO layers never reach good reproduction of the DOS. The number of MgO layers was informed by the collaborators providing the measurements. 101
5.32 Comparison of QE and MTE curves for the bare Cu(100) supercell structure and the interface with 10L Cu/6L MgO, as well as the extended DS model and a set of experimental measurements using the TESS instrument [151, 152]. There is good agreement above $\approx 3.7\,\text{eV}$ for the rest of available experimental data. 102
5.33 Layer based QE contributions. The general rule that layers further out towards the surface, holds true here. Furthermore a distinct structure between the two materials and their response curves is visible, which is to be expected for two materials with very different electronic structure (metal vs semiconductor/insulator. 103
5.34 Calculated band structure for 16L Ag(100)/6L TiN(100) interface slab and the DOS for the structure. 105
5.35 Layer QE contributions for the 16L Ag(100)/7L TiN(100) interface. The PE response is stronger from the TiN layers, but the difference is not as stark, as the metal/insulator case in Figure 5.27. 106
5.36 Calculated QE and MTE curves for the Ag/TiN interfaces. 106

List of Tables

1.1 Table of data on the different materials used in photocathodes. 20
4.1 Expansions coefficients given by Forbes and Dean [139] for the series to approximate the function $v(l')$. The expansion to the fourth degree is used to calculate the tunnelling properties in this work. 60
4.2 Table showing the band energies at the Γ point, a determination of whether the band is folded, and applicable optical matrix elements for a Cu(100) primitive cell (PC) and 2x2 supercell (SC) structure. The band energies of equivalent bands are within 20 meV between the PC and SC structures. The OMEs for equivalent excitations for both PC and SC are within 10 %. The OME for an excitation between two folded states in the SC is of similar magnitude as the OME for an excitation between two non-folded states. The excitations for SC bands that are dissimilar are at least seven orders of magnitude smaller than for the similar SC bands. All taken together this shows, that the band energies and OMEs are consistent between PC and SC structures, and that the excitations between dissimilar states are small enough to be negligible. 65
5.1 Table showing the calculated WFs and surface energies for different amounts of strain. The surface energy is calculated using Equation (5.1). 90
5.2 Table showing the calculated WFs and surface terminations for the different numbers of MgO(100) layers on a Ag(100) substrate. The adhesion energy for the interfaces is calculated using the formula provided by Shan et al. [179]. The adhesion energy for 3 MgO layers is likely incorrect, which is likely due to difficulty during the optimisation of the 3 layer MgO slab. 96
5.3 Table showing the calculated WFs and surface terminations for the different numbers of MgO(100) layers on a Cu(100) substrate. The adhesion energy for the interfaces is calculated using the formula provided by Shan et al. [179] 101
5.4 Table showing the calculated WFs and interface formation energies for TiN(100) layers on a Ag(100) substrate. The adhesion energy for the interfaces is calculated using the formula provided by Shan et al. [179] 105

Acknowledgements

The last four years have gone by so fast and yet October 2021 feels like a lifetime ago. I have had the pleasure to meet so many people and it would take too long to say thanks to every person who contributed in large or small to the success of this PhD. So I will limit myself to thanking those who played a particularly important role in helping me reach this milestone.

I want to thank my supervisor and mentor Prof. Nicholas M Harrison for all the support during this time. I have greatly enjoyed our meetings filled with excitement, intense head scratching over graphs and numbers, and insightful discussions. Thank you for your guidance and feedback!

Thank you as well to my predecessors Bruno Camino and Victor Chang, who both laid the foundation for my work. It was great and sometimes frustrating to find the solution to problems I had been bashing my had against just written out in your theses and papers.

Thank you to all the Harrison group members and other colleagues throughout these years. Thank you to Frederik, Rashid, James, Fei, Huanyu, Kipras, Xinyue and Ayse for the extended lunch discussions, movie nights, attempts to house unicorns, bao making instructions, and general friendship. It was incredible to have you all as colleagues and I am excited to see where in the world we all end up.

Thank you to Dr Giuseppe Mallia for supporting me, helping out countless times during my time at Imperial, and thank you for putting up with my late night report corrections.

This project has been a collaboration with the Photocathodes Group within ASTeC at the STFC Daresbury laboratory. A big thank you Dr. Tim Noakes, Dr. Lee Jones, Dr. Christopher Benjamin, Mr. Hugh Churn and Mr. Dominic Sterland. Thank you for the many discussions, providing the experimental data and experimentalist's perspective to this project, trips to conferences and workshops, hosting for my research stay at the lab, and finally the funding support that made this project possible in the first place.

Thank you to the entire CDT in Advanced Characterisation of Materials (CDT EPSRC and SFI Centre for Doctoral Training in Advanced Characterisation of Materials Grant Ref: EP/S023259/1) for all the support and good times, whether it was Christmas gatherings, summer schools, research updates, or career talks. And thank you to my fellow Cohort 8 members. It has been a blast with you all throughout these years!

A big thank you to my parents, sister and extended family. Thank you for detailed technical discussions, guidance, interest in my work, and random cat pictures. I would not have gotten to this point without your support throughout all these years.

And finally a very special thank you to Margherita for putting up with my late night coding sessions, going on hiking adventures and walks along the Thames with me, making our little Victorian château a home, and your incredible support in the last weeks of writing this thesis. It would not have been possible without you and I am so thankful to have had you by my side for the last 3.5 years and counting!

Publications

Publications based on this work:

F. Mildner, V. Chang, B. Camino, N.M. Harrison, 'OptaDOS photoemission module: A tool for simulating angle-resolved photoemission from electronic structure surface simulations', In preparation

C. Benjamin, H.M. Churn, F. Mildner, L.B. Jones, N.M. Harrison, T.C.Q. Noakes, C.R. Bell, 'Enhanced performance of an Cu(100) photocathode by an ultra-thin MgO film', In preparation

Presentations

TALKS

Cockcroft Institute Postgraduate Research Conference, Cockcroft Institute for Accelerator Science, STFC Daresbury Laboratory, November 2022

EMRS Spring Meeting 2023, European Materials Research Society, May 2023

CDT Summer School 2023, Centre for Doctoral Training in Advanced Materials Characterisation, June 2023

European Workshop on Photocathodes for Particle Accelerator Applications (EWPAA) 2024, Helmholtz Zentrum Dresden Rossendorf, September 2024

CDT Advisory Board Meeting, Centre for Doctoral Training in Advanced Materials Characterisation, University College London, October 2024

TYC Postgraduate Day 2025, Thomas Young Centre, Queen Mary University London, June 2025

CDT Summer School 2025, Centre for Doctoral Training in Advanced Materials Characterisation, July 2025

POSTERS

CDT Summer School 2022, Centre for Doctoral Training in Advanced Materials Characterisation, July 2022

Photocathode Physics for Photoinjectors Workshop (P3) 2023, Stony Brook University, October 2023

TYC Postgraduate Day 2024, Thomas Young Centre, Imperial College London, May 2024

CDT Summer School 2024, Centre for Doctoral Training in Advanced Materials Characterisation, July 2024 (Awarded "Outstanding Poster Award")

Statement of originality

The research presented in this thesis is my own work and all additional sources of information have been appropriately referenced. Information derived from sources such as books, published or unpublished work of others, and Internet sources have been acknowledged in the text and the list of references is given in the bibliography.

The research presented in this thesis was conducted under the supervision and guidance of Professor Nicholas M. Harrison at Imperial College London.

Felix Constantin Mildner

13th January 2026

Copyright Declaration

The copyright of this thesis rests with the author. Unless otherwise indicated, its contents are licensed under a Creative Commons Attribution-Non Commercial 4.0 International Licence (CC BY-NC).

Under this licence, you may copy and redistribute the material in any medium or format. You may also create and distribute modified versions of the work. This is on the condition that: you credit the author and do not use it, or any derivative works, for a commercial purpose.

When reusing or sharing this work, ensure you make the licence terms clear to others by naming the licence and linking to the licence text. Where a work has been adapted, you should indicate that the work has been changed and describe those changes.

Please seek permission from the copyright holder for uses of this work that are not included in this licence or permitted under UK Copyright Law.

List of Acronyms

ARPES angle-resolved photoemission spectroscopy

AO atomic orbital

BZ Brilluoin zone

DFT density functional theory

DOS density of states

FEL free electron laser

GGA generalized gradient approximation

HF Hartree-Fock

IMFP inelastic mean free path

IR infrared

JDOS joint density of states

KS Kohn-Sham

LASER light amplification by stimulated emission of radiation

LCAO linear combination of atomic orbitals

LDA local-density approximation

LINAC linear accelerator

MP Monkhorst-Pack

MTE mean transverse energy

PBC periodic boundary conditions

PE photoemission

PES photoemission spectroscopy

PDOS projected density of states

PSP pseudopotential

PW plane-wave

QE quantum efficiency

RPA random phase approximation

SCF self-consistent field

SASE self-amplifying spontaneous emission

UHV ultra high vacuum

UPS ultraviolet photoelectron spectroscopy

USP ultrasoft pseudopotential

UV ultraviolet

WF workfunction

XRD X-ray diffraction

1 Introduction

During the development of photography in the 19^{th} and 20^{th} century the length of time it took to take a picture had been a central issue. From the time a Daguerreotype took 40 s to 90 s of exposure [1] to Eadweard Muybridge taking pictures fast enough to show the movement steps of galloping horses [2] many improvements were made to the tools and processes to bring down the necessary exposure time. An image of the famous sequence is shown in Figure 1.1. Nowadays there are slow motion cameras capable of taking more than 1,000,000 frames per second[3].

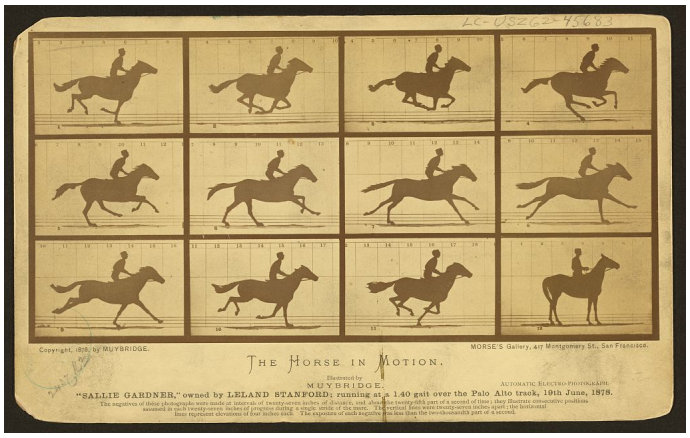


Figure 1.1: Picture of a card showing an illustration by Muybridge of the pictures he took of the horse "Sallie Gardner" galloping. Picture obtained from Library of Congress Prints and Photographs Divisions [4].

Connected to the speed of taking a picture is the need for enough light to get a useable image. This is shown intuitively in a letter to the *The Spectator*[1] as the Daguerreotype needs much longer exposures in the fall compared to the summer. With the slow motion cameras of today bright lights are necessary. Also for experimental research the brightness of a light source used is of fundamental importance to taking a picture and in many cases a limiting factor. In this context, though, the concept of "picture" has to be considered more broadly as a set of signals. It can be a X-ray diffraction pattern of a protein [5], an emission or absorption spectrum [6], or photoemitted electrons and their interaction with adsorbates [7].

For all of these applications the amount of light produced by the illuminating light source are essential, as well as the length of the illumination pulse. If the light pulse is not bright enough, the resulting signal is not high enough, i.e. low signal to noise ratio (SNR). If the pulse of light is bright enough, but too long in time, the temporal dimension is washed out. Just like taking a long exposure picture of a fast moving object. With a short bright pulse the amount of light is high enough to get a good SNR with good temporal resolution. The ideal light source for these requirements is the free electron laser (FEL). Light pulses on the order of fs can be produced by FELs [6, 7]. This allows the measurements listed above and many more to be done at previously unattainable temporal resolution.

FELs create the light using a packet of electrons, which is accelerated in a linear accelerator (LINAC) to relativistic speed. The packet originates from the so-called "gun" containing the photocathode. The FEL uses magnetic fields at the end of the LINAC to accelerate them back and forth. This is the main principle of light creation in FELs, since the acceleration of charged particles always creates electromagnetic radiation [8], i.e. light. In addition the light is normally coherent, making it like a laser, if the electron packets are bunched up tight enough. A more detailed discussion can be found in Section 1.1. This necessity for tight electron packets is the

reason a FEL needs to use a photocathode as a source of the electrons.

The photocathode is the part of an FEL, which will be the focus of this work. This component is the subject of a lot of research work, as the performance of the FEL can be severely limited by the emission characteristics of the cathode and the cathode's lifetime. The focus points of this research effort are described by a number of different studies [9, 10] as the following:

- using material and surface diagnostics to determine the optimal construction methods and emission characteristics;
- modelling of emission process and the dynamics of emitted electrons;
- testing of operational gun and injector systems to validate models;
- engineering the surface and the connected electronic structure of the photocathode material;
- (automated) screening for new photocathode materials.

This thesis will be focussing on the second point. A photoemission (PE) model paired with *ab initio* electronic structure theory is used to calculate the photoemission response for surface models. Through this the specific surface structure and its chemical environment can be linked to changes in the corresponding PE intensity vs energy spectrum. This creates a more direct connection between the specific features in the electronic structure and their influence on the PE response. This informs choices for surface modifications or other approaches to increase cathode performance.

Within this thesis the general working principles of FELs and photocathodes are introduced, the theory used to model the surfaces using DFT is discussed and different approaches to modelling the photoemission process will be reviewed. The specific photoemission model, developed by previous works[11, 12] and within this work, will be introduced in detail and finally the application of the model will be shown on metal surfaces and heterostructure interfaces.

1.1 Free Electron Lasers (FELs)

As discussed above the FEL is the solution to the need for very short high intensity light sources. The idea to use electrons at relativistic speeds to generate radiation/light was published by Motz [13] in 1951 and the idea of an FEL was published by Madey [14] in 1971. Since then a lot of effort has gone into creating FELs for radiation ranging from THz [15], infrared (IR) [16] to X-rays [17].

The relativistic electrons going through a FEL are made up of electron bunches emitted from a source, i.e. the photocathode, into the initial part of the LINAC, called the gun. A bunch represents a single packet of electrons created by a short emission from the photocathode in the electron source, which is later used to create a single light pulse at the end of the FEL. The number of electrons and thus the bunch charge is dependent on the specific setup and requirements of the FEL. The literature stated values for X-ray FELs are in the range of 10 pC to 100 pC, which equals 6×10^7 to 6×10^8 electrons per bunch [18] or even up to 1 nC at the FLASH FEL facility [19]. Other applications of such electron bunches, such as ultrafast electron diffraction (UED), use much smaller bunches of 10 fC to 100 fC [18, 20], equal to 6.2×10^4 to 6.2×10^5 electrons, to retain spacial and temporal coherence during each diffraction event. The electron bunches are initially accelerated using either radio-frequency (RF) [17] or through an applied electric field, also called direct-current (DC) [21]. These give an initial boost to the electron packets, which are then further accelerated in the LINAC and sent into the portion creating the light, also called the undulator. Figure 1.2 shows a visualisation of the electron path in the undulator and how the emission of coherent radiation and emitted power is intimately linked to the formation of micro-bunches.

The rapidly switching magnetic field causes the electrons to 'undulate' back and forth in a sinusoidal pattern, emitting light whenever the electrons are accelerated [17]. This is not the first type of light source using the undulator to create radiation from relativistic electrons. In 3^{rd} generation light sources the undulator is used with bunches of relativistic electrons, but is much shorter [22].

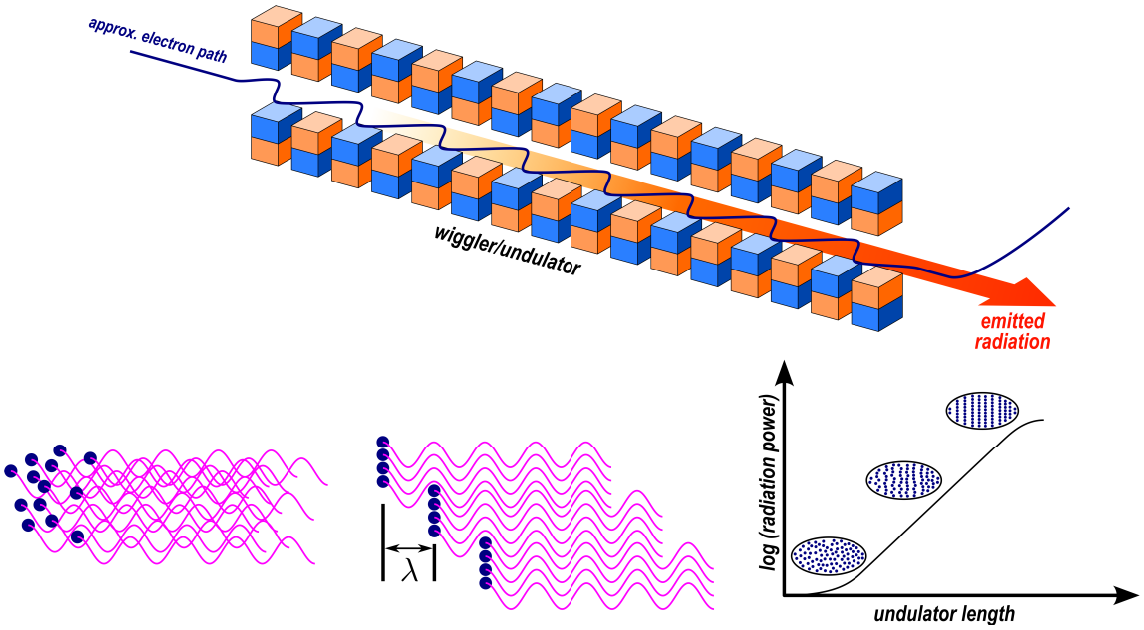


Figure 1.2: Visualisation of the approximate electron path through an undulator in a free electron laser (FEL). In the bottom left the emission of incoherent radiation from a disordered electron bunch is visualised. In the bottom middle, the emission from coherent micro-bunches is shown. The bottom right gives an approximate curve for the amount of radiated power as a function of the length of the undulator. It takes time, and thus space, for the electron bunch to form the micro-bunches that emit the coherent radiation. This figure is adapted from Figure 1 in [22], and the radiation power curve is adapted from Figure 3 in [23].

Compared to 3^{rd}-generation light sources the undulators in FELs are up to an order of magnitude longer [22]. This has the effect that the electron bunch and emitted light travel together through the undulator and interact [17]. The interaction of the electromagnetic radiation with the electrons causes the electron bunch to further subdivide into sub-bunches spaced out by the wavelength λ of the emitted light. This aligns the phase of all further emitted light, making it coherent, just like laser light. A visual representation of the process and the resulting light intensity plot is shown in Figure 1.2.

In the FEL the electrons are the medium, having stored a lot of energy, emitting the coherent light. In other types of lasers, the medium can be made of crystals like neodymium doped yttrium aluminium garnet (Nd:YAG) [24], gases like Krypton and Fluorine (KrF) [25] or even organic dyes [26]. The use of relativistic electrons as the lasing medium allows for much better control of the emitted light by varying the electron bunches' energy in the LINAC, using undulators with different periodicities or sending in a seeding light pulse to stimulate the emission of that specific wavelength of light [22].

If no seeding light pulse is used, the FELs light pulse is generated by a process called self-amplifying spontaneous emission (SASE) [17], which gives a more broad spectrum light pulse. This is due to slight differences in electron energies at the beginning of the undulator, all giving slightly different emission wavelengths [22]. The seeding technique gives FEL light with a much tighter set of wavelengths, but at the cost of needing more equipment to generate the seeding pulse. This is of course difficult to do if the desired emission wavelengths are beyond the range of easily accessible wavelengths, which can also be handled by mirrors and other optical equipment, such as X-rays.

This is one of the reasons it is more difficult to build a FEL capable of creating X-rays. Furthermore, the requirements for the electron packets become much more stringent with decreasing

wavelengths [17]. This means only a small number of X-ray FELs (XFELs) have become operational up until now, such as the FLASH facility at DESY in Hamburg, Germany [27], European XFEL [28] in Hamburg, Germany, LCLS at SLAC National Accelerator Laboratory in Stanford, US [29], and the SACLA facility in Harima Science Park City, Hyogo Prefecture, Japan [30].

These stringent requirements for the electron bunch characteristics require careful optimisation and improvements to the photocathode and all other parts of the FEL. As stated above, this work is specifically aims to contribute to the advancement of photocathode. The kinds of photocathodes currently used in FELs and their characteristics, as well as metrics by which to judge photocathodes are explored in the next section.

1.2 Photocathodes

As set out in the previous section the requirements for the electron packets used in FELs, especially in the soft and hard X-ray regime, are quite stringent. Following from this the characteristics of the cathode are of high importance to advancing the capabilities and usage as a tool for novel research regimes. To meaningfully define the performance of a cathode, specific metrics need to be defined. The most important of these metrics among many others as defined by Musumeci et al. [10] and Todd [31] are:

- **quantum efficiency** (QE) : the QE of a photocathode is the ratio of the amount of light being sent to the cathode and how many electrons are emitted as a result. With higher QE less light power, i.e. photons, are required to achieve a certain amount electrons within the bunch. This lowers the amount of damage caused by material ablation and heating from driving the cathode with a laser.

- **spectral response** : this metric is used to determine how well a given wavelength of light is able to generate electrons. This is on the one hand linked to the strength of absorption and secondly linked to the workfunction. For example in semiconductors light is only strongly absorbed above the band gap energy E_g. With lower band gaps it is much easier to create light of the necessary energy to excite electrons through light absorption. Secondly the workfunction generally limits the emission energy of electrons. In metals the absorption is not limited by a gap, but with a high work-function it also limits the useful wavelengths of light. The higher the absorption limit and WF are, the shorter the required wavelength of light has to be to effectively extract electrons.

- **emittance** : the emittance is the width of the electrons' momentum distribution and a measure of how tight together the electrons are in the emitted bunch. This is both a function of how tight the laser spot is focussed and the so-called *intrinsic emittance* of the specific photocathode. The LINAC geometry of FELs makes it very difficult to meaningfully improve this, so low emittance emission is necessary to get the required bunch density at the light emission site. It is influenced by material choice, surface quality, and photon energy.

- **response time** : the response time is the time between the first light arriving at the cathode and the first electrons being emitted from it. It needs to be well defined to correctly operate the LINAC and accelerate the electron bunch efficiently.

- **cathode lifetime** : many photocathode materials have proven very sensitive to residual gases and other contaminants present under the UHV conditions and their performance to degrade rather quickly in some circumstances. The longer the cathode can be operated, the better, as there is less downtime for the FEL and the cathode production cost can be spread over a longer time frame.

The intrinsic emittance of a photocathode can be related to one measure that will be a central point within this thesis. The mean transverse energy (MTE) is a measure of the mean transverse momentum of the electrons, and for a set of electrons with their respective momenta $\mathbf{p}_i$ is defined

Material Group	sub-group	Material	QE range
metal	normal-conducting	Cu, Ag, Mg, TiN [15]	10^{-4} to 10^{-1} [15]
metal	super-conducting	Nb, Pb [32]	10^{-5} to 2×10^{-3} [32]
semiconductor	negative electron affinity	GaAs/CsO, GaN/CsO [15]	0.1 to 0.53[15]
semiconductor	positive electron affinity	Cs_3SB [33], CsTe, K_2CsSb, [15] RbTe [34]	up to 0.1 [15]

Table 1.1: Table of data on the different materials used in photocathodes.

by

$$MTE = \frac{1}{N} \sum_i \frac{\mathbf{p}_{i,\perp}^2}{2m_e}, \tag{1.1}$$

where N is the number of electrons, $\mathbf{p}_{i,\perp}$ is the momentum component perpendicular to the direction of interest, and m_e is the electron mass. It is therefore a measure for how tightly packed the electron bunch is after emission. It is calculated using Equation (1.1) within the model developed and used in this work. The MTE and emittance ε are connected by

$$\varepsilon = \sigma_x \cdot \sigma_{int} = \sigma_x \cdot \sqrt{\frac{MTE}{m_e \cdot c^2}}, \tag{1.2}$$

where σ_x is the root mean square (rms) size of the laser, σ_{int} is called the intrinsic emittance and represents the emittance contribution due to the photocathode, m_e is the electron mass and c is the speed of light in vacuum [18].

The general material types used for photocathodes are metals and semiconductors. Metals have been used for longer, as they can be simply machined into the photocathode and are in general less sensitive to contaminants, but with the downside of lower QE. In contrast the large family of semiconductor materials can achieve much higher QE, but at the cost of having to grow them on a substrate. This is, unless they are commercially available in high purity and crystallinity, like GaN or GaAs [15]. They show much higher QE, but in some cases are very sensitive to surface contaminants during cathode preparation, characterisation and operation. Some more details are given in Table 1.1.

The low QE values from metal photocathodes and their relatively high work-functions, together with the desire to protect the surface from contaminants, are motivating research work in passivation layers, such as graphene [35–37] or metal chalcogenides [38]. Within this work some approaches for hetero-interfaces formed by protective overlayers will be explored.

When looking at semiconductors specifically, it is important to understand the groups divided distinctly by their electron affinity. The electron affinity is the difference between a semiconductor's conduction band minimum (CBM) and the vacuum level. The vacuum level can be lowered by depositing a thin overlayer of Cs/O onto the surface[15]. This lowers the vacuum level beneath the CBM, making the electron affinity negative and increasing the transfer probability from the cathode to the vacuum greatly. This treatment, however, leaves the surface highly reactive, limiting the cathode's lifetime [10].

A significant challenge is the preparation and subsequent characterisation of photocathodes. All steps need to be performed without breaking the vacuum chain, which creates significant challenges. Some examples are the Photoemission and Bright Beams Lab at Arizona State University, which has both cathode production and analysis facilities integrated in a single vacuum system [39]. These kinds of monolithic facilities are difficult and expensive to set up. On the other hand vacuum suitcases can be used to transport photocathode samples within and between labs [40].

This is one motivator for the modelling efforts of photocathode materials, as this can help save resources and in collaboration help guide the direction of improving photocathodes for the next generation of light sources.
Modelling efforts for photocathodes both include the *ab initio* modelling of photocathode materials to explore their phase stabilities [41–43], their facets and surface energies [44], as well as photoemission models [45–48] or machine learning approaches [49, 50]. These efforts are ongoing and are contributing to the understanding of surface structures and their effect on the photocathode performance.

To conclude, given the current state of photocathodes for their application in FELs a range of challenges are still remaining. Modelling the photoemission process within the photocathodes, as discussed, is one of the ways these challenges are being addressed. This thesis has the aim of calculating the photoemission response of a photocathode surface model using *ab initio* electronic structures calculated using density functional theory (DFT). This allows the modelling of the surface specific electronic structure in great detail and with a photoemission model these can be connected to the experimentally available QE and MTE spectra. While it is possible to use more sophisticated approaches to model the many-body physics of the materials, such as the so called GW approach [51], these would also significantly increase the computational demand for each simulation. DFT has been chosen as the basis for this work as it allows calculating experimentally relevant surface structures, such as reconstructions, defects, or interfaces, with available computational resources.

Using DFT gives accurate enough results to reproduce trends with the possibility of semi-quantitative results and can be run on surface structures with hundreds of atoms on state of the art high-performance computing (HPC) facilities. This combination makes DFT the ideal candidate to use for a general framework to model photoemission for photocathode materials and interpret experimentally relevant PE spectra. This will contribute to the more specific understanding of how growth conditions, material phases, defects, and contaminants affect the overall performance of a photocathode. Furthermore, it provides a tool to explore new avenues to address the long list of remaining challenges in photocathode research.

2 Background and Theory

Within this work a series of well established techniques for *ab initio* modelling are used. It is well beyond the scope of this work to discuss the intricacies for each of them and a long line of literature and books already exist for many of them. Thus, only a high level discussion of the main concept will be done here and for more details the cited sources are available.

2.1 The Energy of Quantum Mechanical Systems

2.1.1 The time-independent Schrödinger Equation

One of the foundations for quantum mechanics and approaches to calculating the energy levels in a system was originally introduced by Erwin Schrödinger [52, 53]. The main equation representing these ideas is now known as the time-independent Schrödinger equation for a non-relativistic wavefunction describing a system of interacting particles [54]. For a given system with n interacting electrons and M interacting nuclei it is the eigenvalue problem given by

$$\hat{H}\Psi(\mathbf{r}_1,\ldots,\mathbf{r}_n,\mathbf{R}_1,\ldots,\mathbf{R}_M) = E\ \Psi(\mathbf{r}_1,\ldots,\mathbf{r}_n,\mathbf{R}_1,\ldots,\mathbf{R}_M), \tag{2.1}$$

where $\mathbf{r}_i$ and $\mathbf{R}_I$ are the coordinates of the electrons and nuclei, respectively, E is the expectation value for the energy, and $\hat{H}$ is the Hamiltonian operator given in atomic units by

$$\begin{aligned}\hat{H} = &-\sum_{i=1}^{n}\frac{1}{2}\nabla^2_{\mathbf{r}_I} - \sum_{I=1}^{M}\frac{1}{2M_I}\nabla^2_{\mathbf{R}_I} - \sum_{i=1}^{n}\sum_{I=1}^{M}\frac{Z_I}{|\mathbf{r}_i-\mathbf{R}_I|}\\ &+\sum_{i=1}^{n}\sum_{j>i}^{n}\frac{1}{|\mathbf{r}_i-\mathbf{r}'_j|} + \sum_{I=1}^{M}\sum_{J>I}^{M}\frac{Z_I Z_J}{|\mathbf{R}_I-\mathbf{R}'_J|},\end{aligned} \tag{2.2}$$

where Z_I and M_I are the I^{th} nucleus' charge and mass, respectively. The first two terms are the electronic and nuclear kinetic energy operators, respectively, while the remaining terms give the electrostatic interactions. These are the attraction between the electrons and nuclei (4^{th}), the repulsion between electrons (5^{th}) and finally the repulsion between the nuclei (6^{th}) [54]. Analytical solutions only exist for a system with two interacting particles, such as the H and He^+ atoms, but anything beyond requires approximations.

One such approximation can be made to the wavefunctions, denoted in the following as $\tilde{\Psi}$ and assumed to be normalised, and the eigenvalue problem is redefined within the variational principle. This states that for a normalised approximate wavefunction $\tilde{\Psi}$ the expectation value E

$$\langle\tilde{\Psi}|\hat{H}|\tilde{\Psi}\rangle = E \geq E_0 \tag{2.3}$$

where E_0 is the expectation value for the exact wavefunction Ψ_0 [54]. Given this principle the search for the ground state energy turns into the numerical search of the approximate wavefunction minimising the energy expectation value calculated by applying the Hamiltonian operator.

2.1.2 The Born-Oppenheimer Approximation

Finding the solutions to the variational problem with the full wavefunction including both electrons and nuclei is much more computationally intensive, than just electrons. This is, however, not necessary in the majority of cases. The motion of electrons and nuclei can be assumed to be decoupled, given that a single proton is more than 1800 times heavier than an electron. This assumption is also known as the Born-Oppenheimer approximation [55] and is widely used today for quantum chemistry and other fields [54]. Within this approximation the electrons are set to move inside the electrostatic potential of a set of fixed nuclei. This has the effect of being able to neglect the 2^{nd} term of the Hamiltonian operator written in Equation (2.2) describing the kinetic energy of the nuclei and making the internuclear interaction term (6^{th}) an additive constant [54].

The decoupling of the two motions leads to the following expression for the electronic Hamiltonian $\hat{H}_{elec}$ with the fixed nuclei as

$$\hat{H}_{elec} = -\sum_{i=1}^{n} \frac{1}{2}\nabla^2_{\mathbf{r}_I} - \sum_{i=1}^{n}\sum_{I=1}^{M} \frac{Z_I}{|\mathbf{r}_i - \mathbf{R}_I|} + \sum_{i=1}^{n}\sum_{j>i}^{n} \frac{1}{|\mathbf{r}_i - \mathbf{r}'_j|} \tag{2.4}$$

and the associated Schrödinger equation becomes:

$$\hat{H}_{elec}\Psi_{elec}\left(\{\mathbf{r}_i\};\{\mathbf{R}_I\}\right) = \epsilon_{elec}\left(\{\mathbf{R}_I\}\right)\Psi_{elec}\left(\{\mathbf{r}_i\};\{\mathbf{R}_I\}\right), \tag{2.5}$$

where the electronic wavefunction Ψ_{elec} depends explicitly on the set of electronic coordinates $\mathbf{r}_i$, but only parametrically on the set of nuclear ones $\mathbf{R}_I$, and the electronic energy ϵ_{elec} also only depends parametrically on $\mathbf{R}_I$ [54]. Reincorporating the nuclear electrostatic interaction gives the total energy calculated as

$$\epsilon_{tot} = \epsilon_{elec} + \sum_{I=1}^{M}\sum_{J>I}^{M} \frac{Z_I Z_J}{|\mathbf{R}_I - \mathbf{R}_J|}. \tag{2.6}$$

The Born-Oppenheimer approximation reduces the complexity of the problem, but does not solve the fundamental issue of finding solutions for many electron systems. This requires further approximations, which will be discussed in the following section.

2.2 Solving Schrödinger's Equation for Many Electron Systems

2.2.1 Hohenberg-Kohn Theorems and Kohn-Sham Approach

The limitations to exactly solving the Schrödinger equation for any system of interest have brought about the use of different kinds of approximation schemes, such as the Hartree-Fock method [56, 57], but the one this work is based on is called density functional theory (DFT). This approach is in principle exact in its formulation, except for the BO approximation. In general it applies to any system of interacting particles present in an external potential $V_{ext}(\mathbf{r})$ [58]. The Hamiltonian operator for this system in atomic units is given by

$$\hat{H} = -\frac{1}{2}\sum_i \nabla_i^2 + \sum_i V_{ext}(\mathbf{r}_i) + \frac{1}{2}\sum_{i\neq j} \frac{1}{|\mathbf{r}_i - \mathbf{r}_j|}. \tag{2.7}$$

The formulation of DFT is based on a set of theorems set out by Hohenberg and Kohn [59], which state [58]:

- For the system of interacting particles in the external potential $V_{ext}(\mathbf{r})$, is defined by the ground state density of particles $n_0(\mathbf{r})$, except for an additive constant.
- The ground state density $n_0(\mathbf{r})$ and the associated ground state energy can be linked by a *universal functional* $E[n]$.

With Theorem 1 the Hamiltonian in Equation 2.7 is fully defined, except for an additive energy constant. This means, that the many particle system's properties are fully determined by solely the density $n_0(\mathbf{r})$. With Theorem 2 and following the variational principle, the minimisation of this functional gives the minimal energy E_0, and thus exact solution, for any potential V_{ext}. So the exact ground state density $n_0(\mathbf{r})$ can be obtained through minimisation of $E[n]$.

Proving these theorems goes beyond this work, but one example of such can be found in the book by Martin [58]. One has to note that the universal functional $E[n]$ is not known and so must be approximated. Using the theorems a way is available to finding the ground state particle density for many electron systems. Having established the *universal functional* $E[n]$ as a solution to finding the ground state density of a multi-electron system, it is still not known and needs to be approximated. A solution to this problem was introduced by Kohn and Sham [60] shortly after the publishing of the Hohenberg-Kohn theorems. The solution to this problem put forward is now

called the *Kohn-Sham approach*. It proposes a system of non-interacting particles in addition to the interacting system and one key assumption about the non-interacting system [58]. There exists an external potential, $V_{ext}(\mathbf{r})$, so that when the non-interacting system has it applied, the resulting ground state density is equal to the ground state density of the interacting system.

This essentially assumes that a set of non-interacting particles can be "coaxed" into assuming the ground state density of an interacting system by finding a suitable external potential. And the total energy of this system can be calculated due to the Hohenberg-Kohn theorems using a density dependent energy functional $E[n]$. The specific functional proposed by Kohn and Sham is given by [58]

$$E_{KS}[n(\mathbf{r})] = T_s[n] + \int V_{ext}(\mathbf{r})n(\mathbf{r})d\mathbf{r} + E_{Hartree}[n] + E_{II} + E_{XC}[n], \tag{2.8}$$

where the kinetic energy for the non-interacting particles $T_s[n(\mathbf{r})]$ is defined as

$$T_s[n(\mathbf{r})] = -\frac{1}{2}\sum_i \int \psi_i^* \nabla^2 \psi_i d\mathbf{r} \tag{2.9}$$

with i as the particle index. The kinetic energy for the non-interacting set of particles is obviously not the same as for a set of interacting ones, but close enough to use. The difference will be made up later. Secondly the Coulomb energy of the density $n(\mathbf{r})$ within the Hartree approximation [56], $E_{Hartree}$, is given by

$$E_{Hartree}[n(\mathbf{r})] = \frac{1}{2}\int\int \frac{n(\mathbf{r})n(\mathbf{r}')}{|\mathbf{r}-\mathbf{r}'|}d\mathbf{r}d\mathbf{r}' \tag{2.10}$$

and V_{ext} in Equation (2.8) is in this instance the potential generated by the nuclei combined with any further applied potential, i.e. external to the electronic system, and E_{II} is the energy due to nuclei interaction. The final term, $E_{XC}[n(\mathbf{r})]$, is called the exchange and correlation energy and combines all the remaining contributions missing due to considering a set of non-interacting particles as

$$E_{XC}[n] = F_{HK}[n] - (T_s[n] + E_{Hartree}[n]), \tag{2.11}$$

where $F_{HK}[n]$ is the exact functional introduced with the Hohenberg-Kohn theorems [58]. This exchange-correlation functional is still not known, but rather than approximating this for the full system, one can rely on the known terms to lessen the influence of the approximations. Rather than using the full Schrödinger equation to get the energies of the wavefunctions, the wavefunctions for each of the non-interacting particles is given by a set of Schrödinger-like single-particle equations, also called the Kohn-Sham equations given by

$$\left[-\frac{1}{2}\nabla^2 + V_{KS}(\mathbf{r})\right]\psi_i(\mathbf{r}) = \epsilon_i\psi_i(\mathbf{r}), \tag{2.12}$$

where the Kohn-Sham potential V_{KS} is given by

$$V_{KS}(\mathbf{r}) = V_{ext}(\mathbf{r}) + V_{Hartree}(\mathbf{r}) + V_{XC}(\mathbf{r}), \tag{2.13}$$

where ψ_i are the single-particle states with the energy ϵ_i [58]. From these wavefunctions the density is constructed by

$$n(\mathbf{r}) = \sum_{i=1}^{N_e}\int |\psi_i(\mathbf{r})|^2 d\mathbf{r}, \tag{2.14}$$

which conceptually completes the necessary elements to calculate the energy, potential and density for the Kohn-Sham approach. But this also includes a circular dependency, highlighted in Figure 2.1. The circular dependence of the Kohn-Sham potential, the set of Kohn-Sham equations and resulting density means that an iterative approach needs to be used to find the density minimising the total energy and the most widely used one is called the self-consistent field (SCF) [58].

$$\begin{array}{ccc} n_0(\mathbf{r}) & \overset{HK_0}{\Rightarrow} & V_{KS}(\mathbf{r}) \\ \Uparrow & & \Downarrow \\ \psi_{i=1,N_e}(\mathbf{r}) & \Leftarrow & \psi_i(\mathbf{r}) \end{array}$$

Figure 2.1: Conceptual representation of the circular dependence of quantities within the Kohn-Sham approach. The Hohenberg-Kohn theorems for a non-interacting system HK_0 allow the calculation of the Kohn-Sham potential V_{KS} from the non-interacting density $n_0(\mathbf{r})$, which acts on each of the single-particle Kohn-Sham equations $\psi_i(\mathbf{r})$, that taken together determine the density of non-interacting particles $n_0(\mathbf{r})$. Adapted from Figure 7.1 in Martin [58].

2.2.2 Exchange-Correlation Functionals

As discussed above the *universal functional* $E[n]$ from the Hohenberg-Kohn theorems is unknown and the exchange-correlation functional is also not fully known. But it can be approximated using a long list of approximations, of which only a small number of general families will be discussed here.

The first widely used and rather simple approach is known as the local density approximation (LDA) [58]. As the name implies, the functional for the exchange-correlation energy only considers the local electronic density and can be written out as

$$E_{XC}^{LDA} = \int n(\mathbf{r}) \epsilon_{xc}^{hom}(n(\mathbf{r}))\, d\mathbf{r}, \tag{2.15}$$

where $\epsilon_{xc}^{hom}(n(\mathbf{r}))$ is the exchange-correlation energy for a homogeneous electron gas of a specific density. This quantity has been calculated with great accuracy [58]. This rather simple approximation has been shown to work well for systems, where the density is slowly varying, such as metals. It does, however, struggle for strongly correlated systems, such as transition metal oxides (TMOs) where it underestimates band gaps and overestimates the cohesive energy [58].

An improvement to the LDA approach, being used with great success, is the so-called *generalized gradient approximation* (GGA). This approach moves from a homogeneous free electron gas to a non-uniform one and considers, as the name implies, the gradient of the density as well [58, 61]. The general functional is defined similarly to the LDA approach as

$$E_{XC}^{GGA} = \int n(\mathbf{r}) \epsilon_{XC}^{GGA}(n(\mathbf{r}); \nabla n(\mathbf{r}))\, d\mathbf{r}. \tag{2.16}$$

In contrast to the LDA functional using only the local density, the exact incorporation of the gradient can vary. With this a plethora of different GGA functionals has been published, that all differ in their exact formulation. One widely used functional of note is the Perdew, Burke, Ernzerhof (PBE) functional [62], which does not include any empirical data in its formulation and has shown good applicability to a wide variety of systems. Within this work a functional called PBEsol [63] is used, which was adapted form PBE for better replication of various quantities in solids and surfaces.

The decision to use PBEsol to calculate the electronic structure for photocathode materials will have an impact on some calculated quantities. The GGA class functionals are known to perform well to calculate the structural properties and formation energies, while underestimating, sometimes severely, the bandgaps for semiconductors [64, 65]. This underestimation will then impact the calculated photoemission response as a lower gap is linked to an excitation of electrons at lower photon energies. One approach to address this issue are the the so called hybrid functionals [66–68], which use a linear combination of DFT energy contributions and Hartree-Fock exchange energy contributions [67, 68]. This functional group, however, requires significantly more computational resources, which can become a limitation for the kind of larger surface slab systems considered within this thesis. Furthermore, using a hybrid functional to calculate a metallic system has been shown to alter the electronic structure and fermi surface of metals [69, 70]. Therefore it cannot

be used without consideration on metallic systems [65]. In this thesis the PBEsol functional is used to calculate all photocathode slabs, as they are either a metal or an interface of metal and a semiconductor and to reduce computational demand allowing for larger surface slab systems to be calculated.

This concludes the high-level discussion of the way that DFT is able to calculate the characteristics and electronic structure for many-electron systems and the approximations it is based on.

2.3 Wavefunctions in Extended Systems : Bloch's Theorem

The modelling within this work is for bulk materials and surfaces. While these structures have finite size from a macroscopic perspective, they can be considered infinite on the atomic scale. This is true in all three Cartesian directions for bulk materials and for surfaces along the surface plane. This would mean an infinite amount of atoms and electrons needs to be modelled, which is of course impossible.

The periodic nature within its given lattice, however, relates all the lattice points to each other [71]. The same periodicity applies to the potential within this lattice. Therefore, the squared wavefunctions present within this lattice must also exhibit the same periodicity [71]. In this case Bloch's Theorem states, that both the wave functions must be equivalent at each lattice point except for a phase factor and that these wave functions can be expressed as a product of a periodic function and a wave like part. Expressed formally this states

$$\psi(\mathbf{r}+\mathbf{t}) = \exp(i\mathbf{k}\cdot\mathbf{t})\psi(\mathbf{r}) \quad \text{and} \tag{2.17}$$

$$\psi_k(\mathbf{r}) = \exp(i\mathbf{k}\cdot\mathbf{r})\varphi(\mathbf{r}), \tag{2.18}$$

where ψ is the wavefunction, $\mathbf{t}$ are the lattice vectors, $\mathbf{k}$ is a vector in reciprocal space, and φ is the periodic part of the wavefunction [71]. This approach can be used to construct infinite or semi-infinite systems, by using Bloch functions to describe the electronic states. With this the calculation of the characteristics at a single lattice point are able to represent a (semi-)infinite solid and (bulk) materials.

2.4 Basis Sets

To actually perform calculations of solids using Bloch's theorem, the wavefunctions need to be calculated. Using a suitable basis can have different advantages, like ease of implementation, efficiency and speed. Like the long list of available DFT functionals, a number of different approaches is implemented in the available DFT codes. So only the applicable ones will be discussed here.

2.4.1 Plane Wave Basis Sets

Starting from Bloch's theorem, the periodic part of the wavefunction is expanded using a set of plane waves (PWs) with the wave vectors $\mathbf{G}$. These must have the same periodicity as the cell being calculated. This means the set of $\mathbf{G}$ vectors is a regular grid spaced out by the reciprocal lattice of the cell [72] and results in constructing a discrete Fourier transform (FT), which is modulated by the Bloch phase $\mathbf{k}$. This way the translational symmetry for the charge density and other observables is enforced. For the wavefunction ψ this gives

$$\psi_{\mathbf{k}}(\mathbf{r}) = \sum_{\mathbf{G}}^{\mathbf{G}_{max}} u_k(\mathbf{G}) \exp(i(\mathbf{k}+\mathbf{G})\cdot\mathbf{r}), \tag{2.19}$$

where $\mathbf{G}_{max}$ is the largest considered $\mathbf{G}$ vector, $u_k(\mathbf{G})$ is the expansion coefficient, and $\mathbf{k}$ is a vector in reciprocal space. It can be also thought of as the result of a truncated, discrete Fourier transform of the real space wavefunction into the Fourier space, which is equivalent to the reciprocal space in this case. This connects to the fact that the maximum gradient the PW basis set is properly able

to describe is intimately linked to the basis set quality. The quality of the basis set is normally set by a parameter called the cut-off energy $E_{cut-off}$. This energy is related to $\mathbf{G}_{max}$ by the general formula for the PWs energy, given by

$$E_{PW}(\mathbf{k}) = \frac{\hbar^2 \mathbf{k}^2}{2 \cdot m_e}, \tag{2.20}$$

$$\mathbf{G}_{max} = \sqrt{\frac{2 \cdot m_e \cdot E_{cut-off}}{\hbar^2}}, \tag{2.21}$$

where $\hbar$ is the reduced Planck's constant and m_e is the electron mass [72]. The Bloch phase's $\mathbf{k}$ vector is in principle a continuous variable, so one would in theory need to calculate the expansion at an infinite set of points. This can be greatly simplified by considering, that the wavefunction only varies relatively slowly across $\mathbf{k}$-space [72]. This means that the infinite set of points can be sampled using a small set of points, that just need to have high enough density to give a proper sample. This idea will be further discussed in Section 2.6.

The plane wave (PW) basis is one of the simplest basis sets to implement and has a number of advantages, which include

- an unbiased treatment of all space, no matter if it is close to an atom or not,
- simple to change the basis set quality,
- complete in the sense that it can represent any form of function equally well [72].

This makes it a good choice for a general purpose DFT code to use, but also comes with a few problems. First, the wavefunctions have to be expanded using a large number of PWs to get a good representation, increasing computational demand [72] and the unbiased treatment of space means a cell with a large portion of vacuum "wastes" resources. Further, the exact treatment of core electrons, as described in the next section, is nearly impossible using PWs. This means pseudopotentials, which are also discussed in the next section, have to be used to represent the atoms. The PW basis is used within the CASTEP [73] code and therefore used throughout this work.

2.5 Atomic Pseudopotentials

As discussed in the previous section, the maximal wave function gradient that can be properly described by the plane wave basis set, is intimately connected to the number of included PWs. This has a direct connection to how atoms and their electrons are represented. When considering the atomic states with both valence and core electrons included this becomes a problem. Any atomic state and thus the associated potential is varying rapidly near the nucleus [72]. This has the effect of the need for a very high number of PWs. Additionally the bonding behaviour is mostly determined by the more loosely bound outer electrons further away from the nucleus. This means, if one can simplify the states near the nucleus and retain the parts that matter for the binding interaction these two problems can be addressed [72].

Firstly, if the wavefunctions are smoothed out, the need for a high PW basis cut-off is lessened. Secondly, if one can further incorporate the tightly bound core electrons into the total atomic potential, the number of electrons per atom can be reduced, too. These atomic potentials are known as pseudopotentials, of which different flavours exist [72]. The first one of note are the so called *norm-conserving* pseudopotentials (NCP). Within this family of pseudopotentials the core potential for the included electrons is altered only so far, as to not alter the result of the charge integration over space compared to an all electron atomic potential [72].

The second flavour, which is used throughout this work, is the so called *ultrasoft* pseudopotentials (USP) originally introduced by Vanderbilt and coworkers [74, 75]. For this type of pseudopotentials the condition that the charge integral across the altered region remains the same is slightly

relaxed. This has the effect that the core potential can be altered so that the wavefunctions are even smoother, requiring fewer PWs in the basis set. This type of pseudopotential also has shown great transferability between different chemical environments [72].

The relaxation of the norm conserving constraint has an effect on the pseudopotential structure and can have an impact on the quantities derived from a DFT calculation using USPs. The comparison of the electronic structure between NCPs and USPs has not been performed within this thesis, as the difference in valence states near E_F are not expected to change meaningfully between the two pseudopotential types. One can expect to not have a meaningful impact on the calculated photoemission response, since these electronic states are the ones contributing most to the calculated emission.

The choice of using USPs, rather than the norm-conserving kind, was made to limit the computational cost of the calculations thanks to the faster convergence with respect to the number of PWs. This choice allows for larger surface slabs to be considered, such as supercells and other surface structures. These include defective surfaces or lattice mismatched interfaces, which are material systems and structures of interest to current photocathode research. When constructing the pseudopotential the choice of which electrons to integrate into the core charge and which to treat explicitly is non-trivial and depends very much on the use case. In this thesis the default definition for USPs in the CASTEP code is used as they have been tested by the authors of the code [73]. The specific USPs used within this work are generated by CASTEP during the calculation, hence their name *on the fly generated* (OTFG) [76].

2.6 Monkhorst-Pack (MP) and other Grids

As discussed in Section 2.4.1, $\mathbf{k}$ is in principle a continuous variable, but due to the slow variation of the wavefunction with respect to $\mathbf{k}$, a sampling of a finite set of points can be sufficient. Next to the density of these $\mathbf{k}$ points the specific choice of the locations can have a large effect on the quality of sampling. For example one could fail to resolve the Dirac cones present in graphene, if the cones' meeting points are not included in the sampled grid. This need for a sampling scheme has brought about many approaches, such as the one proposed by Chadi and Cohen [77] or Gilat [78]. A very popular option, which is also implemented in CASTEP and used throughout this work, is the method proposed by Monkhorst and Pack [79]. The consequently named Monkhorst-Pack (MP) grid with the dimensions $N_1 \times N_2 \times N_3$ is generated by

$$\mathbf{k}_{n_1,n_2,n_3} = \sum_{i=1}^{3} \frac{2n_i - N_i - 1}{2N_i}\mathbf{G}_i \quad \text{with } n_i \in \{1, 2, \ldots, N_i\}, \tag{2.22}$$

where $\mathbf{G}_i$ are the reciprocal lattice vectors. This specific approach was developed for structures with the BCC lattice, and in a later paper Pack and Monkhorst [80] propose a modification for hexagonal systems. In CASTEP the general approach is implemented without regard for the specific system symmetry.

2.7 Densities of States

Starting from the electronic states calculated within DFT a number of the structures' characteristics can be derived. A family of widely used ones is based on the concept of a density of states (DOS) for a specific energy interval. These densities can be based on all states, only the states located within a certain part of the simulation cell, or the combinations of two states. All densities of electronic states within this work were calculated using the OPTADOS code and the discussion follows the discussion in publication(s) by Morris, Nicholls, Pickard and Yates [81–83]. The simplest of the two is the total DOS, which can be defined at a temperature $T = 0\,\mathrm{K}$ as

$$I(E) = \sum_n \int_{BZ} \frac{d\mathbf{k}}{(2\pi)^3} \delta(E_{n,\mathbf{k}} - E), \tag{2.23}$$

where E is the energy of interest, n is the state index, BZ is the 1^{st} Brillouin zone, δ is the Dirac delta function, and $E_{n,\mathbf{k}}$ is the state energy at the $\mathbf{k}$ point [81]. The integral is in practice replaced by the sum over the set of $\mathbf{k}$ points, requiring a scheme to account for the discretisation of the continuous variable $\mathbf{k}$. More on this point in Section 2.8.

When requiring the local contributions to the total DOS, one can use a projection scheme to define the contributions of a set of orbitals located on an atom. The result is called the *projected density of states* (PDOS) and is defined as

$$I_{\mu,n}(E) = \sum_n \int_{BZ} \frac{d\mathbf{k}}{(2\pi)^3} F_{\mu,n}(\mathbf{k}) \delta(E_{n,\mathbf{k}} - E), \tag{2.24}$$

where μ is the atomic index, and $F_{\mu,n}$ is the projection weight for the specific state n and the atom μ. The projection scheme used within this work is the projection scheme implemented within CASTEP based on linear combinations of atomic orbitals (LCAO) [84]. The specific definition for $F_{\mu,n}$ is

$$F_{\mu,n}(\mathbf{k}) = Re\left\{T^{\dagger}_{\mu n}(\mathbf{k}) T_{\nu n}(\mathbf{k}) S^{-1}_{\nu\mu}(\mathbf{k})\right\}, \tag{2.25}$$

$$T_{\mu n}(\mathbf{k}) = \langle \psi_n(\mathbf{k}) | \phi_\mu(\mathbf{k}) \rangle \tag{2.26}$$

$$S_{\mu\nu}(\mathbf{k}) = \langle \phi_\nu(\mathbf{k}) | \phi_\mu(\mathbf{k}) \rangle \tag{2.27}$$

where ψ_n is the electronic state in the PW basis, ϕ_μ is the atomic orbital in the LCAO basis, T is the overlap matrix between LCAO and PW states, and S is the overlap matrix between the LCAO states [81, 84].

When interested in electronic excitations between an occupied valence state into an empty conduction state it is very useful to know how many excitations are possible for a given excitation energy. This quantity is also called the joint density of states (JDOS) and is calculated as

$$I_{n,m}(\hbar\omega) = \sum_n^{occ} \sum_m^{unocc} \int_{BZ} \frac{d\mathbf{k}}{(2\pi)^3} \delta(\hbar\omega - (E_{m\mathbf{k}} - E_{n\mathbf{k}})), \tag{2.28}$$

where $\hbar\omega$ is the excitation energy, and n and m are the initial and final band index, respectively [81]. The concept can be expanded to also include the projection operator to only consider excitations that can happen for a specific atom in the cell. This is not done generally, but is quite useful to calculate the optical properties and individual excitations of one atom to use in photoemission calculations. One could call this the *projected joint density of states* (PJDOS) and define it as

$$I_{\mu nm}(\hbar\omega) = \sum_n^{occ} \sum_m^{unocc} \int_{BZ} \frac{d\mathbf{k}}{(2\pi)^3} F_{\mu n}(\mathbf{k}) \delta(\hbar\omega - (E_{m\mathbf{k}} - E_{n\mathbf{k}})). \tag{2.29}$$

All of these DOS quantities include a Dirac delta function δ, which in practice is evaluated using one of the many possible broadening schemes. These are the subject of the following section.

2.8 Brillouin Zone Sampling Schemes

As discussed previously, the continuous **k** variable has to be sampled by a finite set of **k** points. The set of **k** points divides the Brillouin reciprocal space into a series of subcells around each of them. This creates problems when trying to calculate the DOS and other quantities, as it is not trivial how to generalise from the finite set to the continuous space [81], even if the states and wavefunctions only vary slowly over the space. Within the OptaDOS code suite a number of different schemes are available to address this problem [81]:

- **fixed** : The discrete contributions of each sub-cell are broadened using a Gaussian function of fixed width. This is a simple approximation and requires very little user input, but there is a need to balance resolving sharp features in the DOS and creating oscillations in the DOS due to having only a limited number of **k** points [81]. This gives for the δ function in Equation (2.23)
$$\delta(E_{n,\mathbf{k}} - E) \rightarrow \frac{1}{\sigma\sqrt{2\pi}} \exp\left(-\frac{1}{2}\left(\frac{E_{n\mathbf{k}} - E}{\sigma}\right)^2\right), \tag{2.30}$$
- **linear** : This scheme linearly extrapolates the band out from the **k** point using the bands' gradient vector at that point and calculates a DOS contribution within the reciprocal sub-cell. More details can be found in the Publication by Wilkins and Müller [85] and more explanations in the publication describing the OptaDOS code [81].
- **adaptive** : The simple method of using a fixed width Gaussian function can be extended by varying the width depending on the state's gradient at the **k** point. With a high gradient the width is chosen as larger, than when the gradient is small or even non-existent. This alleviates the tension between resolving sharp features in the DOS and obtaining a discontinuous curve due to the finite sampling of reciprocal space [81].

Each of these schemes can be applied to evaluate the δ functions described in the previous section to obtain any of the mentioned densities of states. Within this work the *adaptive* scheme will be used to calculate the DOS, PDOS, JDOS and excitations for the photoemission response calculations.

2.9 Modelling Surfaces

As discussed in Section 2.3 the applicability of Bloch's theorem relies on the translational invariance for the potential, wavefunctions and electron density. This means, that periodicity has to be enforced in all Cartesian directions, which is also called periodic boundary conditions (PBCs). These are by default enforced in all three Cartesian directions in the CASTEP code [73]. These 3-dimensional PBCs are well suited to represent a bulk material using a cell of the appropriate shape and size. These PBCs do, however, require the cell to be modified to allow the modelling of a surface geometry.

A surface has material below it extending laterally infinite, which is here assumed to be the x, y-plane and either a gas, liquid or vacuum above it. This geometry can only be achieved by creating a cell with two distinct volumes in it, the material and the gas/liquid/vacuum, when 3d PBCs are applied. A visualisation of such a cell is shown in Figure 2.2. The 3d PBCs then extend the cell in all directions creating what can be thought of as stacks of semi-infinite material slabs with two surfaces each and some amount of vacuum in between.

To define the structure of the surface slab, the Miller indices h, k, and l are used [86]. These indices define the surface structure for the surface slab and are widely used to classify a specific surface termination. This approach of using a surface slab is also used to define a surface with adsorbates or even defects. For these more complicated surface structures the surface slab has to be constructed in a way, that the periodicity is maintained.

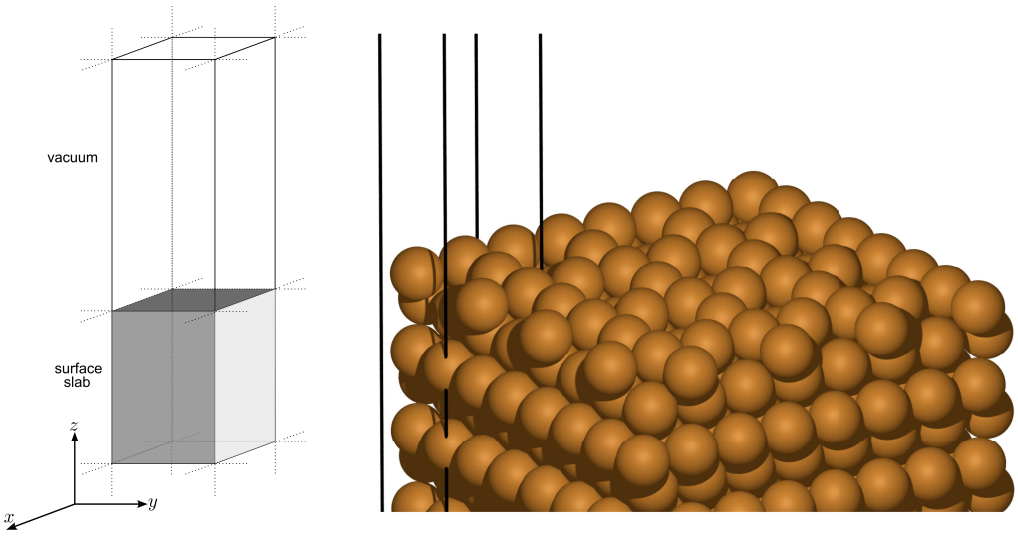


Figure 2.2: left: visualisation of a surface cell with 3-dimensional PBCs applied. The repeated images are indicated by the dotted lines at each corner of the cell. right: Render of a possible SC geometry with one of the surface atoms removed to represent a defective surface.

This means a cell repeating the primitive unit of the surface slab, also called a supercell, is necessary. This supercell is able to for example include a defect of a missing atom in a surface by having a 2×2 supercell and remove one of the four atoms in the surface layer. A visualisation of this for a Cu(100) surface slab is shown in Figure 2.2. For the primitive unit, removing the single atom in the surface layer just removes the layer, due to the enforced periodicity.

3 Theoretical Models for Photoemission

Ever since the first experimental observation of photoemission a long list of approaches has been used to model the process of photoemission and understand the rules and influences of this complex phenomenon. With Einstein's work [87], the very successful and influential works by Berglund and Spicer [88, 89], Damascelli [90], and Dowell and Schmerge [91, 92], over 100 years of research has gone into developing models to predict the PE response of photocathode materials. In the following a subset of these models will be discussed to give context how this work fits into the larger research landscape.

3.1 3-Step Model

In the highly influential formulation of a 3-step model for photoemission by Berglund and Spicer [88, 89] the process is broken into, as the name suggests, three steps. These are excitation, propagation and finally emission of the photoelectron. This approach allows one to treat each phase separately, greatly reducing the complexity of the overall model.

The formulation of the model is based on a photocathode material with a surface termination located at the height $z = 0$ and a normal vector of that surface. The emission angles, i.e. the polar angle θ w.r.t. the surface normal and the azimuthal angle ϕ w.r.t. an axis in the surface plane, and surface coordinate are visualised in Figure 3.1. The azimuthal angle ϕ is not explicitly included in the emission equations, since the entire range from 1° to 360° is assumed to contribute to the emission.

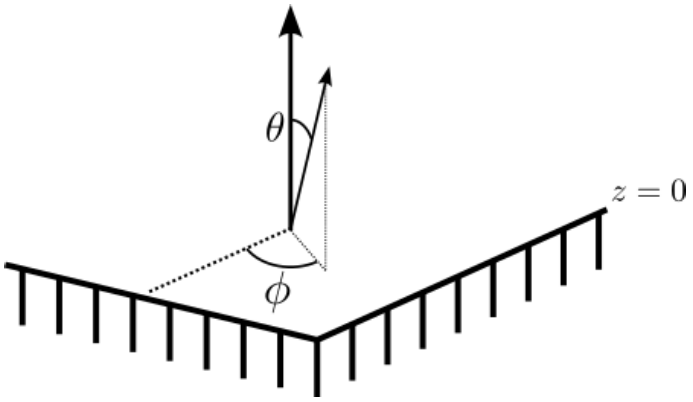


Figure 3.1: Visualisation of the emission angles as they are assumed in the Berglund and Spicer 3-step model. θ is the polar emission angle w.r.t. the surface normal and the emission angle ϕ is the azimuthal angle.

For the last step of the model the transmission probability is assumed to equal unity if the total momentum p is above or equal to a "critical value" p_c, where the normal component $p_\perp > 0$. Below this value the emission probability is simply assumed to be 0 [88]. To calculate the emission probability a scattering model based on a free path length is employed. When an electron located at a given depth z is excited to an energy E it can propagate to the surface and has an associated probability to propagate all the way to the surface. The overall emission probability for the electron at energy E is given by

$$p_{esc}(E, z) = \frac{1}{2} \int_{p_c/p}^{1} \exp\left(\frac{-z}{l \cos\theta}\right) \, d\cos\theta \quad \text{if} \quad p \geq p_c, \tag{3.1}$$

where z is the depth of the electron, l is the free path length, and θ is the polar propagation angle [88]. To derive the excitation rate and connected probability the authors start at the photon

absorption rate for a slice of the material and exciting electrons from energy E to $E + dE$, which gives

$$G(E, z)\ dE\ dz = G_0(E)\ dE\ \exp(-\alpha z)\ dz, \tag{3.2}$$

where dz is the slice thickness, z is again the depth, G_0 is a measure of how photons of a specific wavelength are contributing to the overall excitation rate, and α is the absorption coefficient [88]. Combining these two equations to get the rate of emitted electrons in the energy range E to $E+dE$ gives

$$R'(E)dE = \int_{-\infty}^{0} p_{esc}(E, z)G(E, z)\ dE\ dz, \tag{3.3}$$

$$R'(E)dE = G_0(E)\ dE \int_{-\infty}^{0} p_{esc}(E, z)\exp(-\alpha z)\ dz. \tag{3.4}$$

The lower bound of $-\infty$ for the integration of dz is representative of the semi-infinite nature of the material surface. Performing the integration w.r.t. z and w.r.t. $\cos\theta$ for the escape probability gives

$$R'(E)\ dE = \frac{G_0(E)\ dE}{2\alpha}\left\{1 - \frac{p_c}{p} - \frac{1}{\alpha l} \times \ln\left[\frac{1 + \alpha l}{1 + (p_c/p)\alpha l}\right]\right\} \quad \text{if } p \geq p_c, \tag{3.5}$$

which is not a very insightful form of the equation [88]. To change this the authors expand the logarithm in the last term in an infinite series and the value of this series is represented by a factor K. Furthermore, the authors define a threshold function $C(E)$ given by

$$C(E) = \begin{cases} \frac{1}{2}[1 - \frac{p_c}{p}] & p \geq p_c, \\ 0 & p < p_c, \end{cases} \tag{3.6}$$

which means that the value of $C(E)$ is within the range of $[0, 1/2]$. Substituting K and $C(E)$ into Equation (3.5) gives

$$R'(E)\ dE = \frac{KC(E)G_0(E)\ dE}{\alpha + (1/l)}. \tag{3.7}$$

This still is a complicated function but in a less clunky form. To finally express the number of emitted electrons as a function of energy the absorption rate for a given photon frequency ν is defined as

$$\alpha(\nu) = \int_0^{\infty} \alpha'_\nu(E)\ dE, \tag{3.8}$$

where $\alpha'_\nu(E)\ dE$ is the part of the total absorption that corresponds to the excitation going from E to $E + dE$ [88]. This allows the consideration of two subsets of excitations with $E \to E + dE$ so that they lead to emission, as well as the all possible electronic of excitations. The authors state, that these excitations can be calculated for a specific volume of material using "first and/or second-order time-dependent perturbation theory if the wavefunctions in the solid are known" [88]. This approach is used for the model within this work, see Section 4.3.1 for a more in depth discussion.

Assuming this specific excitation probability from the energy $E_0 \to E$ to be represented by $N_T(E, E_0, \nu)$ the value for $\alpha'_\nu(E)$ can be calculated by

$$\alpha'_\nu(E) = \frac{2h\nu}{n(\nu)c\epsilon_0\varepsilon^2} N_T(E, E_0, \nu), \tag{3.9}$$

where h is Planck's constant, ν is the photon's frequency, $n(\nu)$ is the number of photons for a given frequency, c is the speed of light in vacuum, ϵ_0 is the vacuum permittivity, and ε is the amplitude of the light's electric field vector. To finalise this high-level discussion of the modelling approach by Berglund and Spicer the number of electrons emitted, rather than a rate of emission, can be determined for a given energy range from $E \to E+dE$ for a material, while only considering inelastic scattering events. When the absorption rate is much higher than the scattering rate, i.e. $\alpha \gg 1/l$,

the excited electrons only have a negligible probability of scattering during propagation. This results in the number of emitted electrons $N(E)dE$ given by

$$N(E)\ dE = \frac{R(E)\ dE}{n_p} = \frac{KC(E)\alpha'_\nu(E)\ dE}{\alpha(\nu)} \quad \text{with } \alpha \gg 1/l \tag{3.10}$$

$$= \frac{C(E)N_T(E, E_0, \nu)\ dE}{\int_0^\infty N_T(E, E_0, \nu)\ dE}. \tag{3.11}$$

The discussed cases with only considering a negligible probability of inelastic scattering are elaborated in much more detail within the publication by Berglund and Spicer [88]. The authors further develop expressions to also include elastic scattering into the emission probability. In this paper the authors also apply the emission model to the electronic structure calculated for bulk Cu. Furthermore a discussion of the nature of transitions during the excitation is included by the authors. These transitions can be classified as direct or non-direct. For the direct case, the electron's transverse momentum is conserved during the excitation, whereas the non-direct transition includes a change in the electron's transverse momentum. This change requires momentum transfer from phonons or other sources of momentum. For a material where the majority of transitions is non-direct, the density of states is the material's most important characteristic determining the photoemission response. The authors discuss how the DOS can be determined from photoemission data. All in all, this approach represents the foundation for many subsequent work to build on this concept, especially using the approach to break down the total process into sub-steps.

3.2 Dowell-Schmerge Model

Another series of works expanding the range of emission models for photoemission processes is the series of papers by Dowell, Schmerge and co-workers [91–93]. Their model uses a three step approach of excitation, propagation and emission, just like the foundational work by Berglund and Spicer. In their discussions they start with a rather long and complicated equation incorporating all contributions and use a series of assumptions to simplify the problem. The initial equation for the QE, slightly modified for clarity, assuming $\hbar\omega \leq E_F$, is given by

$$QE(\omega) = [1 - R(\omega)] \frac{\int_{E_F+\phi_{eff}-\hbar\omega}^{\infty} dE P_{excite}(E, \hbar\omega) \int_{\cos\theta_{max}}^{1} d(\cos\theta) F_{e-e}(E, \omega, \theta) \int_0^{2\pi} d\Phi}{\int_{E_F-\hbar\omega}^{\infty} dE P_{excite}(E, \hbar\omega) \int_{-1}^{1} d(\cos\theta) \int_0^{2\pi} d\Phi}, \tag{3.12}$$

$$P_{excite}(E, \hbar\omega) = N(E + \hbar\omega)[1 - f_{FD}(E + \hbar\omega)]N(E)f_{FD}(E), \tag{3.13}$$

$$\cos\theta_{max} = \sqrt{\frac{E_F + \phi_{eff}}{E + \hbar\omega}}, \tag{3.14}$$

where ω is the photon's angular frequency, $R(\omega)$ is the energy dependent reflectance, E_F is the Fermi energy, ϕ_{eff} is the workfunction after lowering due to the electrical field, θ is the polar angle, F_{e-e} is the probability of propagation considering only electron-electron scattering processes, Φ is the azimuthal propagation angle, $N(E)$ is the density of states at energy E, and $f_{FD}(E)$ is the Fermi-Dirac distribution based occupation at E [91, 92]. Essentially the QE is the number of electrons excited to an energy above the effective workfunction $(E_F + \phi_{eff} + \hbar\omega)$ and propagating to the surface without scattering and a propagation angle $\leq \theta_{max}$, is divided by the number of electrons originating close enough to the Fermi energy $(E_F - \hbar\omega)$, that they can be excited into empty states regardless of their propagation direction.

The authors assume that the DOS is constant over the energy range of interest, so $N(E) = N(E + \hbar\omega)$. This assumption is applicable for metals considering only a small range of photon energies just above the effective work function. With this any emitted electrons propagate almost parallel to the surface normal and scattering probability is assumed to be constant w.r.t. θ. Further the scattering rate can be assumed to be constant w.r.t. E for the small energy range of consideration [92]. This gives

$$QE(\omega) = [1 - R(\omega)]F_{e-e}(\omega) \frac{\int_{E_F+\phi_{eff}-\hbar\omega}^{\infty} dE(1 - f_{FD}(E + \hbar\omega))f_{FD}(E) \int_{\cos\theta_{max}}^{1} d(\cos\theta)}{\int_{E_F-\hbar\omega}^{\infty} dE(1 - f_{FD}(E + \hbar\omega))f_{FD}(E) \int_{-1}^{1} d(\cos\theta) \int_0^{2\pi} d\Phi}. \tag{3.15}$$

Further assumptions are made by the authors, that the temperature of the material is sufficiently low, so that the Fermi-Dirac distribution can be replaced by a Heaviside step function [92]. This changes the upper excitation integral boundary to E_F, as there are no electrons available to excite above E_F, and removes the occupation numbers from the integral all together.
This gives

$$QE(\omega) = [1 - R(\omega)]F_{e-e}(\omega)\frac{\int_{E_F+\phi_{eff}-\hbar\omega}^{E_F} dE \int_{\cos\theta_{max}}^{1} d(\cos\theta)}{\int_{E_F-\hbar\omega}^{E_F} dE \int_{-1}^{1} d(\cos\theta) \int_{0}^{2\pi} d\Phi}. \tag{3.16}$$

Finally the scattering probability can be substituted in for an expression derived by the authors, the expression for $\cos\theta_{max}$ from Equation (3.14) substituted in, and the integrations performed for all the integrals. This gives

$$QE(\omega) = \frac{1 - R(\omega)}{1 + \frac{\lambda_{opt}(\omega)}{\lambda_{e-e}(\omega)}} \frac{(E_F + \hbar\omega)}{2\hbar\omega} \left[1 - \sqrt{\frac{E_F + \phi_{eff}}{E_F + \hbar\omega}}\right]^2, \tag{3.17}$$

where $\lambda_{opt}(\omega)$ is the depth where all photons are absorbed and λ_{e-e} is the mean free path for the electron-electron scattering process [92]. An earlier work by Fowler [94] found a quadratic dependence of the QE near threshold and the authors show that when expanding the result in Equation (3.17) with a Taylor series around the emission threshold energy, so $\hbar\omega = \phi_{eff}$, one gets also a quadratic dependence for the excess energy $(\hbar\omega - \phi_{eff})$ [92]. The transverse momentum variance $\sigma^2_{p_\parallel}$, which is related to the MTE, is calculated very similarly to the QE. Here the transverse momentum variance is calculated by ${}^{QE \cdot p_\parallel}/_{(mc)^2 \cdot QE}$, so the initial equation is given by

$$\sigma^2_{p_\parallel} = \frac{\int_{E_F+\phi_{eff}-\hbar\omega}^{\infty} dE P_{excite}(E, \hbar\omega) \int_{\cos\theta_{max}}^{1} d(\cos\theta) \int_{0}^{2\pi} d\Phi p_\parallel^2 \int_{0}^{\infty} ds f(s, E, \theta, \omega)}{(m_e c)^2 \int_{E_F+\phi_{eff}-\hbar\omega}^{\infty} dE P_{excite}(E, \hbar\omega) \int_{\cos\theta_{max}}^{1} d(\cos\theta) \int_{0}^{2\pi} d\Phi \int_{0}^{\infty} ds f(s, E, \theta, \omega)}, \tag{3.18}$$

$$\tag{3.19}$$

where $p_\parallel$ is the emitted electron's transverse momentum, m_e is the electron mass, c is the speed of light in vacuum and $f(s, E, \theta, \omega)$ is the depth s dependent fraction of electrons not scattered before emitting, so a quantity related to F_{e-e} [92]. The authors apply again several assumptions. These are in no particular order, the assumption of a constant DOS, the assumption of constant F_{e-e} w.r.t. E and θ, and $T = 0\,\mathrm{K}$ so the use of a Heaviside step function instead of Fermi-Dirac occupations. This gives for $\sigma^2_{p_\parallel}$ [92]

$$\sigma^2_{p_\parallel} = \frac{\int_{E_F+\phi_{eff}-\hbar\omega}^{E_F} dE \int_{\cos\theta_{max}}^{1} d(\cos\theta) \int_{0}^{2\pi} d\Phi p_\parallel^2}{(m_e c)^2 \int_{E_F+\phi_{eff}-\hbar\omega}^{E_F} dE \int_{\cos\theta_{max}}^{1} d(\cos\theta) \int_{0}^{2\pi} d\Phi}, \tag{3.20}$$

$$p_\parallel = \sqrt{2m_e(E + \hbar\omega)} \sin\theta \cos\Phi. \tag{3.21}$$

The authors perform the integrations, which can be done analytically and get the following for the transverse emittance $\sigma_{p_\parallel}$

$$\sigma_{p_\parallel} = \sqrt{\frac{\hbar\omega - \phi_{eff}}{3m_e c^2}}, \tag{3.22}$$

which is a surprisingly simple relation having started from Equation (3.18).

Given all the assumptions made during the derivation, this model can only be applied for very specific experimental conditions. The prediction of the emittance reaching 0 at threshold is also not corroborated by the experimental results reaching a thermal floor (see experimental data in Section 5), but does make sense under the used assumption of $T = 0\,\mathrm{K}$. In the following sections a number of extensions to this Dowell-Schmerge (D-S) model are discussed.

3.2.1 Extension of D-S like model to $T > 0\,\mathrm{K}$

Given the series of assumptions made in the derivation of the final equations in the D-S model, especially of $T = 0\,\mathrm{K}$, a generally more applicable version of this model was derived by Vecchione

et al. [95], which in the literature is commonly referred to as the *extended Dowell-Schmerge model*. The model is based on the Sommerfeld model for the electronic states of a metal [95]. The authors still assume a constant DOS for the initial and final energies, but explicitly consider the Fermi-Dirac statistics at $T > 0\,\mathrm{K}$. The discussion of the derivation is much shorter, as the only obtainable source is a conference proceeding [95]. The model is based on the three step model by Berglund and Spicer discussed above. For the QE an equation is given as

$$QE(\omega) = S_{12}\left(\frac{\mathrm{Li}_2\left[-\exp\left[\frac{e}{kT}(\hbar\omega-\phi)\right]\right]}{\mathrm{Li}_2\left[-\exp\left[\frac{e}{kT}\mu\right]\right]}\right), \tag{3.23}$$

where S_{12} is a not further defined constant of $0 \leq S_{12} \leq 1$ to represent the first and second step in the three step model, e is the charge of an electron, k is the Boltzmann constant, T is the assumed temperature, $\hbar\omega$ is the photon energy, ϕ is the workfunction, and μ is the electronic chemical potential [95]. The quantity μ can be assumed to be equal to E_F for low enough temperatures [92]. Finally the function Li is the so called polylogarithm function and given by

$$Li_n[z] = \frac{(-1)^{n-1}}{(n-2)!}\int_0^1 \frac{1}{t} Log[t]^{n-2} Log[1-zt]dt, \tag{3.24}$$

which is also used to calculate the transverse emittance ε_x [95]. This quantity, which is related to MTE as discussed in Section 1.2, is calculated as

$$\varepsilon_x = 1000\sqrt{\frac{kT}{m_e c^2}}\sqrt{\frac{\mathrm{Li}_3\left[-\exp\left[\frac{e}{kT}(\hbar\omega-\phi)\right]\right]}{\mathrm{Li}_2\left[-\exp\left[\frac{e}{kT}(\hbar\omega-\phi)\right]\right]}}, \tag{3.25}$$

$$\varepsilon_x = \sqrt{\frac{MTE}{m_e c^2}}, \tag{3.26}$$

$$MTE = kT\sqrt{\frac{\mathrm{Li}_3\left[-\exp\left[\frac{e}{kT}(\hbar\omega-\phi)\right]\right]}{\mathrm{Li}_2\left[-\exp\left[\frac{e}{kT}(\hbar\omega-\phi)\right]\right]}}, \tag{3.27}$$

where m_e is the electron mass, k is the Boltzmann constant, and T is the temperature [95]. When calculating the transverse emittance with this equation the value does not reach 0, but only a thermal floor of kT [95] and so is more useful when comparing with experimental data.

3.2.2 DOS dependent 3-Step Model for Disordered Surfaces

Building on the two previously discussed models the work by Saha et al. [45] focusses specifically on photocathodes with disordered surfaces. This model also breaks the emission process into the three distinct steps of the previously discussed 3-step model. Given the disordered nature of the cathode material, the band structure is considered to be not well defined. Instead the DOS and their occupations are used to give the excitation probability $P_{excitation}$ as

$$P_{excitation}(E) \propto D(E)f(e)D(E+\hbar\omega)[1-f(E+\hbar\omega)], \tag{3.28}$$

where E is the initial energy of the electron, $\hbar\omega$ is the photon energy, $D(E)$ is the DOS and $f(E)$ is the Fermi-Dirac distribution based occupation at the given energies. For the propagation step it is assumed that the photocathode's thickness is small enough, that the scattering of electrons occurs infrequent enough to approximate the propagation probability by a single constant as

$$P_{transport}(E) = C_t. \tag{3.29}$$

Finally during the emission the disordered nature of the photocathode is relevant again. When the electron approaches the surface, it is assumed to scatter into all available free electron states with their associated transverse momentum $k_{\|}$. This is a function of the electron energy and given as

$$P_{emission}(E) \propto C_e \cdot (E + \hbar\omega - E_{vacuum}) = C_e \cdot E_{kinetic}, \tag{3.30}$$

where C_e is a constant representing the 2D DOS in the transverse direction, which is not further discussed in the publication, E is the electron's initial energy, and E_{vacuum} is the vacuum level as calculated by $E_F+\phi$ using the Fermi energy and the workfunction. Similar to the Dowell-Schmerge approach the QE is calculated as the ratio of the emitted electrons and excited electrons and a term relating to the absorption of the cathode. In the Dowell-Schmerge case it was the leftover light after the reflection, i.e. $[1-R]$, while here a simple value α is used. The equation for the QE is stated as

$$QE(\hbar\omega) = \alpha C_t C_e \frac{\int_{-\infty}^{\infty} D(E)f(E)D(E+\hbar\omega)[1-f(E+\hbar\omega)]E_{kinetic}\ dE}{\int_{-\infty}^{\infty} D(E)f(E)D(E+\hbar\omega)[1-f(E+\hbar\omega)]\ dE} \tag{3.31}$$

and for the MTE the full equation is stated as

$$MTE(\hbar\omega) = \frac{\hbar^2}{2m_e} \frac{\int_{-\infty}^{\infty} D(E)f(E)D(E+\hbar\omega)[1-f(E+\hbar\omega)]dE \int_0^{k_{\perp max}} 2\pi k_\perp k_\perp^2\, dk_\perp}{\int_{-\infty}^{\infty} D(E)f(E)D(E+\hbar\omega)[1-f(E+\hbar\omega)]dE \int_0^{k_{\perp max}} 2\pi k_\perp dk_\perp} \tag{3.32}$$

where $k_\perp$ is the transverse momentum of the emitted electron and the maximum transverse momentum $k_{\perp_{max}}$ for a given photon energy is given as

$$k_{\perp_{max}} = \sqrt{\frac{2m_e E_{kinetic}}{\hbar^2}}. \tag{3.33}$$

Inserting this expression into Equation (3.32) and calculating the $dk_\perp$ integrals gives

$$MTE(\hbar\omega) = \frac{1}{2} \frac{\int_{-\infty}^{\infty} D(E)f(E)D(E+\hbar\omega)[1-f(E+\hbar\omega)]E_{kinetic}^2\ dE}{\int_{-\infty}^{\infty} D(E)f(E)D(E+\hbar\omega)[1-f(E+\hbar\omega)]E_{kinetic}\ dE}. \tag{3.34}$$

The authors confirm that when assuming both a constant DOS and $T = 0\,\mathrm{K}$, so replacing the Fermi-Dirac occupations with a Heaviside step function, the QE equation simplifies to $QE \propto E_{excess}^2$ and the MTE equation simplifies to $MTE(\hbar\omega) = \frac{E_{excess}}{3}$. These two relations are the same as the Dowell-Schmerge and extended D-S models discussed above for the given assumptions.

The MTE results from these three models are compared in Figure 3.2, where the DOS dependent model uses the DOS calculated for the 16 layer Cu(100) slab described in Section 5.3.2. One has to note that the integral limits have to be modified to get a sensible result comparable to the graphs shown in the publication. The equation used to numerically integrate and calculate the MTE is given by

$$MTE(\hbar\omega) = \frac{1}{2} \frac{\int_{E_F+\phi-\hbar\omega}^{E_{max}} D(E)f(E)D(E+\hbar\omega)[1-f(E+\hbar\omega)]E_{kinetic}^2\ dE}{\int_{E_F+\phi-\hbar\omega}^{E_{max}} D(E)f(E)D(E+\hbar\omega)[1-f(E+\hbar\omega)]E_{kinetic}\ dE}, \tag{3.35}$$

where E_F is the Fermi energy, ϕ is the workfunction, and E_{max} is the maximal energy the DOS is calculated for, which is $E_{max} \gg E_F$. So the lower limit of the integrals represents all electrons with an energy high enough to be emitted over the workfunction, rather than all electrons regardless of energy. Comparing the different models the increase of MTE as $1/3 E_{excess}$ is clear and for both models using the Fermi-Dirac occupations. The thermal floor as the minimum for the extended D-S model is also evident. The DOS dependent model by Saha et al. further shows a clear divergence from the linear increase at an E_{excess} value high enough, so that the high DOS from the d-states is contributing significantly. Later on the MTE curves slope reaches a linear regime of $1/3$ again. This comparative plot shows the differences in the calculated MTE values nicely and how the assumptions in all three models influence the calculated response.

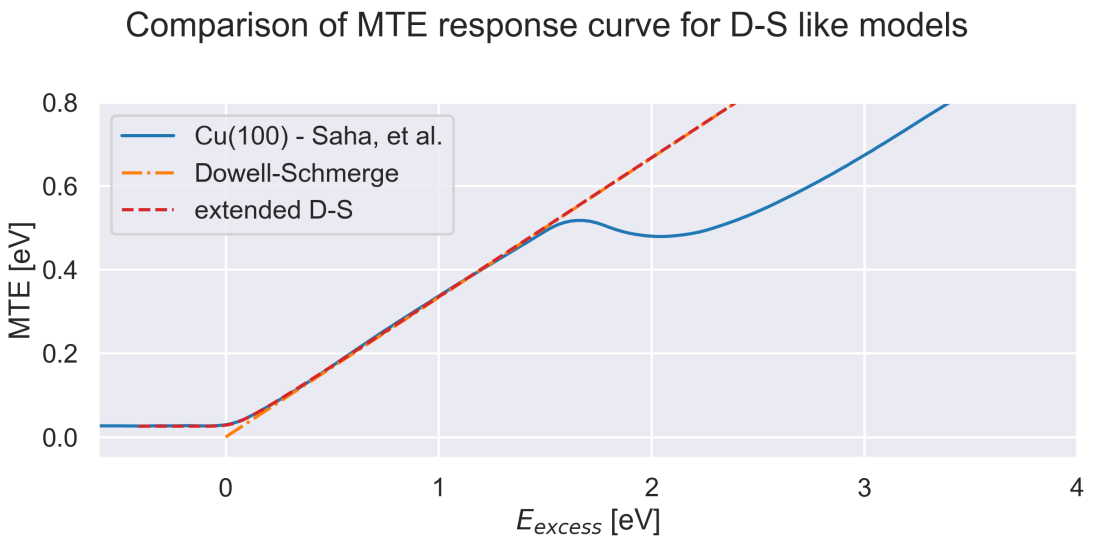


Figure 3.2: A comparison of the MTE curve for three of the discussed emission models. The DOS dependent model was calculated using the DOS from the Cu(100) surface slab model described in Section 5.3.2. Note the discussion on the integral limits for the model by Saha et al. for the DOS dependent model.

3.3 Emittance Model from individual States

Another model building on the foundation of the 3-Step model by Berglund and Spicer, but treating the specifics of each step differently, is discussed in this section. The model published by Antoniuk et al. [46] calculates the contributions from individual states located at $\mathbf{k}$ points, rather than using the DOS across the entire BZ of the materials cell. This is done as a weighted sum across the set of sampled $\mathbf{k}$ points using a weight w_i calculated from the excitation probability, emission probability for a specific excitation from a valence state, and the $\mathbf{k}$ point's transverse momentum $k_{x,i}$ using

$$\varepsilon_{int}(\omega, T) = \frac{\hbar}{m_e c}\sqrt{\sum_i w_i(\mathbf{k}, \omega, T) k_{x,i}^2}\ , \tag{3.36}$$

where ω is the photon's angular frequency, T is the temperature, $\hbar$ is the reduced Planck constant, m_e is the electron mass, and c is the speed of light in vacuum [46]. The normalised weighting factor w_i in turn is calculated using

$$w_i(\mathbf{k}, \omega, T) = \frac{1}{N} w_{i,kpt}(\mathbf{k}) \times w_{i,opt}(\mathbf{k}, \omega, T) \times w_{i,escape}(\mathbf{k}), \tag{3.37}$$

$$N = \sum_i w_{i,kpt} w_{i,opt} w_{i,escape}, \tag{3.38}$$

where $w_{i,kpt}$ is a multiplicity factor for the number of symmetry equivalent $\mathbf{k}$ points, $w_{i,opt}$ is a weight for the excitation probability, and $w_{i,escape}$ is the probability of escape for a given final state and $\mathbf{k}$ point [46].

The multiplicity factor $w_{i,kpt}$ is determined from the full set of MP grid $\mathbf{k}$ points by considering if a number of $\mathbf{k}$ points is both related by symmetry and also has the same squared transverse momentum $\mathbf{k}_x^2$. Only if both conditions are met is the set reduced and the multiplicity value adjusted accordingly. To calculate the excitation probability the matrix element for the transition and occupations are included as

$$w_{i,opt}(\mathbf{k}, \omega, T) = |\langle \psi_{\mathbf{k},c} | \vec{p} | \psi_{\mathbf{k},v} \rangle|^2 \times \delta[E_c(\mathbf{k}) - E_v(\mathbf{k}) - \hbar\omega] \times [f(E_v(\mathbf{k}), T) - f(E_c(\mathbf{k}), T)], \tag{3.39}$$

where $\psi_{\mathbf{k},c}$ and $\psi_{\mathbf{k},v}$ are the conduction and valence state, respectively, $E(\mathbf{k})$ are their respective energies, and $f(E,T)$ is the energy $E(\mathbf{k})$ and temperature T dependent Fermi-Dirac distribution to give the respective occupations of both states [46]. The specific formulation of the model is within the projector-augmented wave (PAW) DFT, so the authors use an approach by Gajdos et al. [96] calculating the imaginary part of the dielectric constant. This can be connected to the photoexcitation probability, as the imaginary dielectric constant is directly related to the absorption. Finally the delta function in Equation (3.39) is evaluated using

$$\delta(x) = \frac{1}{\sigma} \frac{\exp(-x/\sigma)}{(1+\exp(-x/\sigma))^2}, \tag{3.40}$$

where σ is the width. These equations allow the calculation of the electronic excitation probability for a given set of DFT electronic states.

For the second step in the 3-step model, i.e. the propagation, the authors choose to neglect inelastic and elastic scattering processes and their influence. This argument is based on the publication by Dowell and Schmerge [92]. This publication, according to Antoniuk et al. [46], only shows a change of $< 1\,\%$ for the emittance when omitting the scattering processes.

Finally, the emission probability for the electron is calculated using the transmission probability of a plane wave expanded Bloch state into the vacuum. This transmission probability is from the cathode material across the work function into the vacuum, which is modelled as a potential step. By constructing the plane wave expansion for the Bloch state in the material, a free electron state in vacuum, and matching value and gradient of the Bloch state and free electron state at the potential step, the authors obtain an equation to calculate the transmission probability. The PW expansion of the Bloch state includes a series of $\mathbf{G}$ vectors, as discussed in Section 2.4.1 and the authors choose to only consider the $\mathbf{G} = \vec{0}$ contribution to the transmission probability. This approximation is applicable for photon energies low enough, that only the first BZ, where $\mathbf{G} = \vec{0}$, can contribute to emission [46]. With this approximation the escape probability is given by

$$w_{i,escape}(\mathbf{k}) = \frac{4\mathbf{k}_{z,in}\mathbf{k}_{z,out}}{(\mathbf{k}_{z,out}+\mathbf{k}_{z,in})^2} \tag{3.41}$$

$$k_{z,out} = \sqrt{\frac{2m_e}{\hbar^2}(E-\phi) - k_{x,out}^2 - k_{y,out}^2} \tag{3.42}$$

$$k_{x,out} = k_{x,in} + G_x(=0) \quad \text{and} \quad k_{y,out} = k_{y,in} + G_y(=0) \tag{3.43}$$

where $\mathbf{k}_{out}$ is the momentum of the free electron wave, and $\mathbf{k}_{in}$ is the Bloch wave's momentum [46].

The authors discuss, that this scheme is more suited for bulk electronic structures, but in the publication use it with some success for a PbTe(111) surface electronic structure [46]. It could be possible to use this approach for the transmission probability in the photoemission model described within this work. However, in the emission model for the surfaces adopted, see Section 4, the value of $k_{z,in} = 0$ by default, since the direction along the surface normal must not be periodic. Therefore the value of $w_{i,escape}$ would always $= 0$ and no emission could be calculated. It would be possible to take the contributions with $\mathbf{G} \neq \vec{0}$, which would result in a different Equation to (3.41), but the choice for the set of $\mathbf{G}$ vectors to consider is non-trivial. This difficulty led to using the approach described within Section 4.5.2 for the implementation of the photoemission model.

3.4 1-Step Model

The upside of breaking down the complex emission process into three distinct steps for the 3-step model is also a downside. It is not clear that this approximation can be made and thus alongside the 3-step model developments a large body of research has been published with the goal of constructing a model with a single emission step. The main difference to the 3-step model is the change to calculating the excitation into a free electron state. This state is modified within the material and only has finite penetration depth, but is not a Bloch state like in the 3-step model.

While a series of 1-step models has been developed, for example Adawi [97], Mahan [98], Caroli [99], or Liebsch [100], this discussion will be guided by the publication by Pendry [101], who also published a code with coworkers [102] to perform these 1-step calculations. Only a high level discussion can be made here, as the description of the model in the publication is very detailed and would go well beyond this work.

The final state outside the crystal, constructed by Pendry [101] in atomic units, is defined by

$$\langle \mathbf{r}|\mathbf{k}_\parallel, E+\omega\rangle = \frac{1}{\sqrt{L^3}}\exp(i\mathbf{k}^-\cdot\mathbf{r}), \quad z<z_0 \tag{3.44}$$

$$\mathbf{k}^\pm = \left(\mathbf{k}_{\parallel x}, \mathbf{k}_{\parallel y}, \pm\sqrt{2(E+\omega)-|\mathbf{k}_\parallel|^2}\right), \tag{3.45}$$

where $\mathbf{k}_\parallel$ is the transverse momentum vector, E is the initial electron energy, ω is the photon's angular frequency, L is the length of the cubic box confining the material, z_0 is the surface and the z component of $\mathbf{k}$ is negative since the z axis points into the surface within this formulation. To construct the final state as a combination of Bloch states with the energy $E+\omega$ and get the transition probability from the initial states $|j,E\rangle$, the author chooses to use a perturbation theory based approach, which gives

$$\sum_{\mathbf{k}_\parallel} -\frac{iL}{\mathbf{k}_z^+}|\mathbf{k}_\parallel, E+\omega\rangle\langle\mathbf{k}_\parallel, E+\omega|\Delta|j,E\rangle, \tag{3.46}$$

where Δ is the perturbation Hamiltonian [101]. The remaining issue is that all the Bloch states at energy $E+\omega$ would still need to be calculated to get a description of the final state. So a much more efficient approach is one, which only calculates the single state the electron is excited into [101]. The formulation by Pendry relies on starting with the electron after excitation to the energy $E+\omega$ and then calculating how the resulting "wavefield" evolves due to propagating and scattering towards the surface, but including a time reversal of the specific propagation. This propagation can be described by a Green's function, G_2^+, which includes all possible scattering paths during this process [101]. So the Green's function is a way to have the electron start out within the slab and end up outside the surface while traversing any of the possible paths in between. This approach gives a new description for the final state as

$$\sum_{\mathbf{k}_\parallel} -\frac{iL}{\mathbf{k}_z^+}\langle\mathbf{r}|\mathbf{k}_\parallel, E+\omega\rangle\langle\mathbf{k}_\parallel, E+\omega|\Delta|j,E\rangle = \int G_2^+(E+\omega,\mathbf{r},\mathbf{r}')\langle\mathbf{r}'|\Delta|j,E\rangle d^3\mathbf{r}', \tag{3.47}$$

where $\mathbf{r}'$ is the initial position, and $\mathbf{r}$ is the final position. This still requires the calculation of the initial states $|j,E\rangle$. Instead of performing this calculation on a 3-dimensional box, the problem is recast as the calculation of a photocurrent of emitted electrons through a plane of size L^2. This current is given by

$$I(\mathbf{k}_\parallel, E+\omega) = \langle\phi|G_2^+\Delta|j,E\rangle\langle j,E|\Delta^\dagger G_2^-|\phi\rangle \times \mathbf{k}_z^+\rho(E), \tag{3.48}$$

$$\langle r|\phi\rangle = \frac{1}{L}\exp(i\mathbf{k}_\parallel\cdot r_\parallel)\delta(z-Z), \tag{3.49}$$

where ϕ is the final electron state outside the surface, Z is the z coordinate where the plane is located, and $\rho(E)$ is the density of initial states at energy E. This equation can be rewritten, using an identity for the initial states $\langle j,E|$ and their density $\rho(E)$, as

$$I(\mathbf{k}_\parallel, E+\omega) = -\frac{1}{\pi}\mathrm{Im}\langle\phi|G_2^+\Delta G_1^+(E)\Delta^\dagger G_2^-|\phi\rangle, \tag{3.50}$$

where $G_1^+(E)$ essentially describes the scattering behaviour of the free electron state in the material after being de-excited from $E+\hbar\omega$ to E [103]. So the explicit calculation of the initial states is no longer required to calculate the emission characteristics at a given energy and transverse momentum. The material still needs to be represented somehow, to calculate the scattering behaviour

and the resulting electron emission. The chosen approach to represent the atoms within the slab are muffin tin potentials, with a constant potential V_0 outside the radius of the tin potential. The potentials are grouped together into their respective layers to calculate their scattering behaviour for the photoemission state and the surface potential step is assumed to not influence any electrons above its energy [103]. A finite emission depth is considered by modifying the constant potential V_0 to have an energy dependent imaginary component V_{0i}, which can be related to the path length λ

$$\lambda \approx \frac{1}{2}\left|\frac{\sqrt{2(E-V_{0r})}}{V_{0i}}\right|, \tag{3.51}$$

where E is the initial electron energy and V_{0r} and V_{0i} are the real and imaginary parts of the potential V_0, respectively.

The calculation of the emission current density is described as a process progressing in a loop-like fashion. This loop is broken down in into three distinct segments.

- start outside the surface at the final energy $E+\omega$ and the scattering and propagation is calculated for the surface model;
- de-excitation to E occurs and a further scattering and propagation in the model is calculated;
- re-excitation to $E+\omega$ occurs and a final scattering and propagation within the model and back to outside the surface is calculated finalising the loop.

This approach has shown to give good results for metal surfaces in the UPS regime [104]. A direct implementation within the PW-DFT is likely to be difficult, especially when using USPs that have different scattering behaviour to the full electron atom potential.

3.5 Dampened Plane-Wave Model

A quite simple, but nonetheless successful model has been published Puschnig et al. [47, 105] and Lüftner et al. [106] to analyse the PE response of organic molecules adsorbed or bound on substrates. The PE final state is approximated by a simple plane wave and the PE intensity based on a Fermi's Golden Rule type equation gives

$$I(p_x,p_y,\hbar\omega,\mathbf{A}) \propto \sum_{n}^{occ}\sum_{\mathbf{k}}^{BZ} |\mathbf{A}\cdot\mathbf{p}|^2 \left|\langle \exp(i\mathbf{p}\cdot\mathbf{r})|\psi_{n\mathbf{k}}\rangle\right|^2 \times \delta(\varepsilon_{n\mathbf{k}}+\Phi+E_{kin}-\hbar\omega), \tag{3.52}$$

where $\mathbf{p}$ is the electron's final momentum, $\hbar\omega$ and $\mathbf{A}$ are the photon's energy and polarisation vector, respectively, n is the state index going over all occupied states, $\mathbf{k}$ is the originating $\mathbf{k}$ point within the Brillouin zone (BZ), Φ is the workfunction, and E_{kin} is the electron's kinetic energy after emission [106]. The transition matrix element given in the second to last term and the energy conservation in the last term are modulated by a light polarisation and emission angle dependent *geometry factor* [106]. This approach is easily calculated when the initial state is already expanded in a plane wave basis, see Section 2.4.1 for more detail, and the matrix element for the transition between the states is given by

$$\langle\psi_{n\mathbf{k}}|\exp(i\mathbf{p}\cdot\mathbf{r})\rangle = \sum_{\mathbf{G}}^{\mathbf{G}_{max}} c^*_{n\mathbf{k}}(\mathbf{G})\delta_{\mathbf{G},\mathbf{p}-\mathbf{k}}, \tag{3.53}$$

where $\mathbf{G}$ are the set of reciprocal lattice vectors up to $\mathbf{G}_{max}$, $c_{n\mathbf{k}}$ are the PW coefficients, and $\delta_{\mathbf{G},\mathbf{p}-\mathbf{k}}$ is the delta function to filter for the plane waves in $\mathbf{G}$, which are equivalent to the change in momentum going from the Bloch momentum $\mathbf{k}$ to the free electron momentum $\mathbf{p}$ [106]. Finally to account for the dampening of the free electron wave within the material, the final electron state is modified and given by

$$|\psi_f\rangle = \begin{cases} \exp(i\mathbf{p}\cdot\mathbf{r})\exp(\gamma(z-z_0)) & z<z_0 \\ \exp(i\mathbf{p}\cdot\mathbf{r}) & z\geq z_0, \end{cases} \tag{3.54}$$

where z is the depth into the material, z_0 is the surface reference of the substrate, and γ is the inverse of the mean free path in the material [106]. This dampens the amplitude of the final state going into the material and consequently lowers the excitation and emission probability. One can then perform the calculation of qualitative emission maps from DFT calculations and compare them to experimental ARPES data. This approach without the dampening has been used to qualitatively predict the ARPES response of organic molecules on substrates [47, 105] and the method discussed here for the specific interaction of the molecule and the substrate [106]. Rather than using a bulk cell to calculate the electronic structure the substrate surface and adsorbed molecule are calculated explicitly allowing the study of the surface interface and its specific electronic structure.

The implementation of the 1-Step like model matrix element within this work is based on the concept of constructing the final state with a specific momentum and calculating the overlap integral between the initial Bloch state and final free electron state. The dampening of the wave is also performed using a mean free path approach. See Section 4.6 for a more detailed description of the model.

4 The OptaDOS Photoemission Model

The specific implementation of the general approaches to the 3-step and 1-step models, discussed in Section 3, will be discussed below. Compared to a lot of literature calculating the photoemission response of a photocathode material, this model is specifically designed for slab models representing a surface and to break down the overall response into the components coming from different layers or even single atoms or electronic states. Many works use the bulk electronic structure [45, 107–109] to model an inherently surface dependent phenomenon. With this implementation of the model the specific electronic structure of surface slabs is able to be considered. This allows to specifically model the rich surface chemistry of photocathodes and will hopefully contribute to the understanding of photocathode behaviour and the current challenges of lifetime and efficiency.

The PE response of photocathodes has been shown to be intimately linked with the surface structure, where disorder limits the lower bound of emittance and diminishes the QE [33]. Furthermore, the desire to modify the photocathode surface to increase desirable PE characteristics and suppress undesirable ones is evident from many published studies [15, 35–37, 110, 111]. A photoemission model should be able to accurately represent the surface and chemical environment of cathodes to help in guiding and the interpretation of experimental data and studies. This is very difficult with a model using only the electronic structure of a bulk material.

In addition to having an emission model capable of dealing with the specific electronic structure of a surface, the surface model itself must also accurately represent the cathodes properties. This combines the surface and the underlying bulk, so the model must have enough layers to reach bulk like conditions in the middle. The slab's workfunction, surface energy, layer DOS and more are all dependent on the slab size and special attention needs to be put on the convergence of these quantities.

4.1 Defining the Surface Geometry, Layers, and Work Function

The slab model contains two distinct zones, the one with the material and the free space or vacuum. The boundary between these two, i.e. the surface, is not clearly defined. There are many different ways this could be defined, such as taking the z coordinate of the outermost atom and adding the atom's valence radius or taking the z coordinate, where the electrostatic potential has flattened out. Within this work the surface has been defined as the z coordinate, where the normalised DFT electronic density crosses below 0.01 or 1 percent. This threshold is indicated in Figure 4.1 as *top surface density cut-off*. An example of a graph showing the result for a Cu(100) slab is shown in Figure 4.2.

To correctly calculate the optical properties, however, the volume of each layer has to be calculated. Normally OptaDOS uses the entire volume of the cell to define its optical properties, but for a slab this does not work. For further definition of how the optical properties are calculated, see Section 4.2. For the photoemission calculation two approaches to calculate the layer boundaries are available for the user. The first one uses user supplied values for the z coordinate of the top $slab_{max}$ and bottom surface $slab_{min}$ and is visualised as option 1 in Figure 4.1. The steps in the algorithm to define the slab middle z_{ref}, layer height z_{layer} and all the atoms in a layer are

1. Define the initial slab middle z_{init} as

$$z_{init} = \frac{slab_{max} - slab_{min}}{2}. \tag{4.1}$$

2. Check if an atom is within ± 0.1 Å to this slab middle, i.e. the slab has an odd number of layers. If so, take note of this atom and its neighbour in the layer below and their z coordinates z_{atom1} and z_{atom2}.
   If there is an even number of layers, find the two atoms closest to the initial slab middle above and below. Take note of their z coordinate as z_{atom1} and z_{atom2}.

3. If there are more atoms within $z_{atom} \pm 0.5$ Å of $atom1$ or $atom2$, take the mean of their z coordinates to define z_{atom1} and z_{atom2}. This would be the case for a material with multiple atoms per layer or supercell structures. The average z-coordinate is a better measure of the layer middle than the z-coordinate of a random atom in the layer.

4. Redefine the slab middle z_{ref} as

$$z_{ref} = \frac{z_{atom1} - z_{atom2}}{2}. \tag{4.2}$$

5. Define the interlayer distance z_{layer} as

$$z_{layer} = z_{atom1} - z_{atom2} \tag{4.3}$$

and calculate the layer volume V_{layer} as

$$V_{layer} = A_{cell} \cdot (z_{atom1} - z_{atom2}). \tag{4.4}$$

6. Starting from z_{ref} add a layer of height z_{layer} going upwards until the top z coordinate of that layer is above $slab_{max}$ to define the boundaries for all layers above z_{ref}.

7. Sort all atoms above z_{ref} into their respective layers by checking if

$$z_{layer}(bottom) \leq z_{atom} \leq z_{layer}(top). \tag{4.5}$$

As evident in Figure 4.1 the layers align well for the homogeneous part of the shown interface, i.e. the Ag part, but for the interface and all extrapolated layers above the atom and layer alignment much less accurate.

For the second option, visualised as *option 2* in Figure 4.1, the user defines the slab middle z coordinate and the top z coordinates for all layers above the slab middle. The slab's top surface is set by the final layer's top boundary. Within this work the *top surface density cut-off* is used to define the top surface, but it is for the user to decide on the exact way to define the surface z coordinates. This way the layer assignment is much more flexible, than the first option, but requires a bit more work by the user. As evident in Figure 4.1 the alignment of all layers is very good, given that the user has supplied proper z coordinates. So overall, the first one requires less data from the user, but it can be more difficult to get proper layer alignment for a given slab model.

After the layer assignment has been performed, the top and bottom z coordinates for all layers and their thicknesses $t(l)$ have been calculated. The atoms n within each layer l can be determined by checking the layers' top and bottom z coordinate against the atoms' z coordinate and sorting them into the corresponding layer, i.e. $z_l(bottom) \leq z_n \leq z_l(top)$.

Finally, a material's workfunction (WF) is generally defined as the minimal amount of energy needed to move an electron from the Fermi energy to the outside of the material. In this work the structures' WF W is calculated as the difference between Fermi energy E_F and the average electrostatic potential in vacuum E_V,

$$W = E_V - E_F. \tag{4.6}$$

For a given slab model the value of E_V is calculated using the average value of the one electron potential at the middle of the vacuum region. With sufficient vacuum in between the slab copies the one electron potential reaches a steady value and the value of E_V is well defined. An alternative to the approach discussed here is given in a publication by Fall, Binggeli and Baldereschi [112]. An example of the WF calculation is given in Figure 4.2. With the WF, the layer volumes and the atoms sorted into their respective layers the optical parameters for each can be calculated.

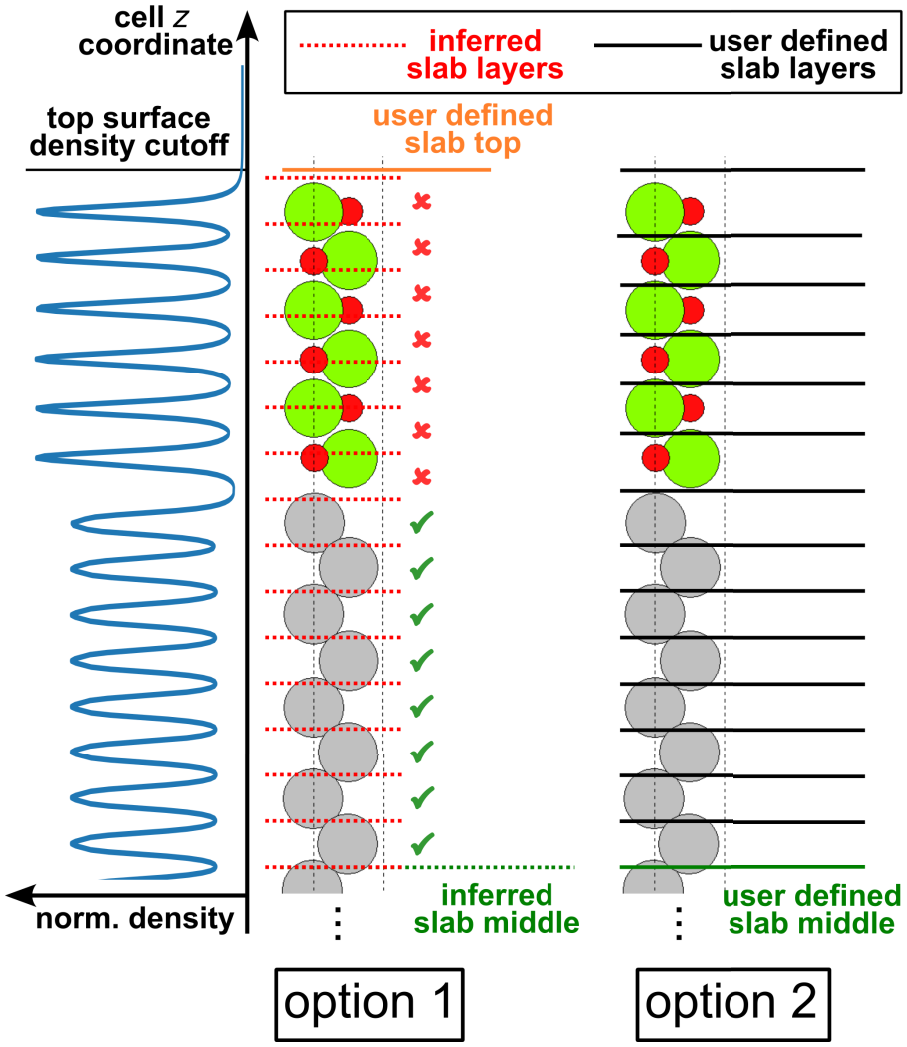


Figure 4.1: Visualisation of the two options for assigning atoms to a set of layers for a MgO on Ag interface slab. The Mg, O, and Ag atoms are coloured light green, red, and grey, respectively. The two implemented approaches are visualised for the slab model and also where they can go wrong. Option 1 takes the *user defined slab top* and *user defined slab bottom* (not shown) as inputs, infers a slab middle and calculates the layer height based on the layer spacing in the middle. This option works well within a homogenous material, as the layers of Ag for option 1 are nicely aligned with atom spacing. At the interface and beyond, however, this spacing does not align any more and the layers of MgO are not well defined by the inferred slab layer height. Option 2 shows the approach of having the user define the boundaries for each of the layers, here the layer height varies slightly, but is able to accommodate both the Ag slab layer height, interface and MgO slab layers.

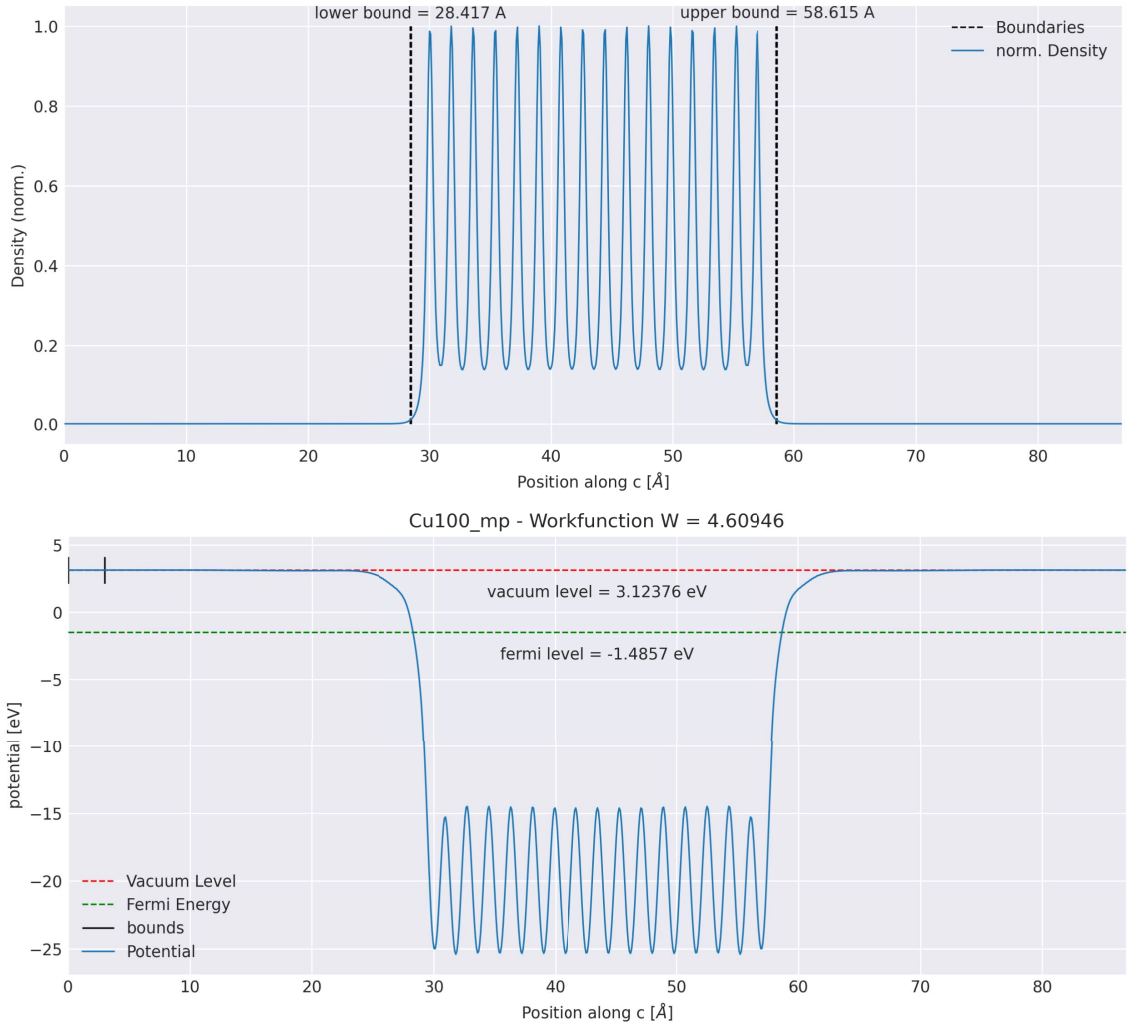


Figure 4.2: Exemplary plots used to determine the boundaries from the electronic density (left) and and WF from the one electron potential and E_F (right) for a Cu(100) surface slab with 16 layers.

4.2 Calculating Optical Properties

When describing the behaviour of light penetrating a material and the associated optical properties, it is important to consider the effect the photon's electric field has on the electrons in the material. The interaction between the electrons within the material and the electric field can lead to the excitation of electrons and absorption of the radiation.

To describe the probability of these excitations w, from the initial bands Ψ_i to the final bands Ψ_f, the so called 'Fermi's Golden Rule' is the chosen description for the perturbation of the initial state by the lights electric field [113, p. 41] and it is given by:

$$w \propto \frac{2\pi}{\hbar} \left|\langle \Psi_f | \Delta | \Psi_i \rangle\right|^2 \delta(E_f - E_i - \hbar\omega), \tag{4.7}$$

where $\hbar$ is the reduced Planck's constant, Δ is the perturbation, δ is a delta function, E_f is the energy of the final state Ψ_f, E_i is the energy of the initial state Ψ_i, and $\hbar\omega$ is the photon energy. The part $\left|\langle \Psi_f | \Delta | \Psi_i \rangle\right|^2$ of the equation is also called the optical matrix element (OME) or matrix element and the operator Δ is given by

$$\Delta = \frac{e}{2m_e c}(\mathbf{A}\cdot\mathbf{p} + \mathbf{p}\cdot\mathbf{A}) - e\phi + \frac{e^2}{2m_e c^2}\mathbf{A}\cdot\mathbf{A}, \tag{4.8}$$

where e and m_e are the electron charge and mass respectively, c is the speed of light in vacuum, $\mathbf{A}$ is the light's vector potential and ϕ is the scalar potential of the light, and $\mathbf{p}$ is the momentum operator given by $\mathbf{p} = i\hbar\nabla$ [113, p. 41]. The commutation of $\mathbf{A}$ and $\mathbf{p}$ in the first part of Equation (4.8) gives

$$\mathbf{A}\cdot\mathbf{p} + \mathbf{p}\cdot\mathbf{A} = 2\mathbf{A}\cdot\mathbf{p} + i\hbar(\nabla\cdot\mathbf{A}). \tag{4.9}$$

This description of the perturbation can be greatly simplified by assuming that two photon processes are not included and thus neglecting $\mathbf{A}\cdot\mathbf{A}$, applying the so called *Coulomb gauge* gives $\phi = 0$ and $\nabla\cdot\mathbf{A} = 0$. Finally considering the photon energies of interest for photoinjectors are usually in the visible to ultraviolet range (i.e. up to $\sim 25\,\mathrm{eV}$) this gives wavelengths of upwards of $\sim 50\,\mathrm{nm}$ and one can further assume the light vector field $\mathbf{A}$ to be constant, i.e. $\mathbf{A} = \mathbf{A}_0$, over the volume of interest, giving

$$\Delta = \frac{e}{m_e c}\mathbf{A_0}\cdot\mathbf{p}. \tag{4.10}$$

With this result for the perturbation, Hüfner [113, p. 41] also writes that for a fully local electron potential there exist a further proportionality $\langle \Psi_f | \mathbf{A}_0\cdot\mathbf{p} | \Psi_i \rangle \propto \langle \Psi_f | \mathbf{A}_0\cdot\mathbf{r} | \Psi_i \rangle$. These two versions of the matrix element can also be called the momentum and length matrix elements, respectively [114–116]. With the change to include non-local parts in the electron potential, this proportionality is no longer true as shown by Starace [114] and a further term results from the interaction between the light's potential and the non-local potential. They further argue that with a non-local potential it is no longer sufficient to use the momentum matrix element and the length matrix elements are the correct approach [114].

While all the calculations within this work are using local DFT functionals, CASTEP uses non-local ultrasoft pseudopotentials (USPs) by default [76] and thus the length matrix elements with non-local contributions have to be calculated. The CASTEP code bases the calculation of matrix elements on the work by Read and Needs [117] and uses a linear response to a very small momentum perturbation $\mathbf{q}$. They give the difference between the two matrix elements based on Starace [114] as

$$R = \mathbf{z}\cdot\langle \Psi_f | \mathbf{r} | \Psi_i \rangle, \tag{4.11}$$

$$P = \frac{-i}{m_e\omega}\mathbf{z}\cdot\langle \Psi_f | \mathbf{p} | \Psi_i \rangle, \tag{4.12}$$

$$R = P + \frac{1}{\hbar\omega}\mathbf{z}\cdot\langle \Psi_f | [U(\mathbf{r}), \mathbf{r}] | \Psi_i \rangle, \tag{4.13}$$

where $\mathbf{z}$ is the light's polarisation unit vector, Ψ_i and Ψ_f are the initial and final state's wavefunctions, m_e is the electron mass, $\mathbf{r}$ and $\mathbf{p}$ are the position and momentum operators, $\hbar\omega$ is the energy difference between Ψ_i and Ψ_f, and $U(r)$ is the non-local part of the pseudopotential. To calculate the commutator $[U(\mathbf{r}), \mathbf{r}]$ they use the result given by Hybertsen and Louie [116] in their Equation (B8) to calculate the dielectric polarisability within the random-phase approximation. It is beyond the scope of this model description to discuss the commutator formula in full detail, but the result relies on calculating the response to the very small momentum perturbation $\mathbf{q}$ in the limit $\mathbf{q} \to 0$ where the initial wavefunctions' momentum $\mathbf{k}_i$ is shifted by $\mathbf{q}$. This gives the matrix elements to be calculated by

$$OME(\psi_i, \psi_f, \mathbf{k}) = \lim_{\mathbf{q}\to 0} \frac{1}{\mathbf{q}^2} \left| \langle \psi_f(\mathbf{k}) | \exp(-i\mathbf{q}\cdot\mathbf{r}) | \psi_i(\mathbf{k}+\mathbf{q}) \rangle \right|^2 \tag{4.14}$$

$$\equiv \left| \langle \psi_f(\mathbf{k}) | \mathbf{u}\cdot\mathbf{r} | \psi_i(\mathbf{k}) \rangle \right|^2, \tag{4.15}$$

where $\mathbf{u}$ is a unit vector along $\mathbf{q}$, ψ_i and ψ_f are the initial and final states' wavefunctions, respectively, and $\mathbf{k}$ is the crystal momentum vector. It is important to note here, that the perturbation vector $\mathbf{q}$ can be chosen arbitrarily, but in practice it is useful to calculate the OMEs for a very small perturbation for each of the directions x, y, z and weight the results according to the polarisation vector of the incoming light $\mathbf{z}$.

Having discussed the calculation of matrix elements for electronic excitations due to the incoming light, the optical properties based on the electronic structure can be calculated. With the discussion above the imaginary part ε_2 of the dielectric function ε given by

$$\varepsilon = \varepsilon_1 + i\varepsilon_2, \tag{4.16}$$

where ε_1 is the real part of the dielectric function, can be calculated. Within the OptaDOS programme [81] the imaginary part of the dielectric function ε_2 is evaluated as

$$\varepsilon_2(\omega) = \frac{\pi e^2}{\varepsilon_0 \Omega} \sum_i^{occ.} \sum_f^{unocc.} \int_{BZ} \frac{d\mathbf{k}}{(2\pi)^3} \left| \langle \psi_f(\mathbf{k}) | \mathbf{u}\cdot\mathbf{r} | \psi_i(\mathbf{k}) \rangle \right|^2 \delta(\varepsilon_f(\mathbf{k}) - \varepsilon_i(\mathbf{k}) - \hbar\omega), \tag{4.17}$$

where e is the electron charge, ε_0 is the vacuum permittivity, Ω is the volume of material considered, δ is a delta function, ε_i and ε_f are the energies of the initial and final state, respectively, and $\hbar\omega$ is the photon energy.

With ε_2 the Kramers-Kronig relations can be used to calculate the real part ε_1 [118]. Having obtained the full dielectric function ε the other optical properties can be expressed as a function of it. The complex refractive index N is given by

$$N = n + ik, \tag{4.18}$$

$$n^2 = \frac{1}{2}\left(\sqrt{\varepsilon_1^2 + \varepsilon_2^2} + \varepsilon_1\right), \tag{4.19}$$

$$k^2 = \frac{1}{2}\left(\sqrt{\varepsilon_1^2 + \varepsilon_2^2} - \varepsilon_1\right). \tag{4.20}$$

The absorption coefficient α is calculated as

$$\alpha(\omega) = \frac{2k\omega}{c}, \tag{4.21}$$

where ω is the photon's angular frequency and c is the speed of light in vacuum. Finally the reflection coefficient R is calculated as

$$R = \frac{(n-1)^2 + k^2}{(n+1)^2 + k^2}. \tag{4.22}$$

4.3 3-Step - Step 1 - Excitation Probability

The first step of the the 3-step model is the excitation of electrons from an occupied valence state into an unoccupied conduction state. The overall probability of excitation is dependent on the polarisation dependent transition probability between the considered pairs of initial and final states, the light intensity within the considered volume of material, and the occupations of the initial and final states. All these aspects will be discussed in more detail in the following sections.

4.3.1 3-Step Excitations

In Section 4.2 the probability of an electronic excitation due to the presence of light and its electric field has been discussed in detail. The same considerations apply for the calculation of a specific excitation probability between two Bloch states. The same equation for the optical matrix elements (OMEs) given in Equation (4.14) can be used here, so

$$OME(\psi_i, \psi_f, \mathbf{k}) \equiv |\langle \psi_f(\mathbf{k}) | \mathbf{u} \cdot \mathbf{r} | \psi_i(\mathbf{k}) \rangle|^2 ,$$

and one further has to include the delta function used in Equation (4.16) to ensure energy conservation during the excitation process. With this the excitation probability is given by

$$P_{excite}(\psi_i, \psi_f, \mathbf{k}, \hbar\omega) = |\langle \psi_f(\mathbf{k}) | \mathbf{u} \cdot \mathbf{r} | \psi_i(\mathbf{k}) \rangle|^2 \cdot \delta \left(\varepsilon_f(\mathbf{k}) - \varepsilon_i(\mathbf{k}) - \hbar\omega \right) , \tag{4.23}$$

where ψ_i and ψ_f are the initial and final state wavefunctions, respectively, $\mathbf{u}$ is a unit vector along the light polarisation vector, ε_i and ε_f are the energies of the initial and final state, respectively, and $\hbar\omega$ is the photon energy. The evaluation of the δ function is evaluated using one of the broadening schemes described in Section 2.8.

4.3.2 Light Polarisation Vector

It is always the goal to compare the calculated photoemission response to experimental data. These experiments can have very different conditions with regard to the incident light. The angle of the incident light and its polarisation can vary drastically between different experiments, making it necessary to account for this [119, p. 124]. When calculating the optical properties in the OptaDOS code package, the specific polarisation vector can be accounted for in a number of different ways [81, 120]:

- *polycrystalline* - no specific polarisation is assumed. An average of the response in x, y, z is assumed, i.e. an isotropic average.
- *polarised* - the light's electric field vector is assumed to be along the given x, y, z values in *optics_qdir*. With this a light with specific linear polarisation can be modelled.
- *unpolarised* - the light is assumed to propagate through the material along the vector given by the x, y, z values in *optics_qdir*. The polarisation is assumed to be orthogonal to the propagation direction, i.e. a planar average of polarisations and thus optical response.

With these approaches a wide range of incoming light conditions can be modelled. This relies, as discussed in Section 4.2 on the excitation properties being calculated for each x, y, z direction individually and during the calculation each of them is weighted accordingly.

4.3.3 Light Intensity

A further piece of calculating the excitation probability within a given layer, is the intensity of light at that specific depth in the material. The approach taken in the current implementation is that the light approaching the surface can either be reflected at the surface or penetrate the material. When the light penetrates the material, it can be absorbed by successive layers, meaning only a partial intensity remains after each layer. The reflection coefficient $R(1, \hbar\omega)$ for the first layer and absorption coefficients $\alpha(l, \hbar\omega)$ for all layers are calculated following the procedure described in Section 4.2. The absorption process is taken into account following a Beer-Lambert type approach

[121]. With these values the fraction of light intensity $I(l, \hbar\omega)$ for each layer l can be calculated as:

$$I_{light}(1, \hbar\omega) = 1 - R(1, \hbar\omega), \tag{4.24}$$
$$I_{light}(l, \hbar\omega) = I(l-1, \hbar\omega) \cdot \exp\left(-\alpha(l, \hbar\omega) \cdot t(l)\right), \tag{4.25}$$

where $\hbar\omega$ is the photon energy and $t(l)$ are the layer thicknesses.

4.3.4 Band Occupations

The occupation of electronic states or bands is a function of temperature. The energy of the highest occupied state at temperature $T = 0\,\mathrm{K}$ is the Fermi energy E_F, being able to be represented by an occupation step function centred on E_F. At non-zero temperatures, however, the occupation of electronic states is described by the Fermi-Dirac distribution [86]. Within the current implementation this is also the chosen distribution to calculate the occupation of bands/states both for the initial and final states of excitations. The occupation $O(\varepsilon, T)$ is thus defined as

$$O(\varepsilon, T) = \frac{1}{\exp\left(\varepsilon - E_F / k_B T\right) + 1}, \tag{4.26}$$

where ε is the band's energy, k_B is the Boltzmann constant and T is the temperature. When considering the excitations described in the previous section, the occupation of both bands has to be considered. While the initial band has to be occupied to excite an electron, the final band has to empty to accept the excited electron. With this the occupation based part for the excitation probability $P_{occ.}$ can be defined as

$$P_{occ.}(\varepsilon_i(\mathbf{k}), \varepsilon_f(\mathbf{k}), T) = O(\varepsilon_i(\mathbf{k}), T) \cdot \left(1 - O\left(\varepsilon_f(\mathbf{k}), T\right)\right), \tag{4.27}$$

where $\varepsilon_i(\mathbf{k})$ and $\varepsilon_f(\mathbf{k})$ are the energies of the initial and final band, respectively, and T is the assumed temperature for the photoemission calculation.

4.3.5 Layer Projection

In addition to taking account of the occupation, the model also accounts to the different contributions of each layer of material to the total photoemission response. This can be accomplished by expressing the delocalised states calculated by PW DFT in a localised basis, such as a atomic orbital (AO) basis or Wannier functions [122, 123] and calculating the contributions of all atoms in a layer to the specific state. In this work the CASTEP code is used to calculate slabs' electronic structure and projections, but generally the implementation is agnostic to the code as long as the contributions for all atoms and their orbitals are available for each state at each $\mathbf{k}$ point.

In CASTEP the projection weight $W(n, \mathbf{k})$ for a specific atom is calculated for a LCAO basis [84, 124, 125], as elaborated in Section 2.7 and thus the layer weight $W_l(l, i, s, \mathbf{k})$ for a state i and layer l at a $\mathbf{k}$ point and spin s is defined as

$$W_l(l, i, \mathbf{k}) = \frac{1}{W_i(i, (\mathbf{k})} \sum_{a \in l} \sum_{\mu \in a} \sum_{\nu} T^*_{\mu,i}(\mathbf{k}) T_{\nu,i}(\mathbf{k}) S^{-1}_{\nu,\mu}(\mathbf{k}), \tag{4.28}$$
$$W_i(i, \mathbf{k}) = \sum_{\mu,\nu} T^*_{\mu,i}(\mathbf{k}) T_{\nu,i}(\mathbf{k}) S^{-1}_{\nu,\mu}(\mathbf{k}), \tag{4.29}$$
$$T_{\mu,i}(\mathbf{k}) = \langle \phi_\mu(\mathbf{k}) | \psi_i(\mathbf{k}) \rangle, \tag{4.30}$$
$$S_{\nu,\mu}(\mathbf{k}) = \langle \phi_\nu(\mathbf{k}) | \phi_\mu(\mathbf{k}) \rangle, \tag{4.31}$$
$$\tag{4.32}$$

where a is the atom index, μ and ν are indices of atomic orbitals (AOs) in the LCAO basis, $W_i(i, (\mathbf{k})$ is the sum of contributions from all atoms at a given $\mathbf{k}$ point to normalise $W_l(l, i, (\mathbf{k})$, since it is not guaranteed that $W_i(i, (\mathbf{k}) = 1$, $T_{i,\mu}(\mathbf{k})$ is the overlap integral between the PW state

$\psi_i(\mathbf{k})$ and the AO $\phi_\mu(\mathbf{k})$,and finally $S_{\mu,\nu}(\mathbf{k})$ is the overlap integral between two AOs of the LCAO basis.

With these layer weights the contributions from each layer to an initial state i can be used when calculating a layers optical properties as described in Section 4.2 and thus allows an explicit consideration of each layer in the calculation of the optical response from the surface slab.

4.4 3-Step - Step 2 - Transmission Probability

In the second step of the 3-step model the population of excited electrons has to pass through the photocathode material. Depending on the angle the electron moves with and the scattering probability of the surrounding material, the population of excited electrons is diminished by scattering processes. Each of these aspects is discussed in further detail below.

4.4.1 Internal Propagation and Angle

An electron has to pass through different amounts of material towards the surface depending on the propagation angle $\vartheta_{internal}$. This angle is dependent on the ratio of the normal and transverse components of the electron's momentum vector. While the electron's transverse momentum is easily defined by the $\mathbf{k}_{x,y}$ vectors, the k_z component is not well defined. As a substitute one can take the electron's transverse energy and the electron's total energy after the excitation E_{final}, which contains the two terms that are defined as

$$E_{final} = \varepsilon_i(\mathbf{k}) + \hbar\omega - E_F, \tag{4.33}$$

$$E_{final} = E_{transverse} + E_{kin}, \tag{4.34}$$

$$E_{transverse} = E_x + E_y = \frac{\hbar^2 k_x^2}{2m_e} + \frac{\hbar^2 k_y^2}{2m_e}, \tag{4.35}$$

where $\varepsilon_i(\mathbf{k})$ is the initial band's energy, $\hbar\omega$ is the photon's energy, ω is the photon's angular frequency, $\hbar$ is the reduced Planck's constant, $\mathbf{k}_{x,y}$ are the two transverse momentum vector components in the x, y-plane, and m_e is the electron mass. The equation for the calculation of $E_{transverse}$ is based on the general formula for the energy of a PW. Using the above equations the internal propagation angle w.r.t. to the surface normal can be calculated with the ratio of E_{kin} and E_{final} as

$$\vartheta_{internal} = acos\left(\frac{E_{kin}}{E_{final}}\right), \tag{4.36}$$

$$\vartheta_{internal} = acos\left(\frac{\varepsilon_i(\mathbf{k}) + \hbar\omega - E_F - E_{transverse}}{\varepsilon_i(\mathbf{k}) + \hbar\omega - E_F}\right). \tag{4.37}$$

A visual explanation of the internal and external angles ϑ is given in Figure 4.4. To calculate an electron's total propagation length l_{total} the distance to the surface from the origin atom with the angle in mind is calculated as

$$l_{total} = \frac{z_{surface} - z_{atom}}{cos\left(\vartheta_{internal}\right)}, \tag{4.38}$$

where $z_{surface}$ is the surface's z-coordinate as determined by the density cut-off method described in Section 4.1 and z_{atom} is the z-coordinate of the electron's originating atom.

4.4.2 Scattering Probability

Given the electron's propagation length calculated in the previous section the probability of it scattering during the propagation has to be determined. In the current implementation of the model only non-scattered electrons are assumed to contribute to the total QE and the scattering

probability is expressed as an inelastic mean free path (IMFP) distance. The scattering probability $P_{scatter}$ as a function of the IMFP value λ is

$$P_{scatter} = \exp\left(\frac{\lambda}{l_{total}}\right), \tag{4.39}$$

where l_{total} is the total propagation length.

To calculate the IMFP values for a given material, a number of different approaches are available in the literature, but their applicability for the photoemission conditions need to be carefully considered. The motivation for this discussion is to search for an approach that is applicable in general, rather than implementing a large number of different approaches for each specific material a user of the implemented model might consider to model. This is due to the scattering of particles propagating in a material being connected to a number of different processes with complicated relationships. These processes can include electron-electron scattering, electron-phonon scattering, defect scattering and more. This makes the development of a comprehensive model very difficult.

A large body of literature exists on estimating the path of a material and developing "universal" curves to estimate the energy dependent behaviour of the IMFP distance. One example for such a universal approach is the so called TPP-2M equation by Tanum, Powell and Penn [126, 127] developed to determine the mean free path for the range energy range 50 eV to 2000 eV, so the applicable range is outside the range of interest for this work, but a good example of an approach for a universal model. The formula uses just a few parameters, of which some are universal, such as the free electron plasmon energy E_p, and others are material dependent, such as the band gap energy E_g, density ρ, or the number of valence electrons N_v. The model's equation is given by [127]

$$\lambda = \frac{E}{E_p^2[\beta \ln(\gamma E) - (C/E) + (D/E^2)]}, \tag{4.40}$$

$$\beta = -0.1 + 0.944(E_p^2 + E_g^2)^{-1/2} + 0.069\rho^{0.1}, \tag{4.41}$$

$$\gamma = 0.191\rho^{-1/2}, \tag{4.42}$$

$$C = 1.97 - 0.91U, \tag{4.43}$$

$$D = 53.4 - 20.8U, \tag{4.44}$$

$$U = N_v \cdot \rho/M = E_p^2/829.4, \tag{4.45}$$

$$E_p = 28.8(N_v\rho/M)^{1/2}, \tag{4.46}$$

where E is the propagating electron's energy, E_p is the free electron plasmon energy, E_g is the materials band gap, ρ is the materials density in gcm^{-3}, N_v is the materials number of valence electrons, and M is the materials molecular weight. While the necessary values for evaluating the equation are easily obtainable, the authors state, that their model is suited for the range energy range 50 eV to 2000 eV. With this the TPP-2M equation is not suitable for the use with photon energies in the visible to ultraviolet. Indeed the TPP-2M calculated IMFP values for Cu shown in Figure 4.3 are consistently below 1 Å, which is well below the curve by Nagy and Echenique curve throughout the entire range of plotted values.

For the specific case of Cu, a further equation by Nagy and Echenique [128] is available to describe an energy dependent IMFP curve. The authors calculate the scattering rate of a fast electron moving through an electron gas with degenerate energy levels, construct an equation for the case of Cu, and find reasonable agreement when comparing to a set of experimental data obtained by Bourke and Chantler using high-accuracy X-ray absorption fine structure (XAFS) measurements

[129]. The resulting Nagy-Echenique equation is given by

$$g_1(x) = \ln(x-1) + \left(\frac{8}{3} - 2\ln 2\right), \tag{4.47}$$

$$g_2(x) = \Theta(2-x) \cdot \left[\frac{2}{3}\sqrt{(2-x)^3} + 2\sqrt{2-x} + \ln\left|\frac{\sqrt{2-1}-1}{\sqrt{2-x}+1}\right|\right], \tag{4.48}$$

$$l(x) = \frac{4\pi}{3} v_F \frac{x}{g_1(x) - g_2(x)}, \tag{4.49}$$

$$x = E/E_F, \tag{4.50}$$

$$v_F = \sqrt{2E_F}, \tag{4.51}$$

where E is the energy of the propagating electron, E_F is the Fermi energy. Nagy and Echenique calculate a Fermi energy of $E_F = 6.9\,\text{eV}$ for Cu and calculate based on this a curve for the energy dependent IMFP. This curve is shown in Figure 4.3. While the given curve for Cu has reasonable agreement with experimental data, the transferability of this approach to other materials is not clear. Since the Nagy-Echenique curve is reported to have good agreement with experimental measurements [128], the TPP-2M curve is as expected not useful for the PE calculations.

The approach mostly used during this work is the spectroscopic constant. The IMFP is assumed to be independent of electronic energy within a small interval of energy and for each material the spectroscopic constant can be set. Two ways to define this constant by the user have been implemented thus far. The first one is to assume the same IMFP for all layers within the slab model, regardless of material type. This is of course not always appropriate, but allows calculations if a value for a specific material is not available. This option is also shown in Figure 4.3.

An extension of the single IMFP constant has also been implemented, where each layer explicitly being considered in the photoemission calculation can be assigned an individual IMFP constant. If for example an interface slab model has 3 layers of material B and 8 layers of material A, the code accepts a list of 11 values and uses them to calculate the weighted IMFP for each layer. This is done using a weighted sum by

$$IMFP_{eff}(n) = \sum_{l=1}^{n} \frac{t(l) * IMFP(l)}{\sum_{l=1}^{n} t(l)}, \tag{4.52}$$

where n is the layer index, $t(l)$ is the layer thickness and $IMFP(l)$ are the user given constants for each layer. For the bulk approximation the IMFP of the innermost explicit layer is assumed for all layers. This allows $IMFP_{eff}$ to represent the layer ordering and give a better approximation in heterogenous surface slab models.

While the discussed approaches are either not applicable for the expected conditions of the photoemission calculations or are not able to satisfy the energy dependence of the scattering probability/IMFP the focus during this work has been on finalising the implementation of the photoemission model to give consistent results. The scattering probability is a modular part of the implementation. Thus, there should be no problem in the future to implement a more complete description of the scattering processes of electrons propagating through the material. One possible approach could be the use of the formula discussed by Ziaja et al. [130]. It requires only two material dependent constants and allows the energy dependent treatment for the scattering rate and thus IMFP.

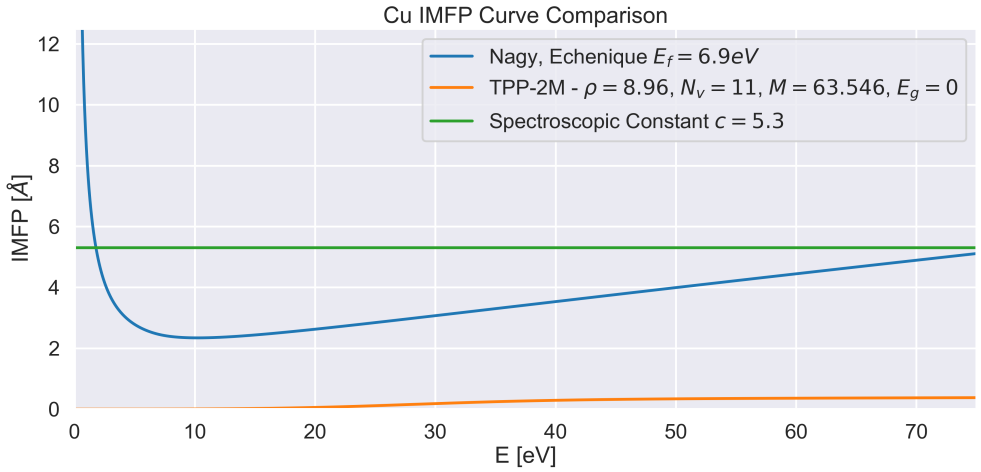


Figure 4.3: Comparison of three different approaches to describe the scattering probability of an electron propagating through Cu. The orange TPP-2M[126, 127] curve clearly shows a severe underestimation of the expected IMFP values, while the curve by Nagy and Echenique [128] shows much more reasonable IMFP values. The constant approach is a very easily usable, but misses the energy dependence of the IMFP, as can be seen from the changing difference between the constant and Nagy-Echenique-curve.

4.5 3-Step - Step 3 - Surface Emission

In the final step of the 3-step model the electron has to pass across the surface barrier and be emitted into the vacuum, where it could then be experimentally detected and characterised. This can also be seen as a cut-off filter for the population of excited electrons that have not been scattered during their propagation to the surface.

4.5.1 External Emission Angles

In an ARPES experiment two different angles, i.e. the polar angle ϑ and azimuthal angle φ are measured. These are also calculated by the current implementation of the model.

When calculating the electron's ϑ angle after the emission from the surface, a similar approach to the internal propagation angle can be used. As stated in the previous section, within this emission model the electron's transverse momentum, and thus transverse energy, is assumed to be conserved during the emission process. The perpendicular momentum $k_\perp$, however, is not conserved while passing through the surface. The electrons loose the energy of the work function W, but with the transverse energy conserved, the angle of emission changes. In a similar fashion to calculating the internal propagation angle in Section 4.4.1 the external emission angle is evaluated as

$$E_{vac} = E_F + W, \tag{4.53}$$

$$E_{out} = \varepsilon_i(\mathbf{k}) + \hbar\omega - E_{vac}, \tag{4.54}$$

$$E_{out} = E_{transverse} + E_{kin,out}, \tag{4.55}$$

$$\vartheta_{external} = acos\left(\frac{E_{kin,out}}{E_{out}}\right), \tag{4.56}$$

$$\vartheta_{external} = acos\left(\frac{\varepsilon_i(\mathbf{k}) + \hbar\omega - E_{vac} - E_{transverse}}{\varepsilon_i(\mathbf{k}) + \hbar\omega - E_{vac}}\right), \tag{4.57}$$

where E_F is Fermi energy, W is the work function, $\varepsilon_i(\mathbf{k})$ is the initial band energy of the electron, $\hbar$ is the reduced Planck's constant, ω is the photon's angular frequency, and $E_{transverse}$ is the

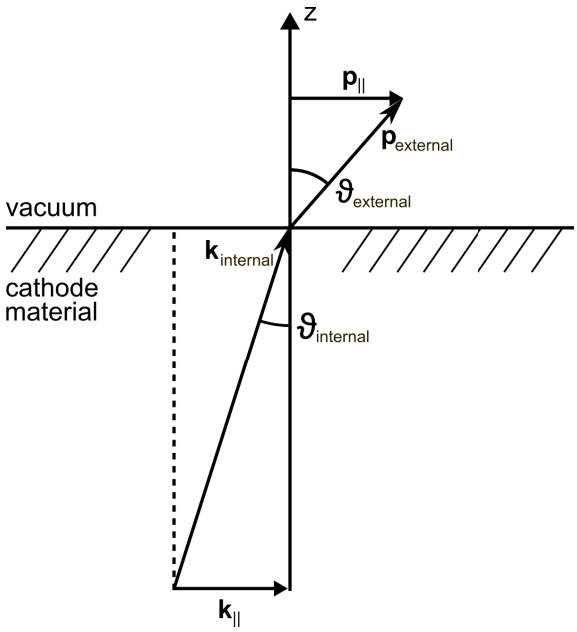


Figure 4.4: Diagram of the electron momenta during propagation and after emission from the surface. The transverse momentum is conserved while passing from the cathode into the vacuum. The momentum along z is diminished when the electron looses the energy of the WF. Hence the internal propagation angle $\vartheta_{internal}$ is smaller than the emission angle $\vartheta_{external}$ w.r.t. the surface normal. Based on Figure 6.5 in the book "Photoemission Spectroscopy" by Hüfner [131].

transverse energy as calculated in Section 4.4.1. A visual explanation of the internal and external angles ϑ is given in Figure 4.4. For the azimuthal φ angle w.r.t. the y-axis the calculation uses the ratio between the transverse energy components along the Cartesian x/y-axes, as

$$\varphi = \arctan\left(\frac{E_x}{E_y}\right), \tag{4.58}$$

where E_x and E_y are the transverse energy components as defined in Equation (4.35). Thus the range of φ is from 0°, i.e. fully along y-axis, to 90°, i.e. fully along x-axis. This is of course not the full 360° range φ can normally assume as this only represents the positive quadrant. This limitation stems from how the grid of $\mathbf{k}$ points in reciprocal space is constructed during the calculation of the electronic structure. This grid is routinely symmetry reduced by removing symmetry equivalent points to reduce computational requirements. Further work would be required to implement the full treatment of φ in future versions of the model, but is certainly possible by applying the available symmetry information within OptaDOS.

4.5.2 Surface Transmission

For the electron to transmit across the surface after propagation through the photocathode, two conditions must be fulfilled. Firstly the electron's energy after excitation must be high enough to pass across the potential step with the height of the work function W and secondly the electron has to pass from the Bloch band in the material into a free electron state in the vacuum.

To describe the first condition, a modified Heaviside step function Θ' is used and defined as

$$\Theta'(E_{kin,out}) = \begin{cases} 1, & E_{kin,out} \geq 0 \\ G(E_{kin,out}), & E_{kin,out} < 0 \end{cases}, \tag{4.59}$$

where $E_{kin,out}$ is the kinetic energy component in vacuum along the surface normal as calculated in Section 4.5.1 and G is a Gaussian broadening function defined as

$$G(E_{kin,out}) \equiv \frac{1}{\sqrt{2\pi}\sigma} \exp\left(-\frac{1}{2}\frac{(E_{kin,out})^2}{\sigma^2}\right), \tag{4.60}$$

$$\sigma = k_B T, \tag{4.61}$$

where k_B is the Boltzmann constant and T is the assumed temperature for the photoemission calculation. This way the general temperature effects of increasing emission [132], line broadening [133], and increases in MTE [134–136] can be estimated.

Secondly the change of an electron from a Bloch state within the material to a free electron state in vacuum has to be considered. The current implementation is based on a "semi-classical" approach put forward in Hüfner and formalised in their Equation (6.11) [113]. The Bloch state within the material is considered to be expanded in a PW basis analogous to Section 2.4.1 and implemented in CASTEP [73] as

$$\psi(\mathbf{k}) = \sum_{\mathbf{G}} u\left(\mathbf{k}, \mathbf{G}\right) \exp\left(i\left(\mathbf{k}+\mathbf{G}\right)\cdot\mathbf{r}\right), \tag{4.62}$$

where $\mathbf{k}$ is the crystal momentum vector, is the $\mathbf{G}$ is the set of reciprocal lattice vectors, and $\mathbf{r}$ is the momentum space coordinate. Each plane wave propagating towards the surface, i.e. $(\mathbf{k}+\mathbf{G})_\perp > 0$, can match onto a plane wave in free space. Thus the transmission probability $T(E_{kin,out}, \mathbf{k})$ is the sum of contributions of plane waves to the Bloch state before transmitting across the surface. So together with the first condition described above one gets

$$T_{surface}(E_{kin,out}, \mathbf{k}) = \Theta'(E_{kin,out}) \left| \sum_{(\mathbf{k}+\mathbf{G})_\perp > 0} u\left(\mathbf{k}, \mathbf{G}\right) \right|^2. \tag{4.63}$$

With this the total probability of electron emission from the surface can be estimated, but further effects, as the surface plasmons, are currently not included [113]. Since these plasmons can inelastically scatter electrons transmitting through the surface, this would be an area where further work could improve the description of the transmission probability.

4.6 1-Step Model

4.6.1 Excitation and Optical Matrix Elements

Rather than adopting the full description of a time reversed LEED state as described in Section 3.4, the final state used in the current implementation of the 1-step model is a dampened plane wave. This approach has been used before in literature [47, 105, 137] with some success. This can be seen as a first iteration, that has been relatively easy to implement within the CASTEP code. As discussed in Sections 2.3 and 2.4.1 a Bloch state expanded in a plane wave basis has the form of

$$\psi(\mathbf{k}) = \sum_{\mathbf{G}}^{\mathbf{G}_{max}} u(\mathbf{k}, \mathbf{G}) \exp(i(\mathbf{G}+\mathbf{k})\cdot\mathbf{r}). \tag{4.64}$$

The final state for the 1-step model, however, is a free electron wave, which needs to be expressed in the plane wave basis. Given the energy of the electron after emission, i.e. E_{free}, the wave vector of the free electron wave $\mathbf{p}_{free}$ can be calculated following the relation

$$E_{free} = \frac{\hbar^2 \mathbf{p}_{free}^2}{2m_e}, \tag{4.65}$$

where $\hbar$ is the reduced Planck constant, and m_e is the electron mass. Analogous to the 3-step model the final electron momentum $\mathbf{p}_{free}$ has the transverse momentum component $\mathbf{p}_\parallel$ and the

normal momentum component $\mathbf{p}_\perp$. Furthermore, $\mathbf{p}_\parallel$ is assumed to be conserved during the emission process , so $\mathbf{p}_\parallel = \mathbf{k}_\parallel$.

To start constructing the final state in the PW basis, one can consider the transverse momentum first. The surface normal is assumed to be along the Cartesian z-axis. Given the initial Bloch state momenta $k_{x,y}$ and transverse momentum being conserved, the final state state is given by

$$\psi^{free}(p_x) = \sum_{G_x}^{G_{x,max}} u(k_x, G_x) \cdot \exp(i(G_x + k_x) \cdot r_x) \cdot \delta_{G_x,0} \ , \tag{4.66}$$

$$\psi^{free}(p_y) = \sum_{G_y}^{G_{y,max}} u(k_y, G_y) \cdot \exp(i(G_y + k_y) \cdot r_y) \cdot \delta_{G_y,0} \ . \tag{4.67}$$

Finally the normal momentum p_z can be calculated as

$$p_z = \sqrt{\frac{2m_e}{\hbar^2}\left(\varepsilon_i(\mathbf{k}) + \hbar\omega - E_F - W - E_\parallel(\mathbf{k})\right)}, \tag{4.68}$$

where m_e is the electron mass, $\hbar$ is the reduced Planck constant, $\varepsilon_i(\mathbf{k})$ is the energy of the initial electronic state, i.e. Bloch state, ω is the photon's angular frequency, E_F is the systems Fermi level, W is the systems WF and $E_\parallel(\mathbf{k})$ is the electrons transverse energy. The construction of the final state is analogous to Equation (4.66) and so

$$\psi^{free}(p_z) = \sum_{G_z}^{G_{z,max}} u(k_z, G_z) \cdot \exp(i(G_z + k_z) \cdot r_z) \cdot \delta_{G_z+k_z,\ p_z}. \tag{4.69}$$

It can not be guaranteed that a value of G_z exists, where

$$G_z + k_z = p_z,$$

since the photon energy is a continuous parameter. So the delta function $\delta_{G_z+k_z,\ p_z}$ is evaluated using a Gaussian broadening of the form

$$\delta_{G_z+k_z,\ p_z} \equiv \frac{1}{\sqrt{2\pi}\sigma} \cdot \exp\left(-\frac{1}{2}\frac{(G_z + k_z - p_z)^2}{\sigma^2}\right), \tag{4.70}$$

$$\sigma = 0.01\frac{1}{r_B} \qquad with \ \ \frac{\hbar^2\mathbf{k}^2}{2m_e} \Rightarrow \sigma = 0.001\,361\,\mathrm{eV} = 1.361\,\mathrm{meV} \ , \tag{4.71}$$

where r_B is the Bohr radius. With this the same procedure for evaluating the optical matrix elements (OMEs) for the 3-step model given in Section 4.3.1 and it follows

$$OME^{free}(\psi_i, \mathbf{k}, \hbar\omega, W) \equiv \left|\left\langle \psi^{free}(\mathbf{k}, \hbar\omega, W)|\mathbf{u}\cdot\mathbf{r}|\psi_i(\mathbf{k})\right\rangle\right|^2, \tag{4.72}$$

where ψ_i is the initial electronic state, $\hbar\omega$ is the photon energy, and W is the model's work function. With this the excitation probability from an initial Bloch state into a free electron state can be calculated and the depth dependent damping will be considered in the next section.

Since the transverse Bloch momentum $\mathbf{k}_\parallel$ is an important parameter to calculating the OME, the "correct" value is required. As discussed in Section 4.11 the transverse momentum for many electronic states is greatly dependent on the surface slab's cell. If the surface slab is not a primitive cell structure, the states from the edge of the BZ appear to be folded towards the origin. For a 2×2 for example, two sets of bands appear at the origin (Γ point). This greatly changes their associated transverse momentum and thus has an effect on the OME calculation. As discussed in Section 4.11, expanding each $\mathbf{k}$ point into a grid spaced by the x, y components of the BZ, $\mathbf{G}_x, y$, gives comparable answers for both PC and SC systems. The contributions on this grid used to calculate a weighted sum of possible excitations for each state, so an analogous expansion of the 1-Step model OMEs should be possible. As of the writing of this work, the OME calculation does not have this expansion implemented and thus will be part of the future work.

4.6.2 Propagation, Emission Angle and finite Penetration Depth of Final State

The same considerations discussed in Section4.4.1 for the propagation angle dependent scattering probability apply within the adapted 1-Step model. The propagation angle of the electron after excitation is calculated analogously to the angle within the 3-Step model. This attenuation length is treated analogous to the IMFP approach described in Section 4.4.2. The propagation probability is thus calculated as:

$$P_{scatter} = \exp\left(\frac{\lambda}{l_{total}}\right), \tag{4.73}$$

where λ_i is the optionally energy dependent IMFP value and l_{total} is the propagation length as described in Section 4.4.1.

Furthermore, the emission probability is limited by the discussion on the final kinetic energy from Section 4.5.2. The same approach of using a modified Heaviside step function with a delta function evaluated by a Gaussian is used. For completeness, this gives

$$\begin{aligned}
\Theta'(E_{kin,out}) &= \begin{cases} 1, & E_{kin,out} \geq 0, \\ G(E_{kin,out}), & E_{kin,out} < 0, \end{cases} \\
G(E_{kin,out}) &\equiv \frac{1}{\sqrt{2\pi}\sigma} \exp\left(-\frac{1}{2}\frac{(E_{kin,out})^2}{\sigma^2}\right), \\
\sigma &= k_B T,
\end{aligned}$$

where $E_{kin,out}$ is the final kinetic energy of the electron outside the surface, k_B is the Boltzmann constant, and T is the assumed temperature for the photoemission calculation.

4.7 Applying Electrical Fields

When conducting photoemission experiments it is common to apply a bias on the photocathode. This helps with extracting the low energy electrons otherwise accumulating close to the photocathode and lowers the cathode's WF a predictable amount [138]. The photoemission model is able to take this WF lowering into account as well as the effects of electron emission through the modified surface barrier. In this work the surface barrier is assumed to be represented by a Schottky-Nordheim (SN) barrier and the calculation of the field emission contribution follows the discussions by Forbes and Deane [139–141].

The WF lowering is calculated analogously to the approach by Schottky [142] to give the effective WF W_{eff} as

$$W_{eff} = W - \sqrt{\frac{e^3 F}{4\pi\varepsilon_0}}. \tag{4.74}$$

In addition to the lower WF, the shape of the barrier is also changed. The SN barrier M_{SN} can be described as a function of the distance from the surface z

$$M_{SN}(z) = h - eFz - \frac{e^2}{16\pi\varepsilon_0 z}, \tag{4.75}$$

$$h = W - \varepsilon_i(\mathbf{k}) + \hbar\omega - E_F, \tag{4.76}$$

where h is the barrier height for an electron with the energy $\varepsilon_i(\mathbf{k}) + \hbar\omega$, e is the electron charge, F is the field strength, and ε_0 is the vacuum permittivity. Some examples for the barrier shape at a range of different field strengths are shown in Figure 4.5. From the plot the barrier height's gradual decrease with increased field strength and more and more altered shape is evident. In addition the plot in Figure 4.5 shows the gradual decrease of the barrier's width when the field strength is increased. This is most evident at field strengths above $1\,\mathrm{GV\,m^{-1}}$ shown in Figure 4.5, where the extent of the barrier is below 50 Å. This permits electrons with an energy below the barrier height to possibly tunnel through and escape into the vacuum. This probability is also represented in the

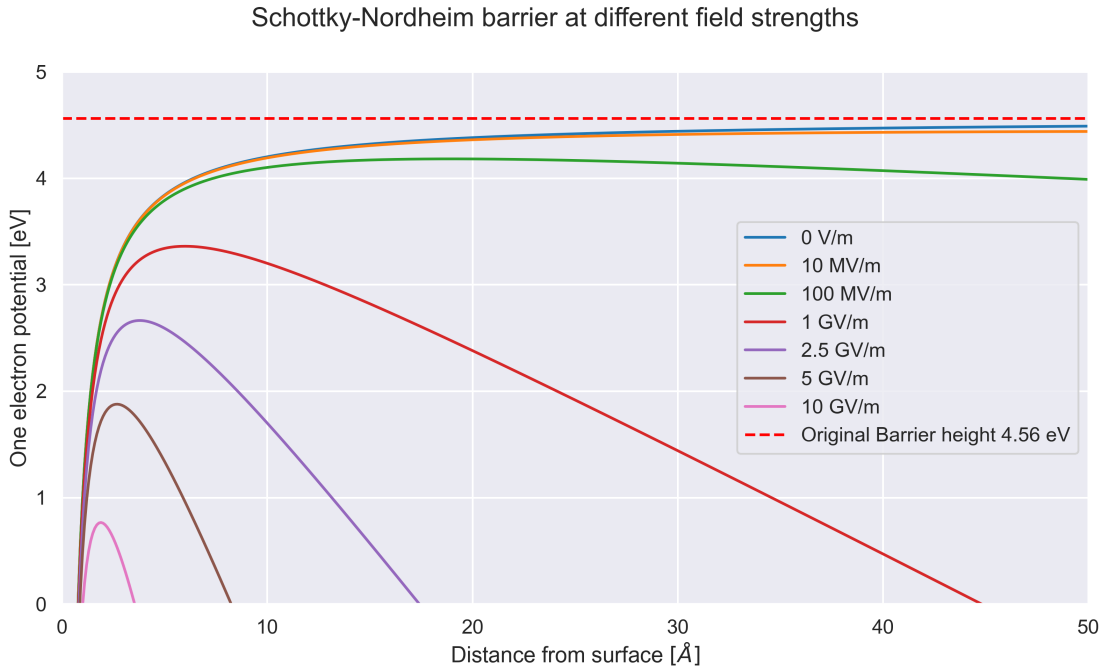


Figure 4.5: Plot showing the Schottky-Nordheim barrier's shape as a function of distance from the surface z at different field strengths. The gradual lowering of the barrier height with increasing field strength and alteration to the barrier shape are evident.

photoemission model.

To calculate these tunnelling probabilities $D(h, F)$ exactly one would need to solve the Schrödinger equation for the tunnelling process, which is not easily possible. It can, however, be approximated using the Jeffreys-Wentzel-Kramers-Brillouin (JWKB) approach [139] and defining a parameter for the tunnelling probability $G(h, F)$ as

$$G(h, F) = \frac{2\sqrt{2m_e}}{\hbar} \int \sqrt{M_{SN}(z)}\, dz, \tag{4.77}$$

where m_e is the electron mass and the integral's limits are the z values where the barrier M_{SN} equals zero. The transmission probability through the barrier $D_{SN}(h, F)$ is given by the equation

$$D_{SN}(h, F) = \frac{P \cdot e^{-G}}{1 + P \cdot e^{-G}}, \tag{4.78}$$

where P is called the tunnelling prefactor by Forbes [141]. In this work it is assumed that the surface potential barrier described by M_{SN} is smooth enough to assume $P = 1$, as is described by Forbes [141]. To solve the integral in Equation (4.77) it is useful to consider the tunnelling probability through a triangular barrier as described by

$$M_t(z) = h - eFz\ , \tag{4.79}$$

where h is the barrier height from Equation (4.76), e is the electronic charge, and F is the field strength. For this barrier type it is possible to calculate the integral $G(h, F)$ explicitly, which yields:

$$G_t(h, F) = \frac{4\sqrt{2m_e}}{3e\hbar} \frac{h^{\frac{3}{2}}}{F}, \tag{4.80}$$

where m_e is the electron mass, $\hbar$ is the reduced Planck constant, h is barrier height from Equation (4.76), and F is the field strength. To adapt this result for the SN barrier, one can define

i	p_i	q_i
0	1	-
1	0.032 705 304 46	0.187 499 344 1
2	0.009 157 798 739	0.017 506 369 47
3	0.002 644 272 807	0.005 527 069 444
4	0.000 089 871 738 11	0.001 023 904 180

Table 4.1: Expansions coefficients given by Forbes and Dean [139] for the series to approximate the function $v\,(l')$. The expansion to the fourth degree is used to calculate the tunnelling properties in this work.

modification value ν as

$$G_{SN} = \nu_{SN} \cdot G_t \ . \tag{4.81}$$

To calculate the final transmission probability through the SN barrier Forbes and Dean [139] further define a variable l' as

$$l' = \frac{e^3}{4\pi\varepsilon_0}\frac{F}{h^2}, \tag{4.82}$$

where e is the electron charge, ε_0 is the vacuum permittivity, F is the field strength and h is barrier height from Equation (4.76). The value ν_{SN} can then be calculated using a function $v(l')$, for which Forbes [143] found a "simple good approximation" to be

$$v\,(l') \approx 1 - l' + \frac{1}{6} l' \ln\,(l')\,. \tag{4.83}$$

In the work by Forbes and Dean [139] another approximation for $v(l')$ is given as

$$v\,(l') \approx (1 - l') \sum_{i=0}^{j} p_i l'^i + (l' \ln l') \sum_{i=1s}^{j} q_i l'^{i-1}, \tag{4.84}$$

where j describes the degree of expansion for the approximation and p and q are the expansion coefficients, which are given in Table 4.1. Forbes and Dean [139] state in their work that the series with $j = 4$ has an absolute error $|\varepsilon| \ \leq \ 8 \times 10^{-10}$ or less for all possible values of l'. This is also the expansion series used to calculate the exponent $G_{SN}(h, F)$ and the subsequently tunnelling probability $D(h, F)$ for electrons being excited into states lying below the WF W_{eff} energy.

With the lowering of the WF and tunnelling probability the field emission of electrons has to be considered, as well. For this the tunnelling probability of electrons in conduction bands and their occupation at non-zero temperatures can be combined to estimate the total contribution by field emission FE_{total} as

$$FE_{total}(h, F, T, \mathbf{k}) = \frac{1}{A} \sum_{\varepsilon_f(\mathbf{k})} D_{SN}(h, F) \cdot n_{FD}(\varepsilon_f(\mathbf{k}), T) \ , \tag{4.85}$$

where A is the surface cell's area, n_{FD} is the Fermi-Dirac occupation for the set of conduction bands as calculated in Section 4.3.4.

4.8 Bulk Approximation

While photoemission is a surface phenomenon it is not feasible to explicitly calculate all the layers of material, that can meaningfully contribute to the photoemission response. Taking a hypothetical inelastic mean free path (IMFP) λ_i =10 Å and interlayer distance of 3 Å, it requires a layer of

material with the depth z

$$\begin{aligned} 0.001 &= \exp\left(\frac{-z}{10\text{Å}}\right), \\ \ln(0.001) &= \frac{-z}{10\text{Å}}, \\ -10\text{ Å}\cdot\ln(0.001) &= 69.01\text{ Å} = z \end{aligned}$$

or 23 layers deep to have an emission probability lower than 1×10^{-3}. A slab always has a surface on either side, so would need a total of 46 layers. Calculating a primitive cell with this many atoms is possible with current HPC systems, but if a larger supercell is required to accurately represent a surface, this quickly becomes intractable. At the same time the density of states (DOS) of a layer within a slab normally converges to the bulk DOS much quicker than the 23 layers required for the emission probability. Thus a bulk like slab can be extrapolated from a inner slab layer that has an electronic density sufficiently similar to the bulk density. This is the approach taken within the photoemission model. The innermost layer defined in the layer assignment scheme of Section 4.1 is repeated until a specified multiple of the IMFP distance is reached. By default this value is 10, which gives an emission probability x of

$$\begin{aligned} x &= \exp\left(\frac{-10a}{a}\right), \\ x &= \exp\left(-10\right) = 4.540\times10^{-5}, \end{aligned}$$

and can further be changed by the user. The absorption coefficient is assumed to be equal to the innermost explicit layer for all extended layers, whereas the light intensity and emission probability are calculated for all layers individually.

4.9 Putting it all together: QE and MTE

Having discussed all parts necessary to evaluate an emission probability in the 3-step and 1-step model they can be put to together to calculate the quantum efficiency (QE) contribution from a single atom located in a layer of material. For this a prefactor of $1/\text{A}$, the surface cell's area A, has to be considered, too. For the 3-step model one gets

$$\begin{aligned} QE_{n,3step}(n,\hbar\omega) = \frac{1}{A}\sum_{\mathbf{k}}\sum_{\psi_i}\sum_{\psi_f} & P_{excite}(\psi_i,\psi_f,\mathbf{k},\hbar\omega)\cdot W_l(l(n),i,\mathbf{k})\cdot I_{light}(l(n),\hbar\omega) \\ & \cdot P_{occ.}(\varepsilon_i(\mathbf{k}),\varepsilon_f(\mathbf{k}),T)\cdot P_{scatter}\cdot T_{surface}(E_{kin,out},\mathbf{k})\cdot(1+D_{SN}(h,F)), \quad (4.86) \end{aligned}$$

where n is the atom index, l is the layer index the atom is located in, $\hbar\omega$ is the photon energy, P_{excite} is the 3-step excitation probability from Equation (4.23), W_l is the projected layer weight from Equation (4.28), I_{light} is the layer dependent light intensity from Equation (4.24), $P_{occ.}$ is the combined initial and final state occupation from Equation (4.27), $P_{scatter}$ is the scattering probability from Equation (4.39), $T_{surface}$ is the surface transmission probability from Equation (4.63), and D_{SN} is the Schottky-Nordheim barrier transmission probability from Equation (4.78) in the case an electrical field is assumed to be applied.

Similarly for the 1-step model one gets

$$\begin{aligned} QE_{n,1step}(n,\hbar\omega) = \frac{1}{A}\sum_{\mathbf{k}}\sum_{\psi_i} & OME^{free}(\psi_i,\mathbf{k},\hbar\omega,W)\cdot W_l(l(n),i,\mathbf{k})\cdot I_{light}(l(n),\hbar\omega) \\ & \cdot O(\varepsilon_i(\mathbf{k}),T)\cdot P_{scatter}\cdot\Theta'(E_{kin,out})\cdot(1+D_{SN}(h,F)), \quad (4.87) \end{aligned}$$

where n is the atom index, l is the layer index the atom is located in, $\hbar\omega$ is the photon energy, OME^{free} is the free electron state OME from Equation (4.72), W_l is the projected layer weight

from Equation (4.28), I_{light} is the layer dependent light intensity from Equation (4.24), O is the initial state occupation from Equation (4.26), $P_{scatter}$ is the scattering probability from Equation (4.73), Θ' is the modified heaviside step function from Equation (4.59), and D_{SN} is the Schottky-Nordheim barrier transmission probability from Equation (4.78) in the case an electrical field is assumed to be applied.

In the output of the program, the calculated QE is reported for each atom in the half of the slab the calculation is based on. The same approach to calculate QE for the bulk approximation described in Section 4.8, but all layers of material summed together. Hence only one value is reported for the bulk QE. To determine the total QE of the surface model, the atomic contributions are simply summed together and the bulk approximation value is added as

$$QE_{total}(\hbar\omega) = \left(\sum_{n}^{n_{max}} QE(n, \hbar\omega)\right) + QE_{bulk}(\hbar\omega) \tag{4.88}$$

Having found a description for the QE of the photoemission, the second important quantity from the PE calculation is the mean transverse energy (MTE). This quantity is evaluated as a weighted sum of the emission probability contribution from a single state ψ, QE_ψ, with its associated transverse energy $E_\parallel$ so one gets for the 3-step model

$$\begin{aligned} QE_{\psi,3step}(\psi_i, \psi_f, \mathbf{k}, n, \hbar\omega) = \frac{1}{A} P_{excite}(\psi_i, \psi_f, \mathbf{k}, \hbar\omega) \cdot W_l(l(n), i, \mathbf{k}) \cdot I_{light}(l(n), \hbar\omega) \\ \cdot P_{occ.}(\varepsilon_i(\mathbf{k}), \varepsilon_f(\mathbf{k}), T) \cdot P_{scatter}() \cdot T_{surface}(E_{kin,out}, \mathbf{k}) \cdot (1 + D_{SN}(h, F)), \end{aligned} \tag{4.89}$$

and for the 1-step model one gets

$$\begin{aligned} QE_{\psi,1step}(\psi_i, \mathbf{k}, n, \hbar\omega) = \frac{1}{A} OME^{free}(\psi_i, \mathbf{k}, \hbar\omega, W) \cdot W_l(l(n), i, \mathbf{k}) \cdot I_{light}(l(n), \hbar\omega) \\ \cdot O(\varepsilon_i(\mathbf{k}), T) \cdot P_{scatter}() \cdot \Theta'(E_{kin,out}) \cdot (1 + D_{SN}(h, F)), \end{aligned} \tag{4.90}$$

where the two equations above are just the individual contributions, which are being summed together for QE_n from Equations (4.86) and (4.87) respectively. With these two the MTE more can be evaluated as

$$MTE_{3step}(\hbar\omega) = \frac{\sum_{n,bulk} \sum_{\mathbf{k}} \sum_{\psi_f} \sum_{\psi_i} QE_{\psi,3step}(\psi_i, \psi_f, \mathbf{k}, n, \hbar\omega) \cdot E_\parallel(\mathbf{k})}{QE_{total,3step}(\hbar\omega)}, \tag{4.91}$$

where $\sum_{n,bulk}$ describes a sum over all the explicitly calculated atoms and the bulk approximation, $\mathbf{k}$ is the set of $\mathbf{k}$ points, and ψ_i and ψ_f are the initial and final states, respectively. Analogously the result for the 1-step model is

$$MTE_{1step}(\hbar\omega) = \frac{\sum_{n,bulk} \sum_{\mathbf{k}} \sum_{\psi_i} QE_{\psi,1step}(\psi_i, \mathbf{k}, n, \hbar\omega) \cdot E_\parallel(\mathbf{k})}{QE_{total,1step}(\hbar\omega)}. \tag{4.92}$$

With this the important values for the PE calculation are defined and discussed. Some exemplary outputs for the 3-step model and the 1-step model are given in Appendix A

4.10 Teasing out the Details: Calculating Angle-Resolved Contributions

Having calculated the emission angle for each possible emission it is easily possible to restrict the range of angles considered and calculate data data akin to angle resolved photoemission spectroscopy (ARPES).

Within the current implementation of the model, there are a number of ways to output such angle resolved data. For both sets of angles, i.e. the elevation (ϑ) and azimuthal angle (φ), the

minimum and maximum value are between 0° and 90°. The angle ϑ is assumed to be with respect to the surface normal and the angle φ is assumed to be between 0° (along y axis) and 90° (along x axis).

Firstly, a simple line graph of binding energy (x) versus emission intensity (y) can be calculated. This option is analogous to the energy distribution curves (EDCs) measured for a specific set of angles in an ARPES experiment. The emission contributions are Gaussian broadened with a default width of 0.026 eV, which can be changed by the user, and summed up.

Secondly a number of intensity maps, which are common in ARPES experiments, can be calculated using the photoemission module. A constant binding energy map shows the emissions across the transverse momentum plane (x,y) for a binding energy of choice. One common example is the Fermi surface located at the Fermi energy. The set of **k** points is normally symmetry reduced. To recover the full set of **k** points in the MP grid, the symmetry elements and **k** weights calculated by CASTEP are used by applying the symmetry element matrices to the explicitly calculated **k** points and applying the proper **k** point weight. The transverse momentum (x) versus kinetic energy (y) map gives contributions for the set of possible kinetic energies and total transverse momenta. The symmetry expansion of the **k** point grid is not yet implemented for the transverse momentum versus kinetic energy map.

The contributions in the maps are Gaussian broadened in the energy direction analogous to the EDCs and in the transverse momentum direction the Gaussian broadening is calculated as the full width half maximum (FWHM) of the distance between the **k** points. The bin width for the momentum dimensions is 0.01 Å^{-1} by default and can be changed by the user. The reference kinetic energy for the Fermi level, is also given to allow the conversion to kinetic energy maps. Examples for the transverse energy map and the Fermi surface map for a Cu(100) surface are given in Section 5.3.2. The constant binding energy map shows the Fermi surface structure of the bands clearly. Comparison with experimental ARPES data has not been explicitly performed for this work, but should hopefully allow for more rich data to compare the calculated spectra to.

4.11 Calculating Photoemission from Supercell Models

Calculating the photoemission response curve for a primitive cell (PC) surface structure the direct use of the bloch phase at the $k_{||}$ points to calculate the electron's transverse momentum $p_{||}$ is possible. Examples can be seen in Section 5.3.2. When the structure is changed to a supercell (SC), this approach fails.

This can be easily demonstrated by calculating PE spectrum for a 2×2 supercell for a Cu(100) surface and comparing that to the spectrum of a 1×1 primitive Cu(100) structure. More detail regarding the modelling parameters is given in Section 5.3.2. The two response curves calculated with the direct use of $k_{||}$ are denoted with *crystal* and shown in Figure 5.7.

The bands in the smaller first Brillouin zone (BZ) of a SC, which is the only one explicitly calculated, appear to be 'folded' back towards the origin (Γ). This can be explained by considering the periodicity of the electronic bands and the reciprocal cell. Due to the periodic boundary conditions the reciprocal cells are assumed to be repeated *ad infinitum*. With an increase of cell size in real space to e.g. $2a$, conversely the reciprocal cell length shrinks to $\frac{2\pi}{2a}$. Each of the smaller repeated reciprocal cells, however, contains a set of bands with the primitive cell periodicity $\frac{2\pi}{a}$. Due to this the bands originating in BZs further away from the origin are pushing into the first BZ centred on the origin. This has the overall appearance of a folded set of bands. These sets of bands are distinguishable due to the different BZs as their origin. A visual explanation using a single hypothetical band is shown in Figure 4.6.

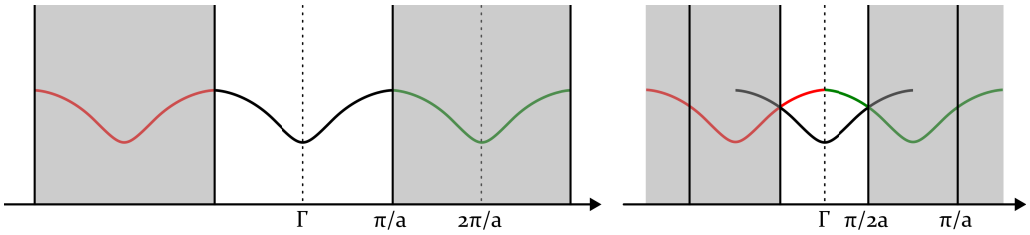


Figure 4.6: Visual explanation for band folding using a single hypothetical band. left: In the primitive cell (PC) with side length a the periodicity of the band and the reciprocal cell are identical and a single band exists in the Brillouin zone (BZ). right: With a 2x supercell of side length $2a$ the reciprocal cell is halved, but the band retains its original periodicity. The bands from the other BZs move into the first BZ and the band appears to be *folded* towards the origin Γ.

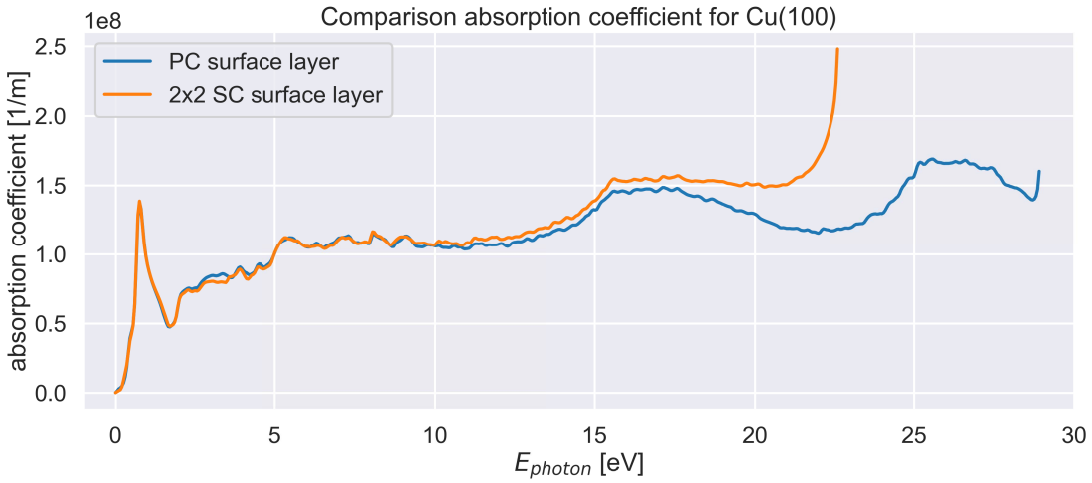


Figure 4.7: Absorption coefficient curves for a Cu(100) PC and 2×2 SC. The curves are nearly identical until they start to diverge due to the lower upper bound for the SC system. This has an effect on lower energies due to the Kramers-Kronig relation used to calculate ε.

With the consideration of how the calculated electronic structure changes going to a supercell structure one can examine their impact on the calculated photoemission properties. More specifically these are the optical properties and the probability of an electron emission. As described in Section 4.2 the optical properties are calculated by an integral over the entire BZ. The excitation probability contributing to e.g. the absorption coefficient are not dependent on the transverse momentum. In addition the bands originate from different BZs and thus one can expect the overlap between the bands to be negligible, making cross excitation very improbable. Indeed when calculating the OMEs for a PC and 2x2 SC surface the values given in Table 4.2 show that exact behaviour of a very small probability for cross excitation between folded and non-folded bands.

In line with this, the absorption coefficients for a PC and 2x2 SC surfaces, discussed in Section 5.3.2, and shown in Figure 4.7 are quite similar and do not contribute significantly to the difference between the two QE curves. The absorption coefficients are for the surface layer in the surface slab models of Cu(100). They are nearly identical for the energy range of interest and the divergence at higher energies is due to the lower upper bound for the 2×2 SC, which has an effect at lower energies due to the Kramers-Kronig relation used to calculate both parts of the dielectric constant ε.

The electron emission probability, however, is very much dependent on electron's transverse mo-

Band	folded	$E_b - E_F$ $[eV]$	OME to PC#96	OME to SC#368	OME to SC#379
PC # 1	no	-9.732	0.3493×10^{-5}		
PC # 96	no	0.843			
SC # 1	no	-9.727		0.3238×10^{-5}	0.3238×10^{-13}
SC # 17	yes	-5.335		0.3281×10^{-5}	0.1215×10^{-3}
SC # 368	no	0.827			
SC # 379	yes	3.505			

Table 4.2: Table showing the band energies at the Γ point, a determination of whether the band is folded, and applicable optical matrix elements for a Cu(100) primitive cell (PC) and 2x2 supercell (SC) structure. The band energies of equivalent bands are within 20 meV between the PC and SC structures. The OMEs for equivalent excitations for both PC and SC are within 10 %. The OME for an excitation between two folded states in the SC is of similar magnitude as the OME for an excitation between two non-folded states. The excitations for SC bands that are dissimilar are at least seven orders of magnitude smaller than for the similar SC bands. All taken together this shows, that the band energies and OMEs are consistent between PC and SC structures, and that the excitations between dissimilar states are small enough to be negligible.

mentum. As described in Section 4.5.2, the electron can only contribute if the orthogonal momentum $p_\perp > 0$. With the band "folded" towards the origin, the transverse momentum of the associated transitions is lowered greatly. To go back to the visual aid in Figure 4.6, this effect is most pronounced for the PC BZ edge at $\frac{\pi}{a}$. This point is folded to the Γ point with no associated transverse momentum. Thus, it can contribute to the overall QE at much lower photon energies in the SC structure compared to the PC structure. This very clearly explains the much stronger QE response of the SC structure compared to the PC structure. The bands folded from the outer parts of the BZ are contributing to the overall QE at much lower photon energies. Furthermore the transverse energy associated with the electron leaving the surface is reduced. This has an effect on the calculated MTE values, too. This is evident from the very different MTE curves in Figure 5.7 comparing the PC and SC structures.

As shown above the optical properties do not differ meaningfully between a PC and SC cell geometry. It is thus possible to get a consistent result for both a PC and SC structure when the correct transverse momentum can be recovered for a SC structure. This band unfolding is not a new problem and approaches for have been available for a while [144–146].

The unfolding of bands, however, starts to get more difficult when calculating interface geometries with materials that have different lattice parameters. The unfolding procedure could be applied using the primitive cell of either material in the interface with different results. One example of this is shown the work by Chen, M and Weinert, M [147]. One of the interfaces consists of a layer of silicene on top of a Ag(111) slab. The unfolding procedure using either of the cells as a base gives different results and the choice of a cell basis is a non-trivial issue.

As stated by Kosugi et al. [148] an unfolding method not relying on a specific cell is a step forward and away from the difficulty of choosing an appropriate cell basis. They propose a basis of free electron waves, i.e. plane waves (PWs), to project the electronic states onto. This approach is furthered by Mayo et al. [149], who take the same plane wave basis to unfold a set of states into a fully unfolded set at a wide range of momentum values. This set can either be folded into a cell of the users choice or used as is.

The approach by Mayo et al. uses the points $\mathbf{k_q}$ located within the SC BZ and the set of SC's reciprocal lattice vectors $\mathbf{G_q}$ calculated as $\frac{\pi N}{a_{sc}}$ with $N \in \mathbb{N}$ to calculate the contributions at momentum values available through a linear combination of $\mathbf{k_q}$ and $\mathbf{G_q}$. It is very handy that the current approach to calculate the electronic structure for the photoemission is using the PW-DFT approach implemented in CASTEP [73], as with this all the necessary values are already readily

available in the code. In addition only the transverse momentum is necessary to calculate the photoemission response consistently between PC and SC structures.

The approach to determine the transverse momentum of any state for the photoemission response calculation is as follows. As described in Section 2.4.1 the plane wave basis calculates the contribution $\tilde{u}_{\mathbf{k},\mathbf{G}}$ for the set of reciprocal lattice vectors $\mathbf{G}$ each shifted by a different $\mathbf{k}$ vector. This can also be thought of as a set of 3D grids with the spacing of $G_{x,y,z}$, where each grid is centred on one of the $\mathbf{k}$ points. We can use these grids and the calculated contributions to recover the transverse momentum associated with a specific band for a SC structure. This approach is referred to the Gkgrid approach from here on.

Throughout this entire work, it is assumed, that the surface lies within the x, y-plane. Thus, by summing over all contributions with the same $G_{x,y}$ we get the contributions in the transverse momentum plane. With the transverse momentum values and associated contribution a weighted sum of possible emissions can be computed during the photoemission response calculation. It is of course unnecessary to use the entire grid of the PW basis set. The transverse momentum and likewise transverse energy values for points at the grid edges are comparable to the cut-off energies used in PW calculations. Exemplary values are given in the next Chapter with the applications of this photoemission model and are usually hundreds of eV. By limiting the maximal transverse momentum to within a range of expected values, the size of the file containing the grid can be limited. The OptaDOS photoemission module is intended for photon energies ranging from visible light wavelengths to the ultraviolet (UV).

A common light source in the UV is a He gas discharge lamp, where the HeII's line has a maximum energy of $\sim 51\,\mathrm{eV}$. Based on this 55 eV was chosen as the maximum transverse energy for the grid points. Converting this energy value into a momentum vector using the general energy momentum relation of a plane wave, one gets 3.799 $^1/\text{Å}$ or 2.011 $^1/_{r_{Bohr}}$ as the maximum value. The transverse momentum and contributions at each of the grid points are calculated for all bands at all $\mathbf{k}$ points in the calculation. Examples of such grids are shown in Figure 4.8 for a folded and non-folded band of a Cu(100) 2x2 SC surface. A further visual explanation for a set of G-grid points, how they are summed up in the z-direction and then choosing the subset within 55 eV of transverse momentum is shown in Figure 4.9.

Having described the approach to recover the correct transverse momentum there are a few things to note. Looking at the example curves in Figure 5.7 it becomes clear that the calculated response curve does change. Comparing the two curves using the direct $\mathbf{k}$ with the Gkgrid approach the QE curve is lower for the Gkgrid approach, while the MTE curves are generally comparable. This difference in the QE curve can be explained by looking at the grid point contributions in the Gkgrid approach. For the direct $\mathbf{k}$ approach only one transverse momentum value based on $\mathbf{k}_{x,y}$ is used for the emission calculation. This can also be seen as a single contribution with the weight = 1. In the Gkgrid approach, however, a set of contributions at different transverse momenta of $\mathbf{G}+\mathbf{k}$, is used as the basis for possible emissions. It is not guaranteed, that the sum of all the contributions in the grid are summing up to 1. This has the effect seen in the QE curve in Figure 5.7, where the Gkgrid approach has consistently lower QE values compared to the direct $\mathbf{k}$ approach. Comparing the PC's and SC's QE and MTE curves with the Gkgrid approach, it is clear, that very nearly the same response is calculated for both systems, as one would expect.

This result shows clearly how the Gkgrid approach is essential to calculate comparable response curves between PC systems and more complex SC systems. With this the changes in the spectrum can be attributed to the differences in the electronic structure of a system rather than the model's cell size.

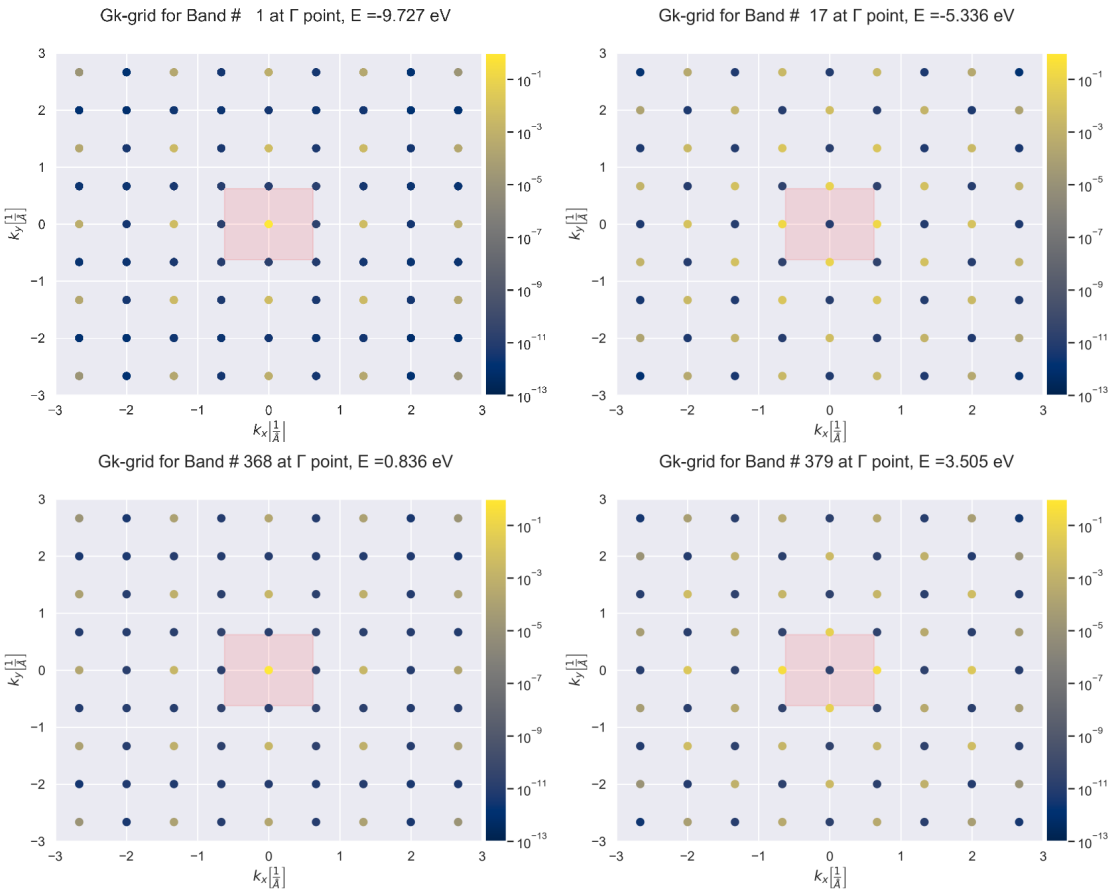


Figure 4.8: Visualisation of the Gkgrid contributions for each point in Cartesian coordinates for the bands in Table 4.2. The red box shows the reciprocal cell size for the PC. The pattern of higher and lower contributions aligns very well with the *folded* and *non-folded* band classification in Table 4.2. Since it is a 2×2 SC, the folded states originated from the edge of the PC BZ, which means, that the high contribution points now correspond to $\mathbf{G} = (N, N, N)^T \in [1, 3, 5, \ldots]$ in fractional coordinates. A non-folded band has the highest contribution for $\mathbf{G} = \vec{0}$ and the other higher contributions are located at $\mathbf{G} = (N, N, N)^T \in [2, 4, 6, \ldots]$ in fractional coordinates.

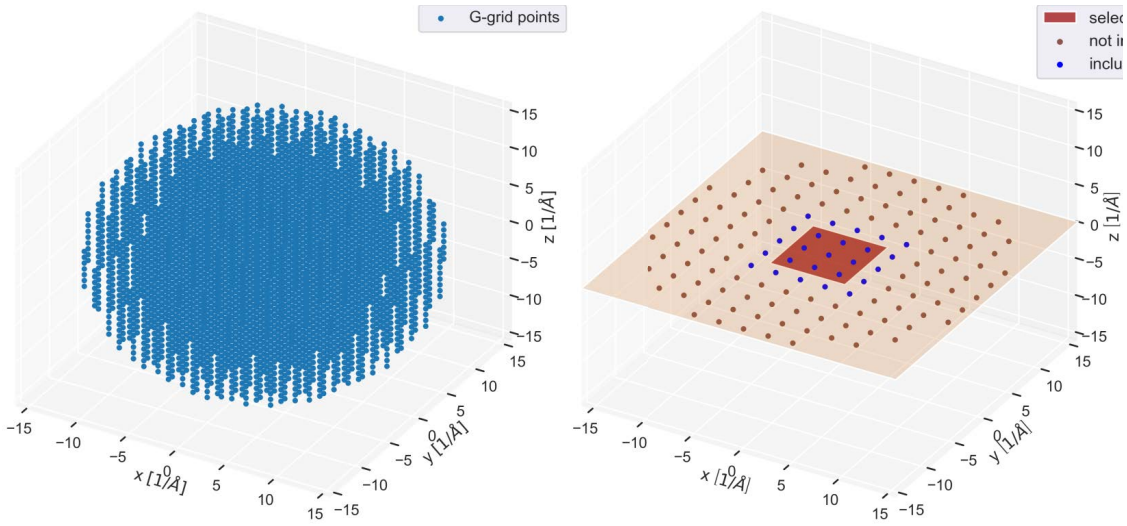


Figure 4.9: left: The entire set of **G**+**k**-grid points with $\vec{k} = \vec{0}$ for a Cu(100) cell with some points in the Z direction not shown for visual clarity. See Section 5.3.2 for exact cell size of Cu(100) surface. right: Set of **G**+**k**-grid points after summing all contributions with the same $\mathbf{G}_{x,y}$ coordinates. The selection zone has the lateral size of 3.799 $^1/_{\text{Å}}$, corresponding to 55 eV of transverse energy. The extra points outside the selection zone are chosen to account for any possible offset due to the **k** point vector when creating the **G**+**k**-grid. The not included points have such a high transverse momentum, that they would not be able to contribute unless one calculates PE with photon energies beyond the UPS range.

5 Photoemission code and modelling

5.1 Discussion of Code Development

The main goal during this work was to continue the development of the code implementing the photoemission model described in the previous section and add further capabilities. This meant analysing the code that had been developed during the two previous PhD projects and find the causes for some unexpected behaviours, as well as resolving limitations present in the previous code base. Since the photoemission model is implemented as a module of the OptaDOS code package [81] the assumptions made within the other modules needed to be considered and behaviour adjusted where necessary. In the following it will be discussed how the main issues presented themselves and how they were ultimately addressed.

Issue: Floating point exceptions and undefined behaviour

After execution of the code the programme would report errors for illegal mathematical operations, also called *floating point exceptions*, and showed so called *undefined behaviour*. This behaviour included program encountering a problem and stop or the printing unexpected values for calculated quantities. These included *not a number* (NaN), quantities = 0 if they should be $\neq 0$, or quantities having a random value. These behaviours stemmed from improperly initialised variables and mathematical functions being not properly guarded against improper inputs, such as negative values in ln or a division by 0.

Issue: Cell volume dependency of photoemission values

The calculated optical properties for slab layers and the resulting photoemission response curves showed a cell volume dependence. This would manifest as a change in the calculated photoemission when changing the vacuum gap included between a slab model. This dependence was traced back to two points within the OptaDOS code. As discussed in Section 4.2 all optical properties are calculated for a volume of space. The OptaDOS code was originally designed for bulk material cells so the entire cell volume was assumed to be part of the material. By using the volume of each layer to calculate the optical properties this dependence can be resolved.

Secondly, the `adaptive` smearing implementation discussed in Section 2.8 is also dependent on the cell size. This smearing scheme is used both to calculate the optical properties and the δ function for the 3-step model. The implementation in OptaDOS uses the Cartesian distance between $\mathbf{k}$ points in the sampling grid, which is defined in fractional coordinates. This dependence is working properly in the x, y directions, but not in the z direction containing an arbitrary amount of vacuum. Using the layer z size, rather than cell's z height resolves this dependence.

Issue: Missing input parameters and intermediate value output

The code was not printing all necessary input values for the optical property calculations and none of the photoemission parameters. This made recreating the input file from a previous photoemission calculation impossible. Further no printing of intermediate values for debugging purposes was implemented, making the search for improperly initialised variables and undefined mathematical operations difficult. Printing of all necessary input parameters and some intermediate values was implemented and debug printing options for calculated quantities were added.

Issue: The 1-step free electron state construction
In the original implementation of the 1-step model the final state was improperly expressed in the plane wave basis set. The p_z, i.e. the normal component $p_\perp$, was assumed to always = 0. This means, that the final state for the 1-step emission had no momentum away from the surface. This is of course unphysical, because with this no electrons could be measured. This also makes the free electron state energy independent of photon energy, which does not ensure energy conservation. The optical matrix elements (OMEs) were therefore calculated to a incorrectly defined state. This

was rectified by changing the construction to include the photon energy dependent p_z component.

Optimisation: Fowler-Nordheim transmission probability

The transmission probability across the Fowler-Nordheim barrier, as discussed in Section 4.7, was originally calculated using numeric integration. This resulted in very slow calculations for low field strengths. The described transmission probability approximation was implemented making the calculation of transmission probabilities much faster.

Optimisation: Loop optimisations

The code module contains a number of highly nested loops, which were not optimised for speed of execution. Code analysis tools, i.e. valgrind [150] and Intel VTune, were used to find areas of concern for performance and memory leak issues. Slow lines were replaced where possible, like an `if` statement being called millions of times, and the indexing order of arrays were changed to allow for contiguous memory access.

Optimisation: Code Parallelisation

The OptaDOS code does not officially support parallelised calculations for all functionality, but the parts relevant to photoemission calculations were tested for correct execution and the parallelisation of the photoemission module was finalised. The parallelisation uses message passing interface (MPI) parallelisation. The calculation can be fully parallelised across the set of **k** points. The photoemission calculation was be performed on a Cu(100) surface slab with a $512 \times 512 \times 1$ MP grid containing $> 33,000$ **k** points using 256 CPU cores for testing purposes. This grid size is much larger than necessary, but a good test for the code's limits.

New Feature: Photon energy ranges

Originally the photoemission code was implemented such that calculations were only possible for a single photon energy, while always calculating optical properties for a range of photon energies. The implementation was changed to allow for the calculation of photoemission characteristics for a range of photon energies. This greatly reduces the necessary computational time of calculating a response curve, as the set of necessary optical properties is only calculated once.

New Feature: Supercell photoemission

As discussed in Section 4.11 and in the thesis by Camino [11], the photoemission response of a supercell (SC) model compared to the primitive cell (PC) equivalent, was a big limitation of the code. The described approach was implemented to allow for the calculation of comparable response curves between PCs and SCs. This way interfaces and other surface features of interest can be recreated in surface slab models and their impact on the PE response studied.

New Feature: ARPES maps

The code is now able to print a series of emission maps that can be compared to emission data from ARPES experiments. Originally only a binding energy curve was implemented, which similar to an ARPES energy distribution curve (EDC). These maps allow the user to perform detailed analysis of the emission patterns and extend the range of quantities that can be compared to experimental results.

All these changes result in a very different codebase at the end of this work compared to earlier versions of the code. The code module is under review by the OptaDOS developer group, giving the research community access to this open source PE tool hopefully very soon. The necessary changes to the CASTEP code are also due to be included in the CASTEP releases in the near

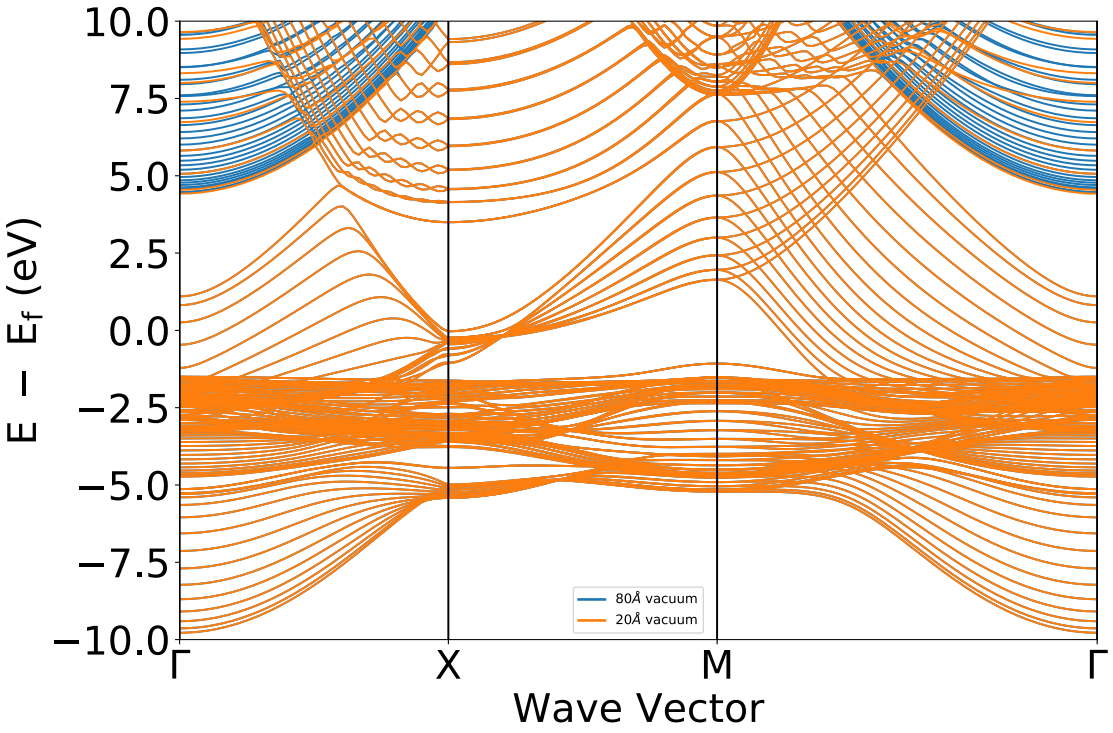


Figure 5.1: Bandstructure plot for two Cu(100) surface models with 16 layers of Cu atoms and varying amounts of vacuum in between periodic images. The equal dispersion for the Cu based is evident and the notable change of the number of parabolic bands around Γ is notable.

future, giving access to the full workflow for other researchers and users.

5.2 The Issue of Convergence

When constructing a surface model one important aspect is how the surface model changes when increasing or decreasing the number of layers in slab. Another is the amount of vacuum included in the cell. If not enough vacuum is present in between the slabs, unwanted interaction between them can occur and modify the vacuum potential and electronic structure. The more layers are included in the model, the better the representation of a surface with underlying bulk material can be achieved. This allows important quantities to converge, such as the surface energy and bulk like DOS in the innermost layers. But including more layers also increases the computational demands, limiting the maximal size that can be modelled. Additionally, changing both of these variable quantities also has an impact on the calculated photoemission spectrum.

The amount of vacuum has impact especially on the 3-step model PE spectrum. This can easily be rationalised by plotting the surface bandstructures for two Cu(100) models with very different amounts of vacuum in between the slabs. The surface slab structures contain both 16 layers of Cu atoms and the electronic structure is calculated using the same parameters as in the model described in Section 5.3.2. The two resulting bandstructures are shown superimposed in Figure 5.1. It is clear, that the Cu based bands have the same energies and dispersion for both systems, but the change in the number of parabolic bands centred on the Γ point is notable.

In the 3-step model these states are the final states for the excitations that also produce emission, since the transverse momentum is limiting the possible emissions. Since the Γ point has no transverse momentum associated with it, it will be where the threshold emissions originate. Therefore one can expect the calculated PE response to be impacted by the amount of vacuum present in

the cell, making it a factor the user should be aware of. This issue, however, is not present for the 1-step model, since the excitation is into a constructed final state of arbitrary energy, rather than a Bloch state.

The number of layers in the surface slab model has an impact on the calculated PE response, as well. Comparing the PE spectra for two Cu(100) surface models with 16 and 64 layers, as discussed in Section 5.3.2 and plotted in Figure 5.6, shows that the MTE spectrum is smoothed out, but also the initial QE spectrum appears to be suppressed. As of writing of this thesis, it is not entirely clear, which parts of the QE calculation have this suppression effect. The smoothing of the MTE spectrum is as expected, since the oscillations in the MTE spectrum are associated with discretised excitations. With more possible excitations the discrete values approach the continuum limit. This is another aspect to consider for the user. By increasing the number of layers the quality of the surface model is increased and the MTE spectrum shows a smoother response, but the QE spectrum is also modified in the process.

These observations taken together make it complex to define a convergence criterion for the PE response, since simply increasing the number of layers does not converge to a single response spectrum. This might make it more difficult to quantitatively compare the results. The comparison between calculated spectra, however, will not be impacted if the surface models are kept consistent.

5.3 Metallic Surfaces

For all simulations the CASTEP code of the academic version 23.1 is used. To describe the atoms the ultrasoft pseudopotentials generated on the fly (OTFG) by CASTEP [76] are used, using the PBEsol GGA functional [63], as it is a widely used functional with an improved description of solids, and the default OTFG USP version for CASTEP 23.1, named "C19", is used.

The experimental data, which is used to compare to the calculated MTE values for the Cu surfaces has been measured using the transverse energy spread spectrometer (TESS) instrument located in the ASTeC group within the STFC laboratory at Daresbury [151, 152]. It is made of a tuneable light source to illuminate the photocathode of interest and the emitted electrons spread out according to their mean transverse momentum. The electrons are extracted using a low energy electric field, are amplified using a multichannel plate and create a picture on a phosphor screen. TESS is specifically designed to isolate the drifting electrons from outside influences, such as stray magnetic fields [151, 152].

5.3.1 Cu Bulk

A Cu bulk system has been modelled to define the geometry that the surface slabs are cut from. The specific low index surface slabs are discussed in the following sections. The Cu bulk structure before relaxation is constructed as a primitive face centred cubic (fcc) cell ($Fm\bar{3}m$) [86] with a lattice parameter $a'_{prim} = 2.53\,\text{Å}$ as taken from the Materials Project [153] with a single atom centred on the origin. This primitive lattice parameter equates to a conventional lattice parameter of $a'_{conv} = 3.58\,\text{Å}$.

The plane wave basis cut-off, representing the maximum energy of PWs used to describe the wavefunctions (see Section 2.4.1 for reference), is set to 566 eV, giving a total energy convergence of $5 \times 10^{-4}\,\text{eV}$. The standard FFT grid factor (`grid_scale`) as a multiple of the cut-off sphere radius is set to 2.0, and the fine FFT grid factor (`fine_grid_scale`) as a multiple of standard grid G_{max} is set to 3.0. The PBEsol GGA functional [63] is used to approximate the xc energy. The convergence criterion for the electronic energy is set to $1.0 \times 10^{-8}\,\text{eV atom}^{-1}$. The density is mixed using the Pulay mixing scheme as implemented in CASTEP. The BZ is sampled using a Monkhorst-Pack (MP) grid with the dimensions $12 \times 12 \times 12$ and offset by half a step between the grid points, so the Γ point is included in the set of $\mathbf{k}$ points. The number of electronic states is increased by 25 % to 12 and the system is treated as spin-polarised. A Gaussian smearing of

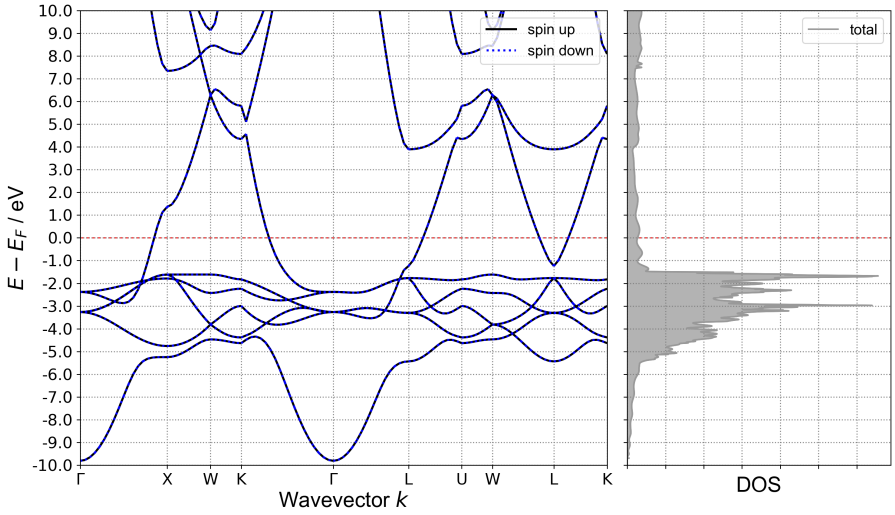


Figure 5.2: Calculated band structure and DOS for the bulk fcc Cu structure.

$k_B \cdot 300\,\mathrm{K}$ is applied to the electronic states, where k_B is the Boltzmann constant.

The structure and cell is relaxed using the LBFGS [154] optimisation method as implemented in CASTEP until all components of the constrained stress tensor on the cell are $\leq 5 \times 10^{-4}\,\mathrm{GPa}$, constraining the cell angles to 60° and the cell lengths to all be equal. The resulting bulk structure has the lattice parameter $a_{prim} = 2.5175\,\text{Å}$ or $a_{conv} = 3.5602\,\text{Å}$, which is within 1 % of experimental values [155] and identical up to two decimal places with other works using the PBEsol functional [156]. The LBFGS optimiser reported a final bulk modulus $K = 165.64\,\mathrm{GPa}$, which is almost 20 % above experimental values of 142 GPa [157, 158], which is extrapolated to 0 K from measurements down to 4.2 K [157], but within 1 % of reported values for PBEsol DFT of 166 GPa [158]. The calculated band structure and the bulk DOS are shown in Figure 5.2.

The following Cu surface slabs are all created using the `SlabGenerator` functionality implemented in the `pymatgen` software package [159]. This slab generator can generate cells with any surface angle, so the options were chosen to ensure that the surface normal = 90°. Furthermore, all slab geometries have the same number of atoms and the same calculation parameters given to CASTEP so only the different cell geometries will be presented for each.
During the SCF calculation the density is mixed using the Pulay mixing scheme as implemented in CASTEP. The plane wave basis cut-off is selected as 730 eV. The `grid_scale` is set to 2.0, and the `fine_grid_scale` is set to 3.0. The PBEsol GGA functional is used. The convergence criterion for the electronic energy is set to $1.0 \times 10^{-8}\,\mathrm{eV\,atom^{-1}}$. For the geometry relaxation the BZ is sampled using a MP grid with the dimensions $17 \times 17 \times 1$ with no offset. All slabs are geometry optimised until any component of the forces on the atoms is $\leq 5 \times 10^{-3}\,\mathrm{eV\,Å^{-1}}$. The number of states is doubled to 176 for the geometry relaxation. For the calculation of the spectral properties, which does not perform self-consistent updates on the density, the MP grid density is increased to $51 \times 51 \times 1$ with no offset and the number of states is increased by CASTEP by default, giving in total 243 states per **k** point.

The surface energy is calculated using

$$E_{surface} = \frac{1}{2} \cdot (E_{slab} - n_{units} \cdot E_{bulk}) \tag{5.1}$$

where E_{slab} is the total energy of the slab, n_{units} is the number of unit cells contained in the slab and E_{bulk} is the total energy for the material's bulk phase. The photoemission response for the Cu surface models is calculated using the `adaptive` broadening scheme with a smearing ratio of

0.4 [81, 120], the bin width for the JDOS $bin_{jdos} = 0.05\,\text{eV}$, the scattering is calculated using an IMFP constant $\lambda_{\text{Cu}} = 5.3\,\text{Å}$, and the temperature smearing is set to 300 K.

5.3.2 Cu(100) Surface

The Cu(100) surface slab is created with 16 layers from the relaxed Cu bulk structure. Periodic boundary conditions (PBCs) are applied in all Cartesian directions. The cell length in the c direction and the atoms' z coordinates are adjusted, so that 60 Å of vacuum are present between the repeated surfaces before geometry relaxation, resulting in a tetragonal cell with $a = 2.50\,\text{Å}$, and $c = 86.95\,\text{Å}$.

The surface slab geometry is relaxed until the force components on all atoms are $\leq 5\times10^{-3}\,\text{eV Å}^{-1}$. The spectral properties are calculated, the WF is determined as $W = 4.61\,\text{eV}$, which is in good agreement with experimental values of 4.73(10) eV [160] or 4.59 eV [161], and another PBEsol based DFT value of 4.43 eV [162]. The surface terminations are determined using the density cut-off to be 58.62 Å and 27.42 Å for the upper and lower surface, respectively. The surface energy, calculated using Equation (5.1), is $E_{surface}(\text{Cu(100)}) = 1.77\,\text{J m}^{-2}$, which is very close to other PBEsol DFT values of $1.76\,\text{J m}^{-2}$, and the experimental value for a polycrystalline surface is given as $1.79(19)\,\text{J m}^{-2}$ [162].

Calculating the photoemission response for the Cu(100) surface using the 3-step model gives the curves shown in Figure 5.3. The response curves are compared to the extended DS model [95] and experimental data for a Cu(100) single crystal measured with the TESS instrument [151, 152]. The spectra show very good agreement for the comparable range, but the calculated response shows many oscillations in both spectra. This can be linked to the band structure having discrete regions rather than a continuous spectrum and using individual electronic states to calculate the photoemission response. General deviations of the curve could also be caused by not considering scattered electrons in the current implementation of the model. By calculating a *kinetic energy vs transverse momentum map* and choosing the emission angles carefully, the emissions along paths starting from Γ can be calculated and visualised. For the Cu(100) system these are $X \leftarrow \Gamma$ (90°) and $\Gamma \rightarrow M$ (45°) directions. Two such plots are shown in Figure 5.5 for a photon energy just above the WF (4.65 eV) and one at 5.3 eV.

To explore how changing the number of layers affects the calculated spectra, a Cu(100) surface model with 64 layers is prepared in the same manner as the 16 layer model. The photoemission spectra are calculated and Figure 5.6 shows the comparison for the two different systems. The smoother response spectrum for the 64 layer surface model is evident, which is as expected due to the larger number of discrete states considered. The QE spectrum, however, appears to show a smaller QE for the 64 layers, which is the opposite of the expected behaviour. The origin for this unexpected behaviour is not clear at this moment and will have to be investigated in the future.
The approach to calculate the PE of supercells using the `Gkgrid` method described in Section 4.11 needs to be tested for suitability and the differences to the `crystal` approach explored. The `Gkgrid` method expands each of the set of **k** points into a grid with the spacing of the reciprocal cell's lateral size. The plane wave basis contributions to the electronic states for this grid are then used to calculate the transverse momentum for a set of possible electron emissions. These grid contributions are very similar for both primitive cells and supercells of a given material. This allows the calculation of comparable PE response curves for different cell sizes, so that hetero-interfaces can be compared to bare surfaces, defective surfaces can be compared to pristine surfaces, and other applications where supercells are necessary.
For this test one can compare the calculated photoemission response for the 1×1 cell to a 2×2 repeated supercell of that exact structure. The geometry optimisation is performed using the same CASTEP parameters except for the MP grid being about halved to $9 \times 9 \times 1$ to keep the **k** point density similar between the two systems. The spectral parameters are calculated using a modified MP grid of $25 \times 25 \times 1$. The photoemission response is calculated for both the *crystal* and *Gkgrid* option for the momentum scheme and the four different curves are shown in Figure 5.7.

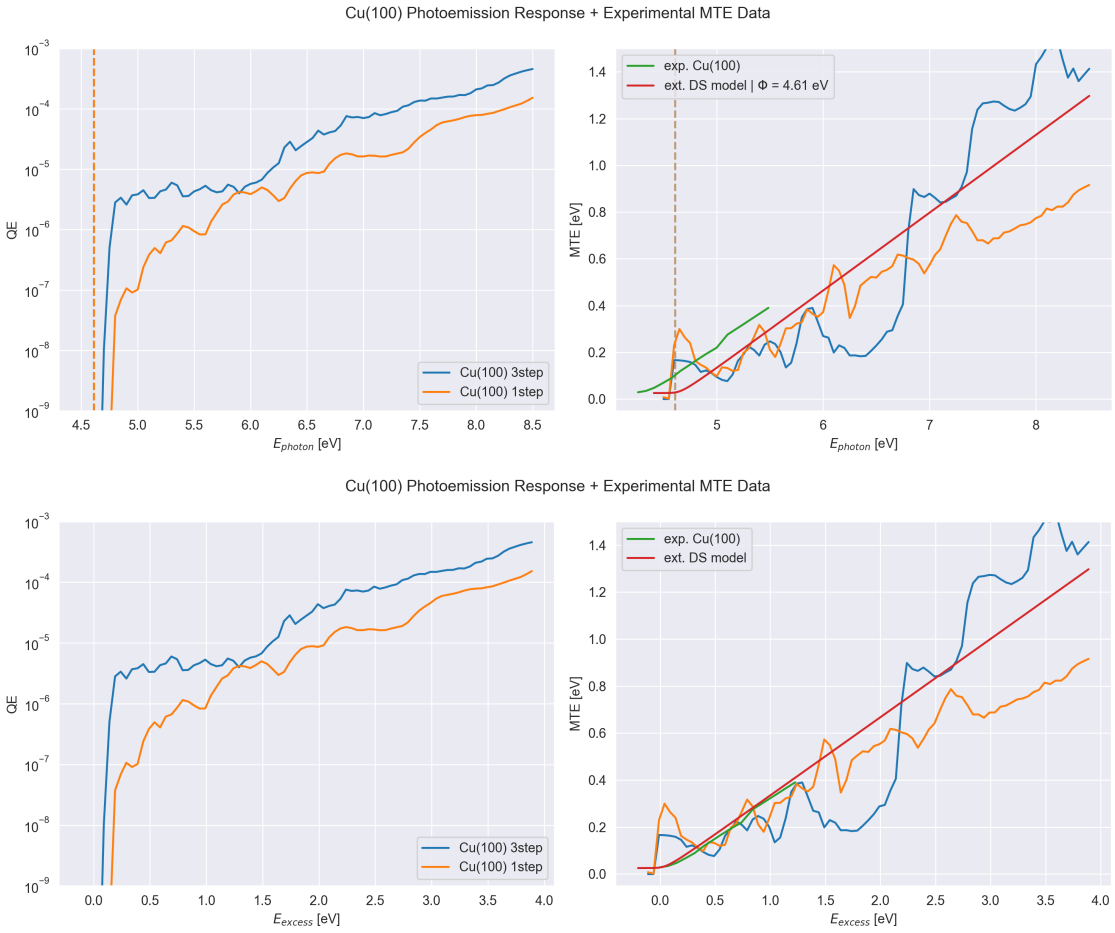


Figure 5.3: Photoemission response calculated for a Cu(100) 16 layer slab using the 3-step and 1-step models. The energy axis is shown as both photon energy (top) and excess energy above the WF (bottom). The comparison with the extended DS model [95], as well as experimental data measured using the TESS instrument [151, 152] shows very good agreement in the comparable range. The varying oscillations in both curves can be attributed to discrete states rather than a continuum contributing to the calculated photoemission response.

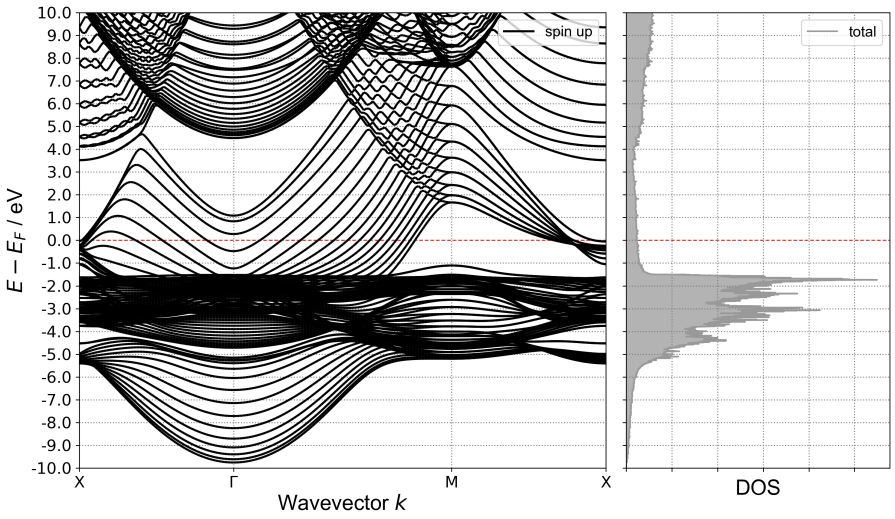


Figure 5.4: Calculated band structure for the Cu(100) 16 layer slab and the corresponding DOS; the red dashed lines indicate the Fermi energy.

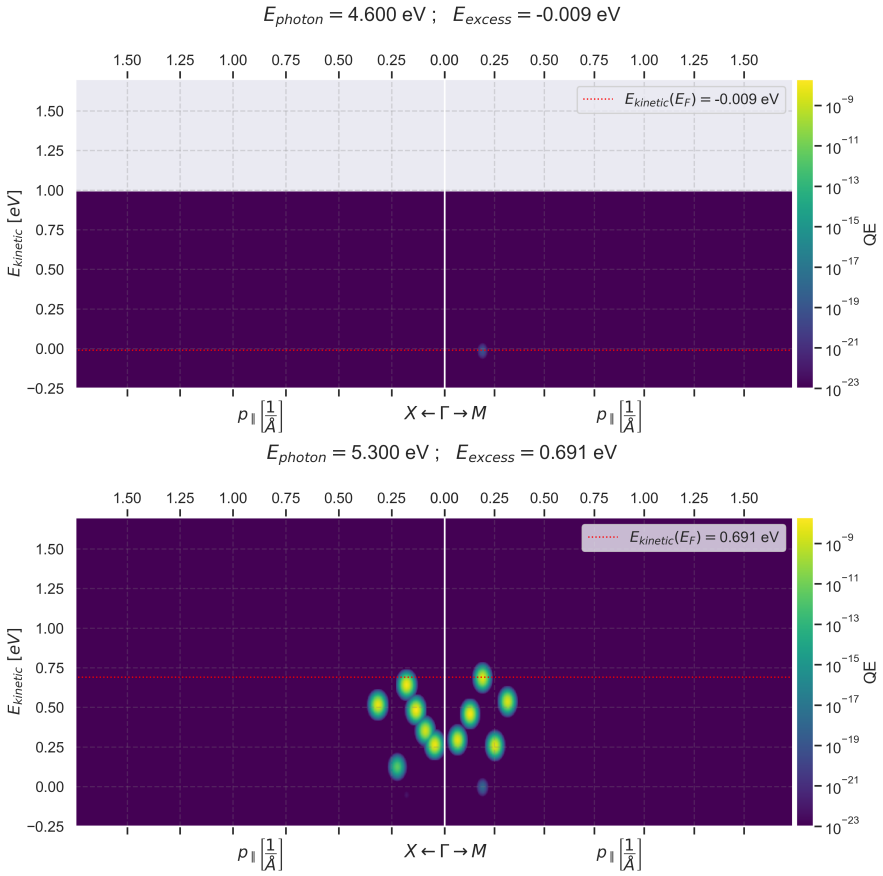


Figure 5.5: Broadened 3-step emissions for 4.60 eV and 5.30 eV showing the kinetic energy vs transverse momentum distribution. The first emission contributions near threshold originate from a state crossing the Fermi energy away from the origin, resulting in a high MTE value at threshold. At a higher energy of 5.3 eV, further states are able to contribute to the emission, lowering the calculated MTE value.

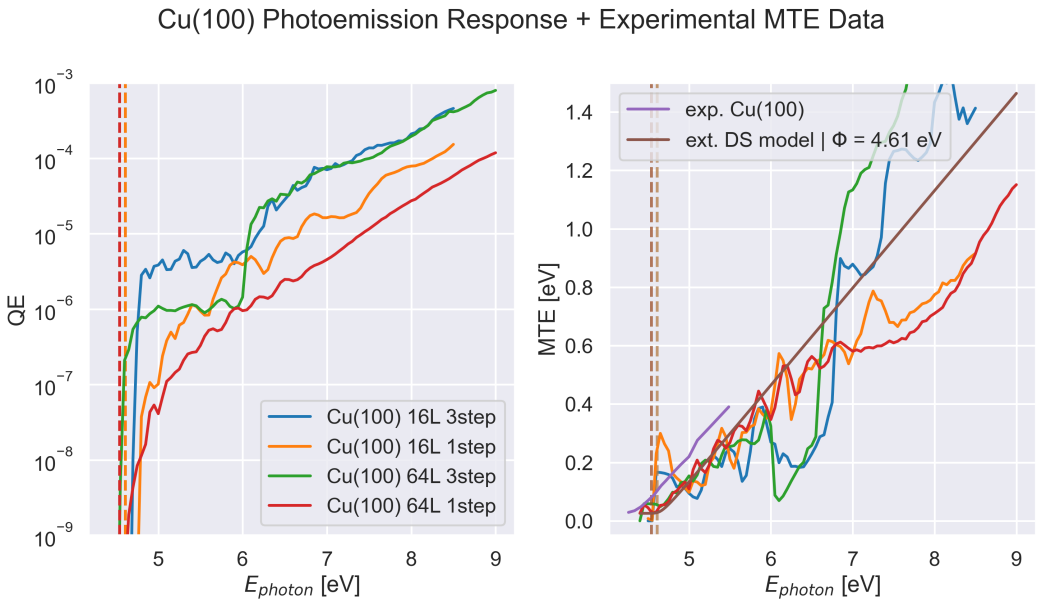


Figure 5.6: Calculated PE spectra for a Cu(100) surface with 16 and 64 layers. Both spectra show much smaller oscillations for the 64 layer model, but the QE spectrum appears to be suppressed for the 64 layer model.

To further analyse the specific emissions from different states, one can construct a similar plot to Figure 5.5 but at a much higher photon energy of 16 eV. These plots for both the `crystal` and `Gkgrid` options are given in Figure 5.8. The missing chunk of data in both panels of this Figure is due to the symmetry reduction of the MP grid. Since the system has a tetragonal cell, the $\mathbf{k}$ points along the x-axis are symmetry equivalent to the $\mathbf{k}$ along y-axis and so only one set is kept for the calculation. For some of the emission maps implemented the symmetry reduction is reversed using the determined symmetry elements, but this has not yet been implemented for this specific map type. The main differences between `crystal` (top) and `Gkgrid` (bottom) are still evident, though.

First, the overall emission strength is lower in the `Gkgrid` case and some of the flat bands along $\Gamma \to M$ are almost entirely missing. This can be related to the contributions on the Gk grid < 1 or even $\ll 1$. The reason why some bands are suppressed in the Gk grid contributions is not known as of writing of this work and is a good candidate for further work in the future. The missing flat bands near the origin can also help to explain the strong increase in the calculated MTE value at ≈ 6.8 eV. While the `crystal` MTE curve rises to the approximate level of the extended DS model, the `Gkgrid` shows a large overshoot of the linear curve. One likely explanation for this is the apparent lack of calculated emissions near the origin as shown in Figure 5.8. The suppression of generally flat bands near the Γ point, means that the overall *mean* of the transverse momentum for the electron emissions is increased.

Secondly the emissions for the `crystal` approach stop at the first BZ edge in the $\Gamma \to X$ direction, while the `Gkgrid` shows further bands in the next BZ over. The BZ edge edge is located at $1.258\,\text{Å}^{-1}$, given the slab's cell size mentioned earlier. These emissions outside the first BZ are expected, since the contributions are calculated as $\mathbf{k} + n\mathbf{G}_{x,y}$ with $n \in \mathbb{N}$, so the **Gk** grid extends far beyond the first BZ. This is not seen in the $\Gamma \to M$ direction at this photon energy, since the BZ corner is at $\sqrt{2} \times 1.258\,\text{Å}^{-1} = 1.779\,\text{Å}^{-1}$, which is a slightly higher transverse momentum than the maximum transverse momentum of electrons, that can escape.

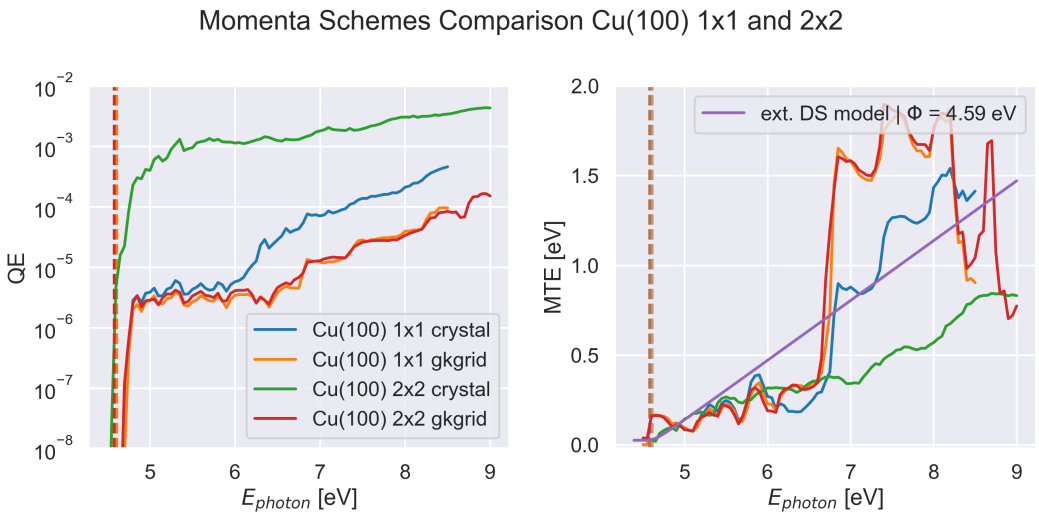


Figure 5.7: Comparison of calculated PE curves for a Cu(100) 1x1 slab and a 2x2 SC of this exact same structure using both available momenta schemes. Comparing the `crystal` curves, it is evident that this approach fails to give comparable results. The `Gkgrid` approach, on the other hand, gives nearly identical QE and MTE values, although the values are changed compared to the `crystal` scheme.

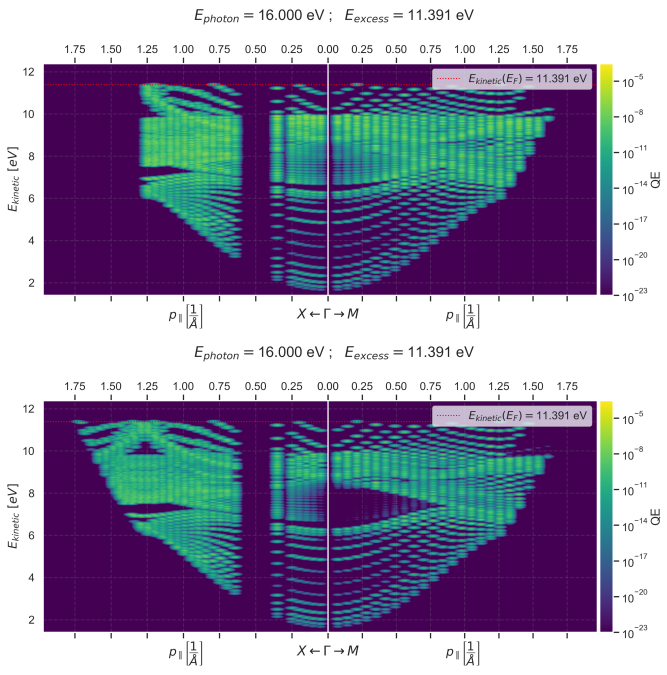


Figure 5.8: Broadened 3-step emissions for 16 eV showing the kinetic energy vs transverse momentum distribution for the `crystal` (top) and `Gkgrid` (bottom) momentum options. The section of missing data in the left panel of both is due to the symmetry reduction of the MP grid. Reconstruction for the full MP grid has not yet been implemented for the kinetic energy vs transverse momentum map.

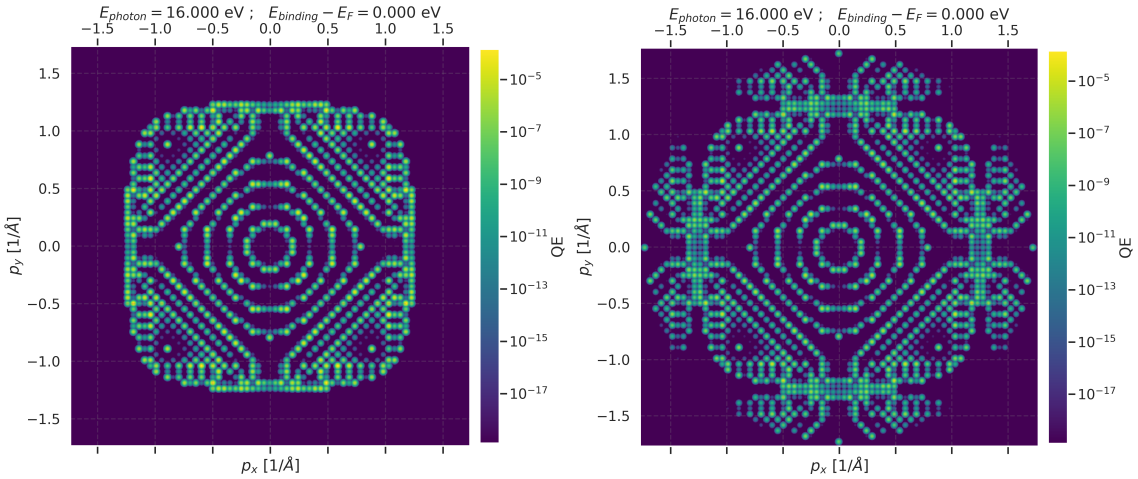


Figure 5.9: Constant binding energy maps for Cu(100) surface with a binding energy broadening of 0.026 eV. left: map using the *crystal* momentum scheme, showing the circular features for the parabolic bands near the origin and the flat bands near the edge of the BZ. The outer edges align with the edges of the BZ. The MP grid only extends to the outer edges of the BZ, so no calculated emission outside of these is expected. right: map using the *Gkgrid* momentum scheme, but the overall emission intensity is slightly reduced. The same features as in the *crystal* scheme case are present within the BZ boundaries. Furthermore, the emissions extend outside the first BZ, since the MP grid is extended for the *Gkgrid* momentum scheme, so this behaviour is as expected.

In addition to kinetic energy maps, the code also has the option to calculate a map across the reciprocal space for a given binding energy $E_{binding} = \varepsilon_i(\mathbf{k}) - E_F$ with ε_i being the initial electron's energy and E_F being the Fermi energy. Two such maps are shown in Figure 5.9 for the bands located at and near the Fermi energy and for the two momentum schemes implemented. Both maps show very similar features of parabolic bands (circular features) around the origin, as well as flat bands near the BZ edges. The *Gkgrid* scheme further shows emissions outside the BZ, since the MP grid of $\mathbf{k}$ points is extended outside the BZ in the *Gkgrid*.

5.3.3 Cu(110) Surface

The Cu(110) surface slab is created with 16 layers from the relaxed Cu bulk structure. PBCs are applied in all Cartesian directions. The cell length in the c direction and the atoms' z coordinates are adjusted, so that 60 Å of vacuum are present between the repeated surfaces before geometry relaxation, resulting in a orthorhombic cell with $a = 2.52$ Å, $b = 3.56$ Å, and $c = 78.75$ Å.

The surface slab geometry is relaxed until the force components on all atoms are $\leq 5 \times 10^{-3}\,\mathrm{eV\,Å^{-1}}$. The WF is determined as $W = 4.45\,\mathrm{eV}$, which is in good agreement with experimental values of $4.56(10)\,\mathrm{eV}$ [160] and $4.48\,\mathrm{eV}$ [161], and PBEsol DFT based value of $4.48\,\mathrm{eV}$ [162]. The surface terminations are determined using the density threshold method to be 50.40 Å and 28.44 Å for the upper and lower surface respectively. The surface energy, calculated using Equation (5.1), is $E_{surface}(\mathrm{Cu(110)}) = 1.88\,\mathrm{J\,m^{-2}}$, which is very close to a PBEsol DFT calculated value of $1.88\,\mathrm{J\,m^{-2}}$ [162] and in reasonable agreement with the experimental value for a polycrystalline surface of $1.79(19)\,\mathrm{J\,m^{-2}}$ [162].

Calculating the photoemission response for the Cu(110) surface using the 3-step and 1-step model gives the curves shown in Figure 5.10. The response curves are compared to the extended DS model [95] and experimental data for a Cu(110) single crystal measured with the TESS instrument [151, 152].

The 3-step model shows better reproduction of the experimental data with its gradual increase, compared to the 1-step model, which has a strong MTE response near the PE threshold. This can be related back to the emissions shown for the 3-step and 1-step model in Figure 5.12 and Figure 5.13, respectively. Comparing the Cu(110) band structure shown in Figure 5.11 to the emission maps, the 1-step model calculates a weak emission from the flat state located $\approx 0.5\,\mathrm{eV}$ above the Fermi energy at Γ. This can explains the high MTE value calculated for low excess energies. In the case of the 3-step model, this band is not emitting. Instead a flat band located $\approx 0.3\,\mathrm{eV}$ below the Fermi energy is the first band to emit. This explains the lack of MTE at very low excess energies. The emission maps at 5.1 eV are very comparable for both models, which aligns with the calculated MTE values being nearly identical.

Calculating a constant binding energy map, which is shown in Figure 5.14, clearly shows the orthorhombic nature of the surface cell. The flat bands crossing the Fermi energy on the path towards the Y point are shown in the top middle and the parabola like bands near the Y point. The map for the *Gkgrid* momentum scheme shows the same features with a systematically lower emission intensity, but extends the calculated emissions beyond the BZ boundaries.

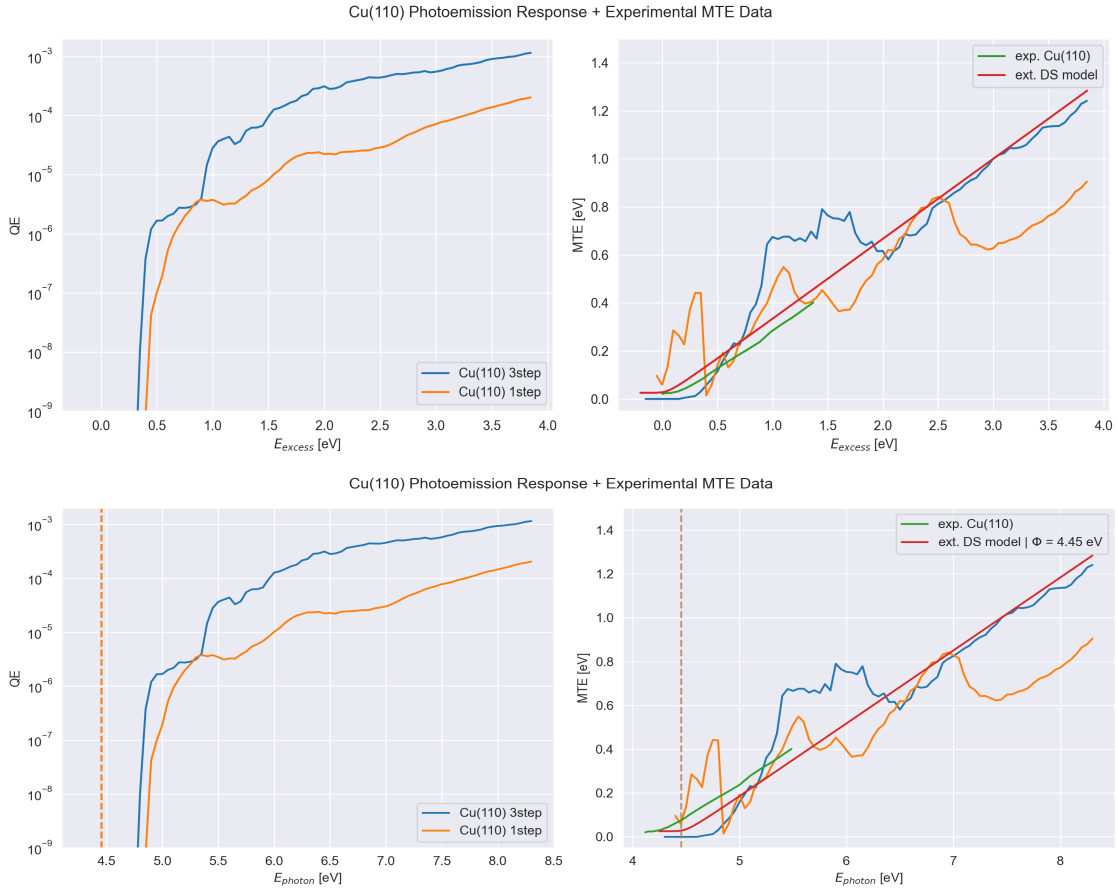


Figure 5.10: Photoemission Response calculated for a Cu(110) 16 layer slab using the 3-step and 1-step models. The energy axis is shown as both photon energy (top) and excess energy above the WF (bottom). The comparison with the extended DS model [95], as well as experimental data measured using the TESS instrument [151, 152]. The strong calculated 1-step MTE response can be attributed to flat states contributing early, see Figure 5.13 for map showing the 1-Step model emissions near threshold. The 3-step model shows a more comparable response until it starts deviating above $\approx 5.3\,\text{eV}$, but has very good agreement above $\approx 7\,\text{eV}$.

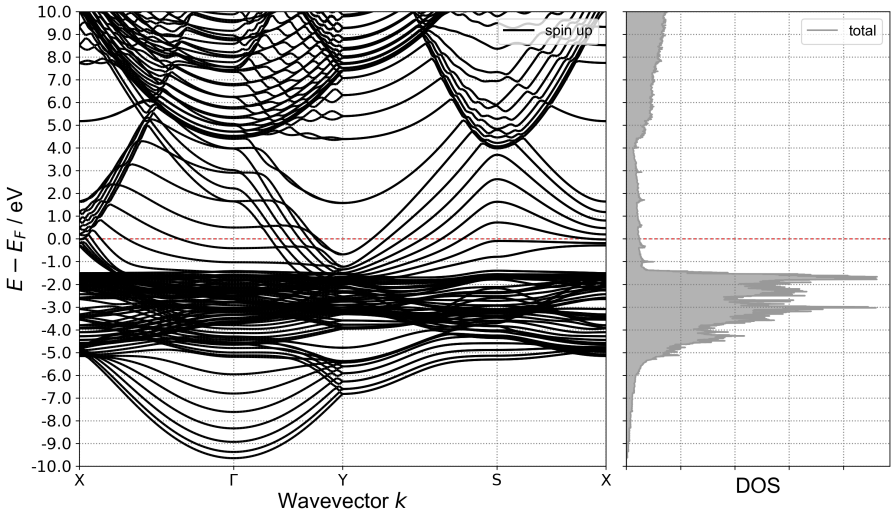


Figure 5.11: Calculated band structure and DOS for the Cu(110) 16 layer slab, the red dashed line indicates the Fermi energy.

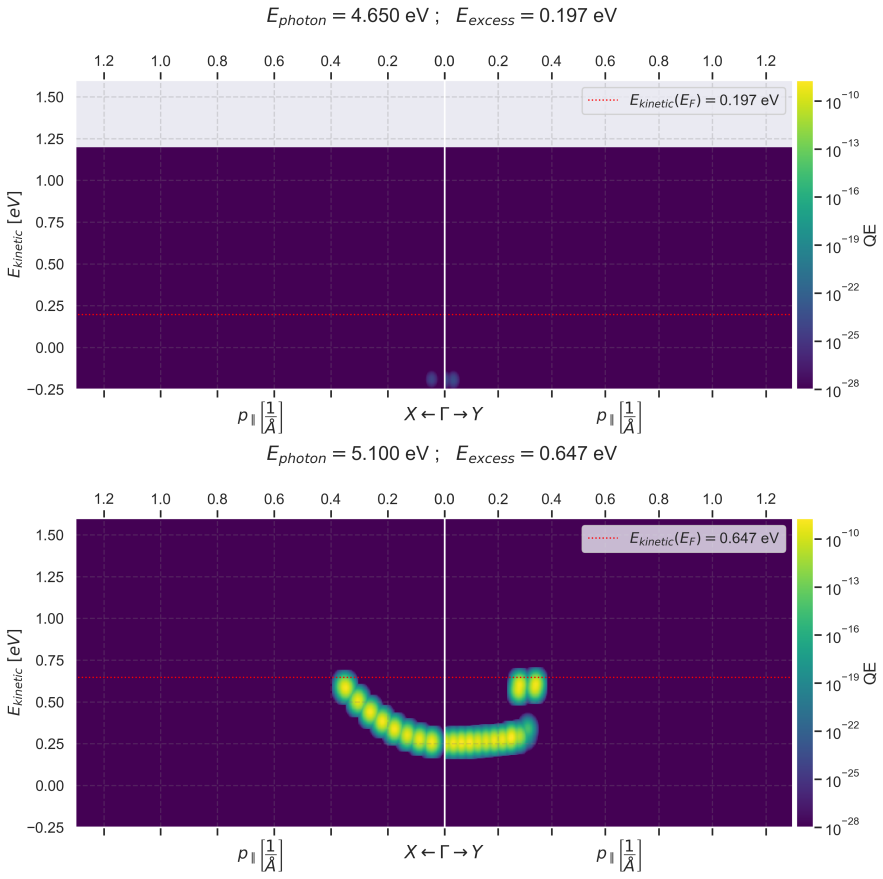


Figure 5.12: Broadened 3-step emissions for Cu(110) at 4.65 eV and 5.10 eV showing the kinetic energy vs transverse momentum distribution. The first emission contributions originate from a flat state lying below the Fermi energy, which explains the onset of emission away from the threshold energy. At higher energies, more of the same state can contribute and a second state near the Fermi energy can contribute.

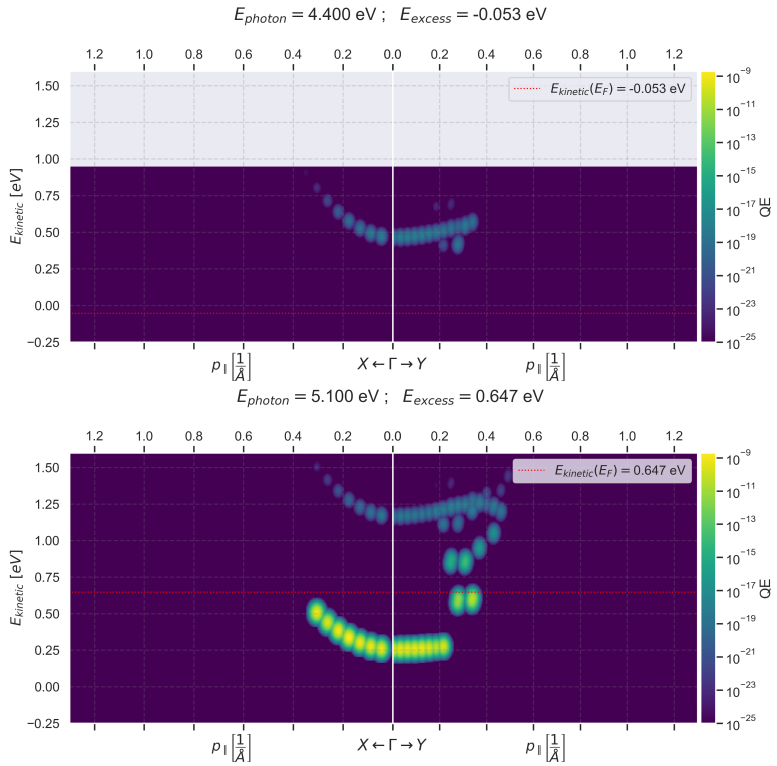


Figure 5.13: Broadened 1-step emissions for Cu(110) at 4.40 eV and 5.10 eV showing the kinetic energy vs transverse momentum distribution. The first emission contributions originate from a flat state lying above the Fermi energy, which explains the onset of emission below the threshold energy. Further the high calculated MTE value at threshold is associated with emissions from states away from the Γ point.

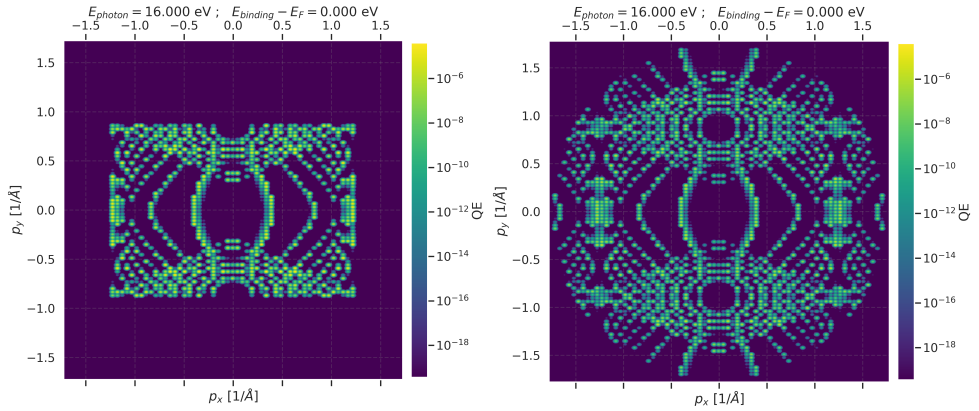


Figure 5.14: Constant binding energy maps for Cu(110) surface with a binding energy broadening of 0.026 eV. left: map using the *crystal* momentum scheme, The MP grid only extends to the outer edges of the BZ, so no calculated emission outside of these is expected. The orthorhombic shape of the BZ is evident. right: map using the *Gkgrid* momentum scheme. The same features as in the *crystal* scheme case are present within the BZ boundaries, but the overall emission intensity is slightly reduced. Furthermore, the emissions extend outside the first BZ, since the MP grid is extended for the *Gkgrid* momentum scheme, so this behaviour is as expected.

5.3.4 Cu(111) Surface

The Cu(111) surface slab is created with 16 layers from the relaxed Cu bulk structure and PBCs are applied for all Cartesian directions. The cell length in the c direction and the atoms' z coordinates are adjusted, so that 60 Å of vacuum are present between the repeated surfaces before geometry relaxation, resulting in a trigonal cell with $a = 2.52$ Å, and $c = 90.84$ Å.

The surface slab geometry is relaxed until the force components on all atoms are $\leq 5 \times 10^{-3}$ eV Å^{-1}. The spectral properties are calculated, the WF is determined as $W = 4.86$ eV, which is in reasonable agreement with the experimental values of 4.90(2) eV [160] and 4.94 eV [161], and reasonable agreement with a PBEsol DFT derived value of 4.98 eV [162]. The surface terminations using the density threshold approach are determined to be 50.40 Å and 28.44 Å for the upper and lower surface respectively. The surface energy calculated following Equation (5.1) is $E_{surface}(\mathrm{Cu}(111)) = 1.58\,\mathrm{J\,m^{-2}}$, which is in good agreement with a PBEsol DFT derived value of $1.59\,\mathrm{J\,m^{-2}}$ and in reasonable agreement with an experimentally derived value for a Cu surface of $1.79(19)\,\mathrm{J\,m^{-2}}$.

Calculating the photoemission response for the Cu(111) surface using the 3-step and 1-step model gives the curves shown in Figure 5.16. The response curves are compared to the extended DS model [95] and experimental data for a Cu(111) single crystal measured with the TESS instrument [151, 152].

The explicit 1-step and 3-step contributions near threshold and around 0.7 eV of excess energies are given in Figure 5.17 and Figure 5.18. It becomes clear, that the bands above the Fermi energy are contributing within the 1-step model, which is not the case for the 3-step model. The contributions near threshold for the 1-step model are further away from the origin than the 3-step model. This is consistent with a parabolic band dispersing away from the origin, which is clearer in the right panel of Figure 5.17. Mechanistically, this is also consistent. The parabolic band is much closer to the origin near the Fermi level, compared to above it. Thus the excitations for the 1-step model have a much higher MTE, than those for the 3-step model. Looking at the Cu(100) band structure, a series of bands just below and above the WF energy stand out. These are the states, which are the final bands for 3-step excitations near threshold. Since there are no bands below these, it is not possible to have excited electrons emit from these states within the 3-step model.

In the case of the 1-step model, however, the free electron state's energy can take any value and an emission is registered, as long as the final energy is above or just below the vacuum level. This explains the detailed differences in excitation behaviour between the two figures and models, as well as the very different MTE values near and just above threshold.

When calculating the Fermi surface emissions for a photon energy of 16 eV the constant binding energy maps shown in Figure 5.19 are obtained. The hexagonal shape of the BZ is shown nicely and the series of parabolic bands around the origin are also evident. The Fermi surface emissions for the *Gkgrid* scheme are systematically lower than for the *crystal* scheme, but as stated before the emissions are extended beyond the BZ edge.

In summary the PE calculations for low-index Cu surfaces produce spectra, which in comparison with experimental results can give qualitative agreement, but show much more structure within the spectrum. The experimental data measured using the TESS instrument almost fully aligns with the extended DS model prediction. The samples used are single crystal Cu surfaces, so the application of the model by Saha et al. [45] for disordered surfaces, discussed in Section 3.2.2, should not be appropriate. The model by Saha et al, however, does give nearly the same prediction as the extended DS model. The use of low energy electron diffraction (LEED) showed a high degree of crystallinity, based on personal communication with the collaborators at the ASTeC, but no peer reviewed publication of this data is available as of writing. So it is not clear at this point, where the difference in structure for the MTE spectrum between theory and experiment originates from. Berglund and Spicer [88] discuss that for a material the DOS will be the important quantity for the PE spectrum, if non-direct transitions dominate. The emission model developed within this

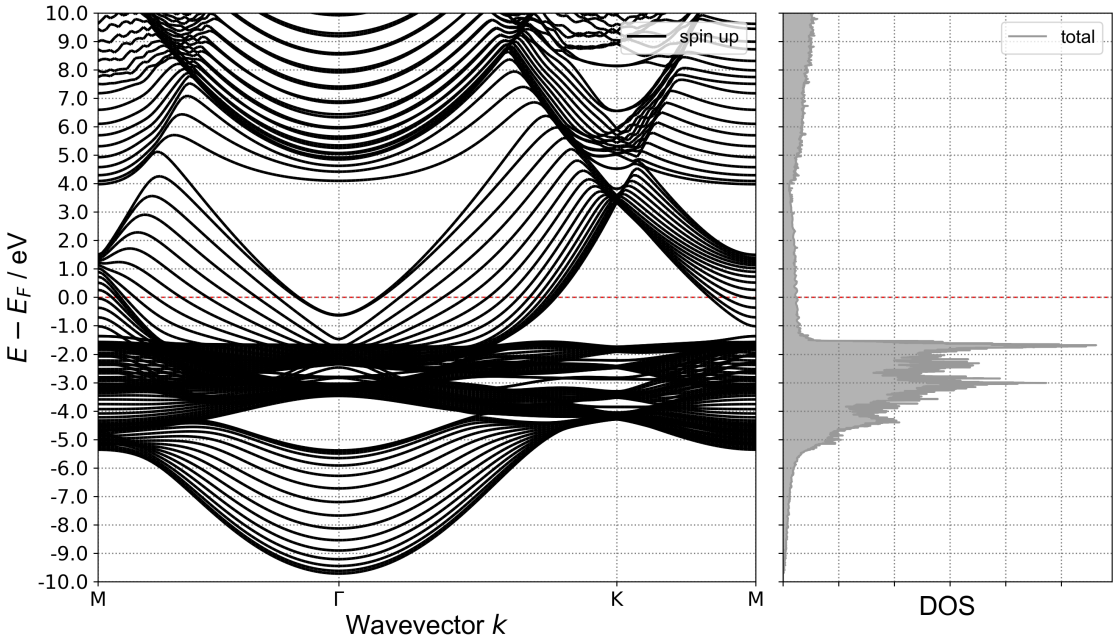


Figure 5.15: Calculated band structure and DOS for the Cu(111) 16 layer slab, the red dashed line indicates the Fermi energy.

work only considers direct transitions, so it is possible that including non-direct transitions would reduce the differences between the experimental and calculated spectra.

Calculating photoemission maps allows for detailed analyses of the different contributions to the QE and MTE spectra and also allows the visualisation of the Fermi surface emissions and other quantities of interest. No explicit comparison with ARPES data has been performed here, but the possible use case for interpreting other research from areas other than photocathodes is hopefully evident.

Other experimental data for low-index single crystal Cu surfaces, such as the measurements by [163] for a graphene coated Cu(110) photocathode, show a slow decrease of MTE with smaller E_{excess} values reaching the thermal floor at the threshold. This spectrum is in line with the experimental spectrum measured on TESS. For another experimental setup with a picosecond laser [164] the MTE spectrum for a single crystal Cu(111) around the threshold shows a minimum located very close to the work function and increasing both in energies below and above this value. The authors of this study apply an emission model based on the bulk electronic structure of Cu. The 1-Step model applied to the Cu(111) system also shows a minimum in the MTE spectrum. But this minimum is not located below the threshold, so it is not clear, how one would need to change the developed model to get similar results to the experimental results.

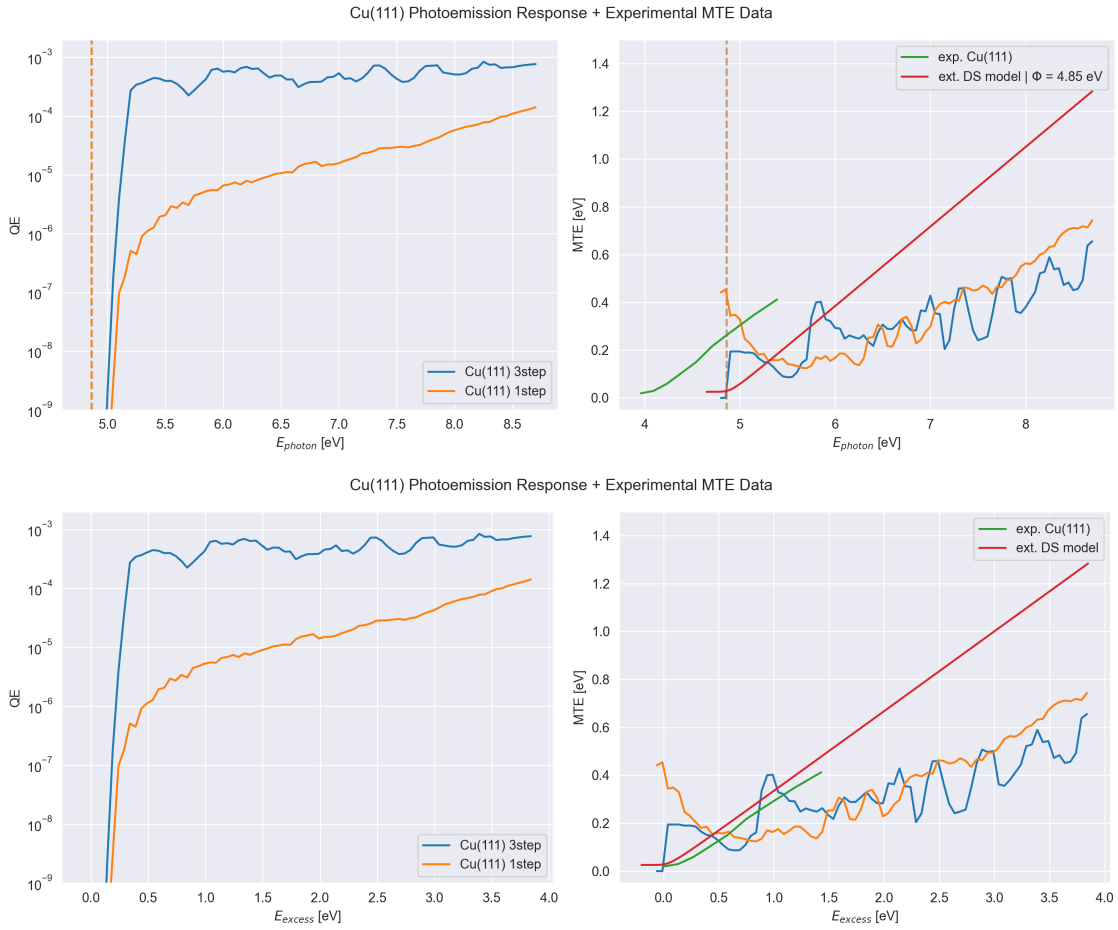


Figure 5.16: Photoemission Response calculated for a Cu(111) 16 layer slab using the 3-step and 1-step models. The energy axis is shown as both photon energy (top) and excess energy above the WF (bottom). The comparison with the extended DS model [95], as well as experimental data measured using the TESS instrument [151, 152] shows acceptable agreement for the comparable range for the 3-step model. The 1-step model has a very strong MTE response, which can be attributed to the low contributions from states away from the Γ point. The varying oscillations in both curves can be attributed to discrete states rather than a continuum contributing to the calculated photoemission response.

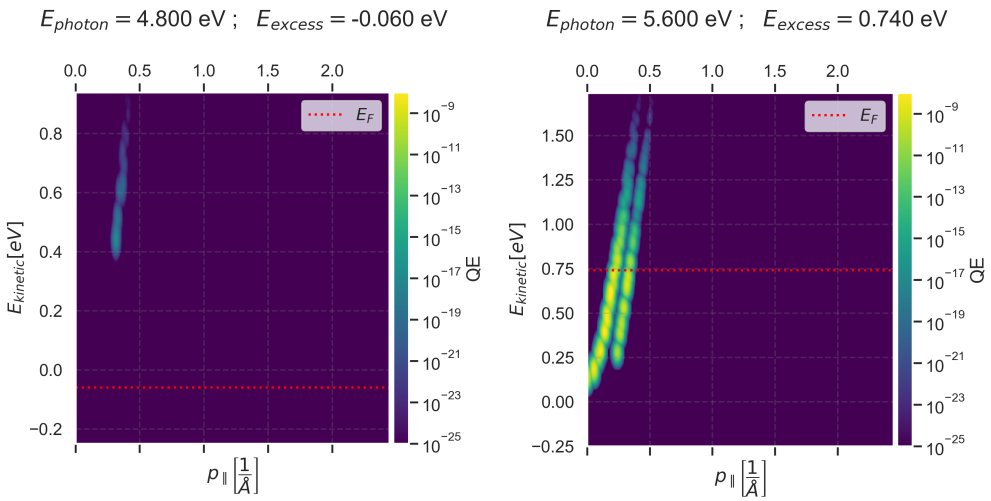


Figure 5.17: Broadened 1-step emissions for Cu(111) at 4.80 eV and 5.60 eV showing the kinetic energy vs transverse momentum distribution. The first calculated 1-step emissions are low intensity of emissions above the Fermi energy. This correlates with the high MTE value near threshold. At the higher energy the first parabolic state can fully contribute and a second state is also able to contribute.

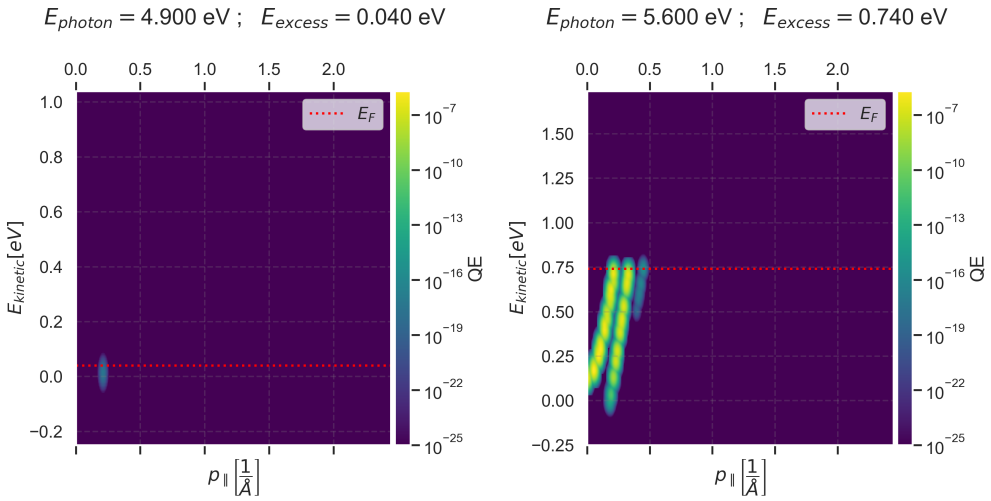


Figure 5.18: Broadened 3-step emissions for Cu(111) at 4.90 eV and 5.50 eV showing the kinetic energy vs transverse momentum distribution. The first calculated 1-step emissions are low intensity of emissions above the Fermi energy. This correlates with the high MTE . At the higher energy the first parabolic state can fully contribute and a second state is also starting to contribute.

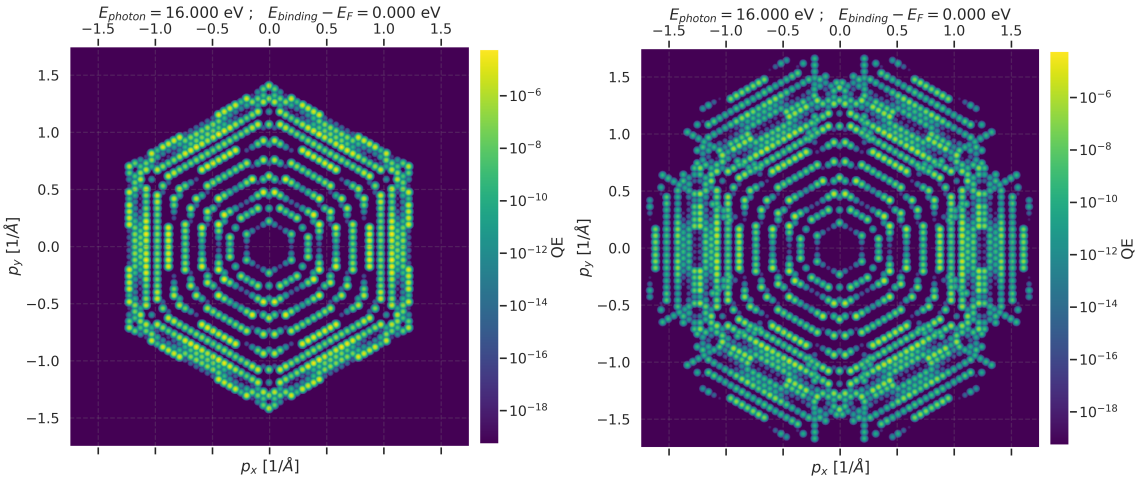


Figure 5.19: Constant binding energy maps for Cu(111) surface with a binding energy broadening of 0.026 eV. left: map using the *crystal* momentum scheme. The MP grid only extends to the outer edges of the BZ, so no calculated emission outside of these is expected. The hexagonal shape of the BZ is evident. right: map using the *Gkgrid* momentum scheme. The same features as in the *crystal* scheme case are present within the BZ boundaries, but the overall emission intensity is slightly reduced. Furthermore, the emission extends outside the first BZ, since the MP grid is extended for the *Gkgrid* momentum scheme, so this behaviour is as expected.

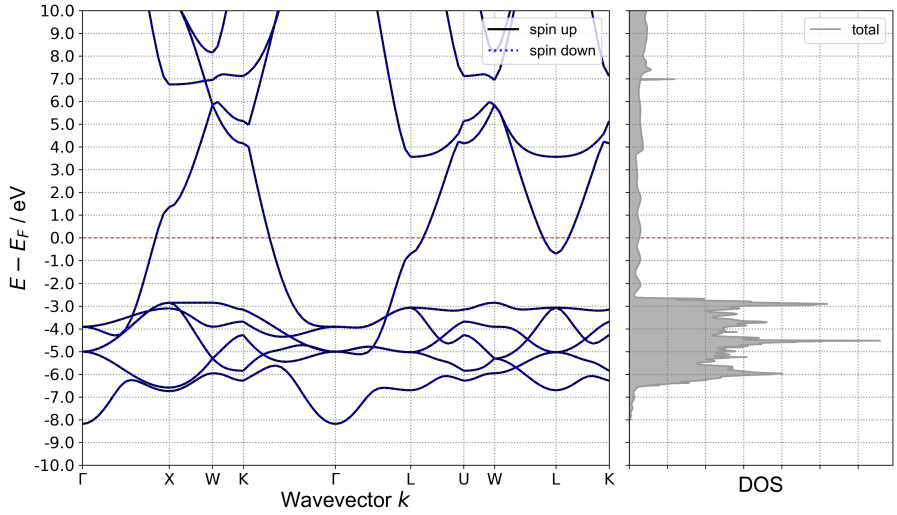


Figure 5.20: Calculated bulk Ag band structure and bulk DOS. The very sharp "peak" at 7 eV is due to the gradient dependent broadening scheme. The large set of flat bands across the BZ create this "peak", which should not be as prominent with a constant width broadening scheme.

5.3.5 Ag Bulk

In the next section on heterogeneous systems a number of systems has a Ag slab as substrate. To create the Ag surface substrate, a Ag bulk phase has to be modelled. Bulk Ag has the fcc structure ($Fm\bar{3}m$) and the unrelaxed primitive lattice parameter is set to $a'_{prim} = 2.90\,\text{Å}$ as found by the Materials Project database [153], corresponding to a conventional lattice parameter $a'_{conv} = 4.10\,\text{Å}$, with a single Ag atom centred on the origin.

The plane wave cut-off for the plane wave basis set is set to 827 eV, which gives a total energy convergence of $4 \times 10^{-5}\,\text{eV atom}^{-1}$. The `grid_scale` is set to 2.0 and the `fine_grid_scale` is set to 3.0. The PBEsol GGA functional is used to calculate the XC energy and the density is mixed using the Pulay density mixing approach as implemented in CASTEP. The total energy convergence tolerance is set to $1 \times 10^{-8}\,\text{eV atom}^{-1}$. The BZ is sampled using a MP grid of $12 \times 12 \times 12$ with an offset of one half step between the grid points. The number of electronic states is doubled to 11 and the system is treated as spin polarised. The electronic states also have a smearing of $k_B \cdot 300\,\text{K}$ applied to them.

The Ag bulk cell is optimised, with all cell angles constrained to 60°, until all components of the constrained stress tensor are $\leq 5 \times 10^{-4}\,\text{GPa}$. This results in a cell with the lattice parameter $a_{prim} = 2.8657\,\text{Å}$, which gives for the conventional cell $a_{conv} = 4.0528\,\text{Å}$. These values are within 1 % of the experimental value [165]. The LBFGS optimiser reports a bulk modulus of 120.93 GPa, which is about 17 % higher than experimental values [165], but within 1 % of other PBEsol calculations [166]. The calculated band structure and bulk DOS is shown in Figure 5.20.

Stretch	WF [eV]	$E_{surface}$ [J m^{-2}]
unstrained	4.125	8.46
AgMgO (4.6 %)	4.264	8.08
AgTiN (3.6 %)	4.137	8.12

Table 5.1: Table showing the calculated WFs and surface energies for different amounts of strain. The surface energy is calculated using Equation (5.1).

5.3.6 Ag(100) Surface

The Ag(100) surface is created using the `SlabGenerator` function in the `pymatgen` software package [159]. The Ag(100) surface slab are created with 16 layers from the relaxed Ag bulk structure, making sure that the surface normal is as close as possible to 90°. The resulting tetragonal cell has $a = 2.856$ Å, while the c cell side length is dependent on the system. In every case, however, the amount of vacuum in the z direction is ≥ 60 Å. All slab geometries are relaxed until the force components of atoms are $\leq 5 \times 10^{-3}$ eV Å^{-1}. The slabs WFs, stretch in percent and surface energy are given in Table 5.1.

The band structures are calculated to assess the effect a slight stretch has on the Ag(100) slab's and compared in Figure 5.21. The only visible difference between the two band structures is the slightly different dispersion of the parabolic bands extending from the Γ. This has the effect, that for the TiN case, one of the bands touches the Fermi energy, while the MgO case has a state dipping just slightly beneath the Fermi energy. Together with the slightly lower WF for the TiN cell this has an effect on the calculated PE response. The QE and MTE curves are shown and compared in Figure 5.22. The changes in the electronic structure result in the later onset of the QE response for the MgO cell system. Further, the calculated MTE is very near 0 until ≈ 0.4 eV excess energy, the emission threshold, and the MTE value is calculated as a very high value. This is likely due to the parts of the parabolic state further away from Γ contributing first. The decline of the MTE after the initial high value is also in line with more parts of the state contributing. This lowers the overall MTE value.

Calculating the Fermi surface emission for the Ag(100) at 16 eV gives the map shown in Figure 5.23. Around the origin the same near parabolic bands are present, as they are for the Cu(100) surface. The area near the X point, however, has a slight shift in the electronic state energies. So comparing these maps between Cu(100) and Ag(100) gives very different Fermi surface features. Compared to the Cu(100) surface, the MTE curve for Ag(100) tends higher than the linear increase for the extended DS model, while the Cu(100) shows a slower increase until the MTE suddenly shoots up.

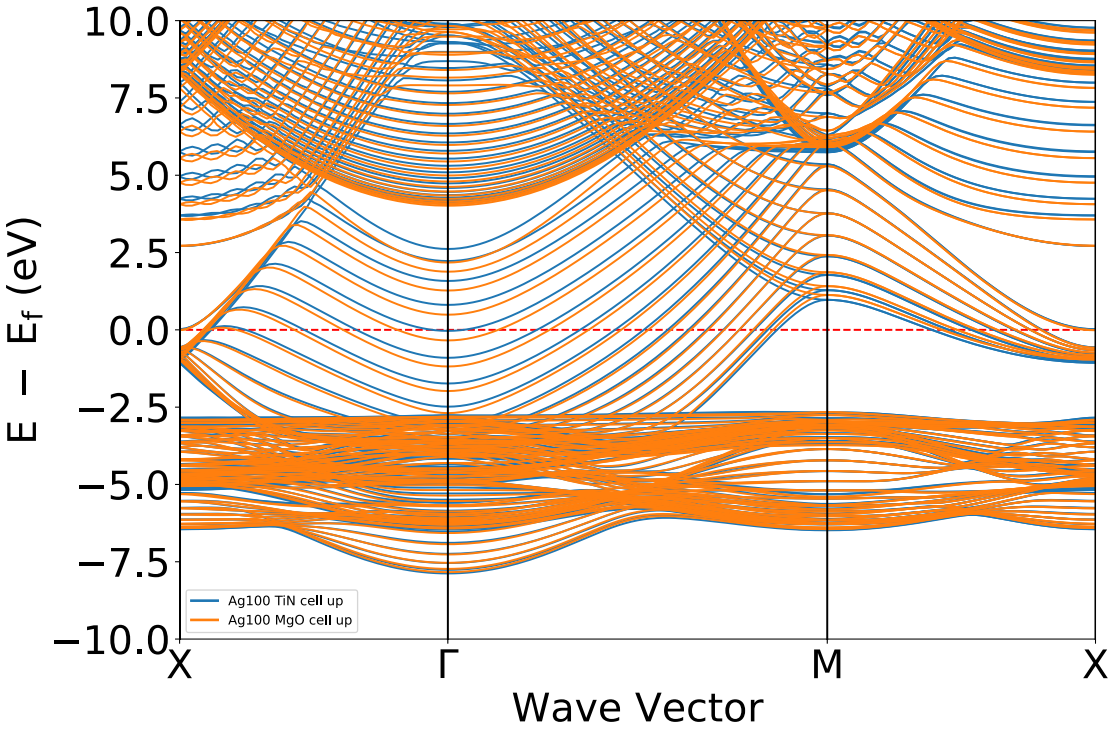


Figure 5.21: Calculated band structures for the Ag(100) layer slab with the lattice parameters of TiN and MgO. The different amount of stretch shows up in slightly different band energies around the Γ point.

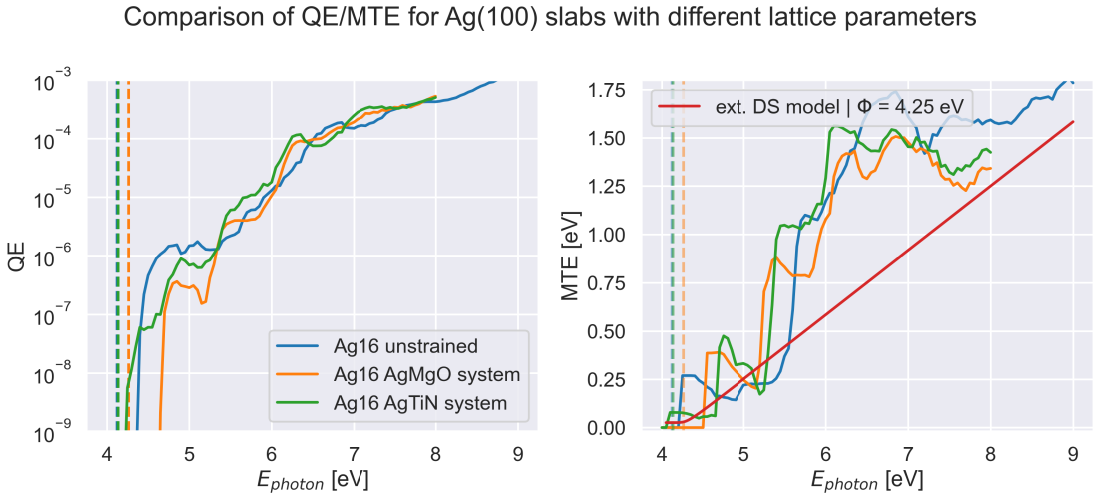


Figure 5.22: Calculated QE and MTE curves for different cell sizes and thus strain for a 16 layer Ag(100) slab. The late onset of the MTE and QE values is associated with the slightly different energies of states near the Fermi energy located at the Γ. The TiN cell structure has a band directly on the Fermi energy, while the MgO cell structure has the band dip just below the Fermi energy. See Figure 5.21 for more details.

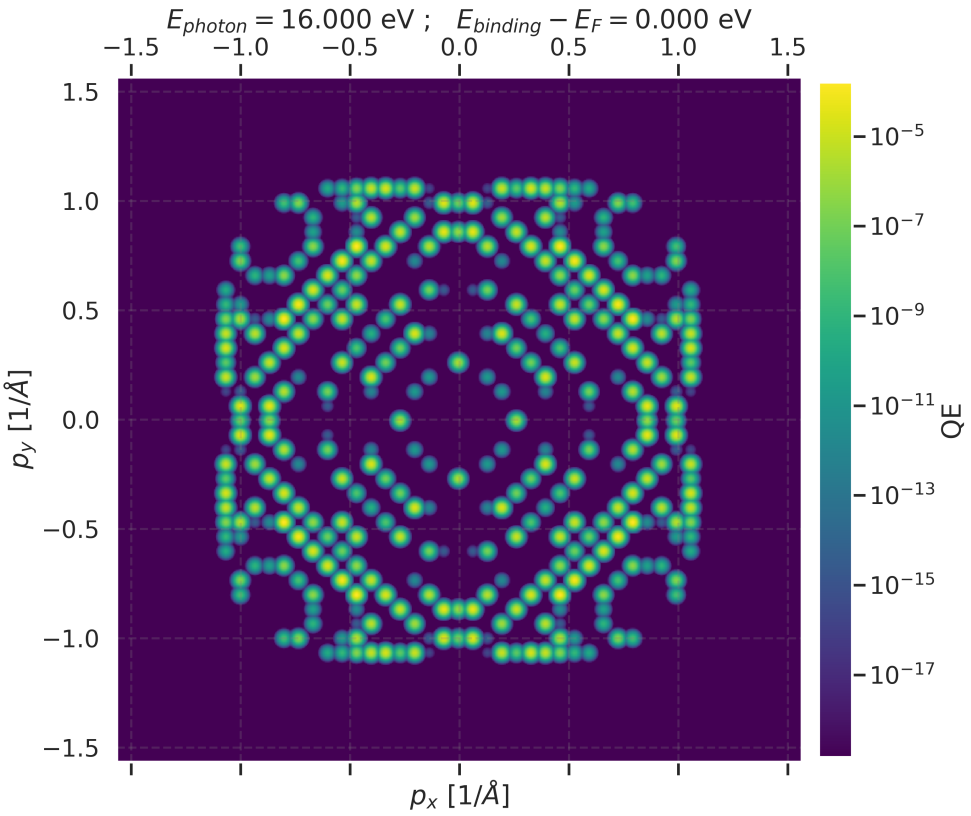


Figure 5.23: Constant binding energy maps for Ag(100) surface using the unstrained cell with a binding energy broadening of 0.026 eV. The map uses the *crystal* momentum scheme. Since the MP grid of **k** points only extends to the outer edges of the BZ, no calculated emission outside of these is expected. The tetragonal shape of the BZ is evident.

5.4 Heterostructures with protective Coatings for Photocathodes

One long-standing challenge in the field of photocathodes for next generation light sources has been the lifetime of photocathodes in the accelerator's vacuum environment. While the accelerator is kept under UHV conditions, it is quite common for a specific photocathode to degrade in performance over the course of hours to days. One approach to prolong the cathode's life span has been to put thin layers of oxides and other chalcogenides on the surface of the cathode. This approach can also modify the cathodes WF, thereby improving the cathode's performance even further. In the following sections the interfaces of Ag and Cu with MgO and TiN are modelled and their photoemission characteristics are calculated and compared to the bare surfaces'.

For the hetero-interfaces with MgO the question of the correct description for the electronic structure of MgO arises. It is well known that the GGA functionals used throughout this work can (significantly) underestimate the band gap of semiconductors due to electronic self-interaction and excessive delocalisation. There exist multiple ways of addressing this issue within CASTEP.

Firstly, there is the family of hybrid functionals, which combine a GGA based functional with exact HF exchange, which produce much better band gap estimates. A number of functionals is implemented within the CASTEP code. They do, however, require a substantially larger amount of compute power to use. With the constructed systems, using tens to hundreds of atoms, it would have been likely that the effort required to do these calculation with PW-DFT and hybrid functionals exceeded the computing resources available. One common approach is to perform geometry optimisations and SCF calculations using a GGA functional, like PBE or PBEsol, and only use the hybrid functionals for the spectral parameter calculations. This is possible in CASTEP and can in principle be used to calculate the bands for the spectral properties, although the developers warn to use this option with caution [167].

Secondly a popular option is using a DFT+U approach. This approach was initially described by Anisimov et al. [168–170]. The excessive de-localisation of electrons is counteracted by introducing a user defined energy penalty term for partially occupying a specified set of orbitals. This way these orbitals are more likely to be either fully occupied or empty. This approach is available as a DFT+U implementation in CASTEP [73]. When trying to use the DFT+U approach in CASTEP-23.1 to calculate the spectral properties, the calculations were always producing errors during the calculation. It was thus decided to use the GGA functional for all hetero-interface structures to show the capabilities of the model presented in this work.

5.4.1 MgO Bulk

To create the MgO overlayers, a MgO bulk phase has to be modelled. Bulk MgO has the fcc structure ($Fm\bar{3}m$) at room-temperature and normal pressure and the unrelaxed primitive lattice parameter is set to $a'_{prim} = 2.97\,\text{Å}$, which is the value found in the Materials Project database [153]. This corresponds to a conventional lattice parameter $a'_{conv} = 4.19\,\text{Å}$. The primitive cell consists of a Mg atom centred on the origin and an O atom at the fractional coordinate $1/2, 1/2, 1/2$.

The plane wave cut-off for the plane wave basis set is set to 1050 eV, which results in a total energy convergence of $5 \times 10^{-4}\,\text{eV atom}^{-1}$. The `grid_scale` is set to 2.0 and the `fine_grid_scale` is set to 3.0. The PBEsol GGA functional is used and the density is mixed using the Pulay density mixing approach as implemented in CASTEP. The total energy convergence tolerance is set to $1 \times 10^{-8}\,\text{eV atom}^{-1}$. The BZ is sampled using a MP grid of $11 \times 11 \times 11$ without any offset. The number of electronic states is doubled to 16. The electronic states also have a smearing of $k_B \cdot 300\,\text{K}$ applied to them.

The MgO bulk cell is optimised, with all cell angles constrained to 60°, until all components of the constrained stress tensor are $\leq 1 \times 10^{-1}$ GPa. This results in a cell with the lattice parameter

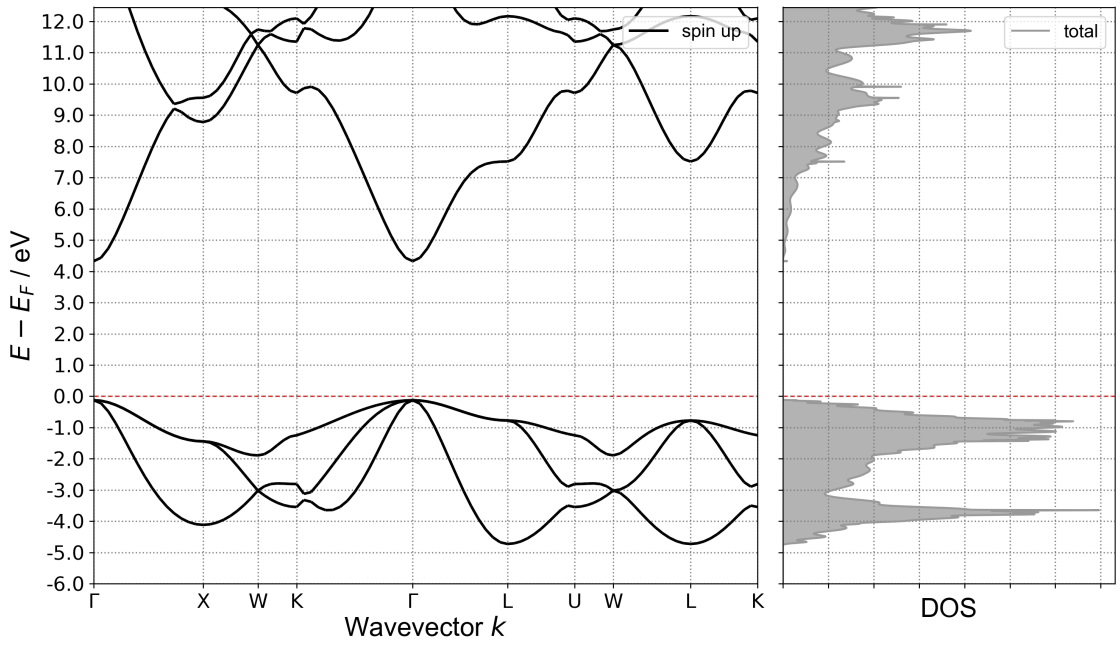


Figure 5.24: Band structure and DOS for the MgO bulk structure. The band gap is a direct gap of 4.452 eV at the Γ point. The very sharp peaks around 4.5 eV, 7.5 eV and 9.8 eV are due to the gradient dependent broadening. The flat band sections in the BZ at these energies cause the broadening of these contributions to become as tight as possible, representing these peaks.

$a_{prim} = 2.9971$ Å, which gives for the conventional cell $a_{conv} = 4.2384$ Å. These values are within 1.5 % of other PBEsol calculations for TiN [171]. The LBFGS optimiser reports a bulk modulus of 155.05 GPa. Using the Murnaghan equation of state [172] as implemented in the Atomic Simulation Environment [173, 174] the calculated bulk modulus is 154.67 GPa. Calculating the band structure and DOS for the bulk system results in the plots given in Figure 5.24. The calculated bandgap is a direct bandgap of 4.452 eV located at the Γ point. This is much lower, than the experimentally measured gap of 7.8 eV [175], but within 2.8 % of other PBEsol based calculations [176].

5.4.2 TiN Bulk

For the TiN overlayers, a TiN bulk phase has to be modelled. Bulk TiN has the fcc structure ($Fm\bar{3}m$) at room-temperature and normal pressure[177] and the unrelaxed primitive lattice parameter is set to $a'_{prim} = 3.00$ Å, which is the value found in the Materials Project database [153]. This corresponds to a conventional lattice parameter $a'_{conv} = 4.24$ Å, with a Ti atom centred on the origin and a N atom at the fractional coordinate $1/2, 1/2, 1/2$.

The plane wave cut-off for the plane wave basis set is set as 784 eV, which gives a total energy convergence of 5×10^{-4} eV atom^{-1}. The `grid_scale` is set to 2.0 and the `fine_grid_scale` is set to 3.0. The PBEsol GGA functional is used and the density is mixed using the Pulay density mixing approach as implemented in CASTEP. The total energy convergence tolerance is set to 1×10^{-8} eV atom^{-1}. The BZ is sampled using a MP grid of $15 \times 15 \times 15$ without any offset. The number of electronic states is doubled to 18 and the system is treated as spin-polarised. The electronic states also have a smearing of $k_B \cdot 300$ K applied to them.

The TiN bulk cell is optimised, with all cell angles constrained to 60°, until all components of the constrained stress tensor are $\leq 1 \times 10^{-1}$ GPa. This results in a cell with the lattice parameter $a_{prim} = 2.9714$ Å, which gives for the conventional cell $a_{conv} = 4.2021$ Å. These values are

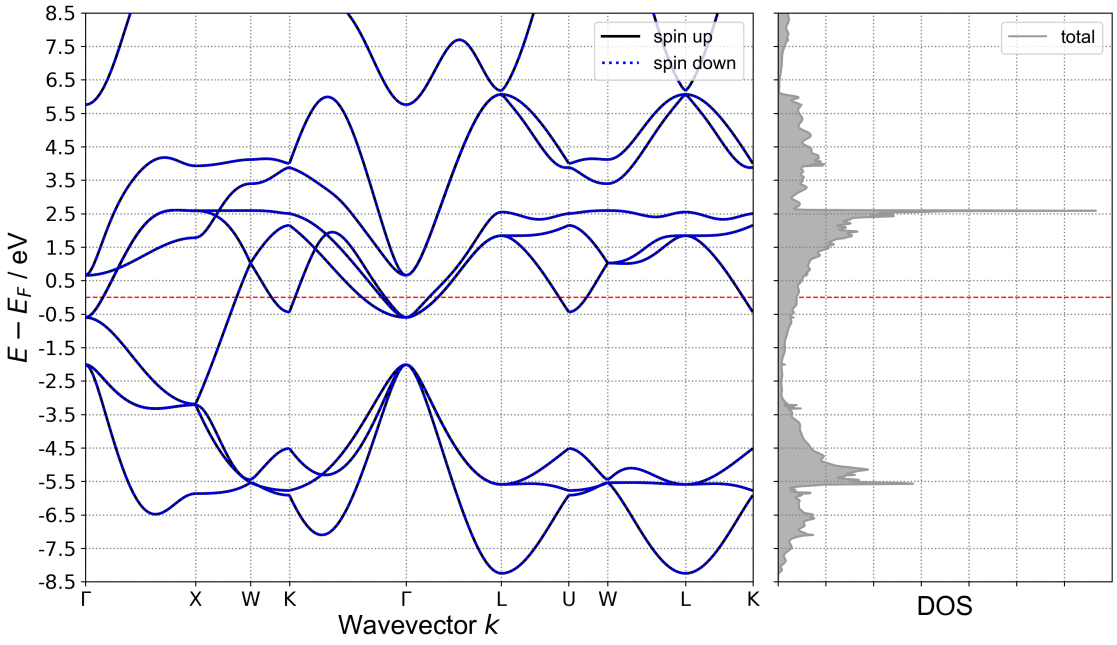


Figure 5.25: Band structure and DOS for the TiN bulk system.

within 1 % of experimental measurements [177]. The LBFGS optimiser reports a bulk modulus of 302.55 GPa, which is within 3 % of both theoretical (294.6 GPa)[178] and experimental values (292 GPa) [178]. The calculated bulk band structure and DOS is shown in Figure 5.25.

5.4.3 MgO(100) on Ag(100)

For the given modelling parameters the determined lattice parameters are within 4.6 % of each other, i.e. Ag $a_{conv} = 4.0528$ Å and MgO $a_{conv} = 4.2384$ Å. This means to create a coherent interface between the two materials can be created by stretching the Ag slab substrate by the same amount. For a metal like Ag one can still expect to retain a good representation of the electronic structure for this amount of distortion.

The interface is built by creating a Ag(100) slab with 16 layers using the `SlabGenerator` in `pymatgen` [159]. A slab with the appropriate amount of layers (0-3,6) is created for the MgO part of interface with the same approach. This gives a tetragonal cell with $a = 2.9971$ Å. The Ag(100) slab's tetragonal cell is scaled to the same lateral dimensions, while not changing the atoms' z coordinates. The two slab structures are then combined in a MgO-Ag-MgO order to form an interface slab with two equal surface terminations. The alignment between the two materials in the x, y-plane is set, so that the O atoms occupy the *ontop* site of the Ag(100) surface. This has the lower formation energy compared to the Mg atom occupying the *ontop* site, as determined by Chang, Noakes and Harrison [38].

The surface geometries are created as described and the cell size and atoms' coordinates are adjusted, that at least 60 Å of vacuum are present in between each replica. The plane wave basis cut-off is set to 1050 eV and the interface slab geometry is relaxed for all systems until all force contributions on all atoms are $\leq 5 \times 10^{-3}$ eV Å^{-1}. The geometry optimisation uses MP grid of $9 \times 9 \times 1$ and the spectral properties are calculated non-self-consistently on a $33 \times 33 \times 1$ MP grid of $\mathbf{k}$ points. The determined WF and surface termination values for the different interfaces are given in Table (5.2). The calculated band structure and DOS for the 16L Ag(100)/6L MgO(100) is shown in Figure 5.29.

# MgO layers	WF [eV]	$E_{adhesion}$ [J m^{-2}]
0	4.264	$E_{surface}$ =8.23
1	3.173	8.57
2	2.738	8.21
3	2.784	-2.92
6	2.643	8.32

Table 5.2: Table showing the calculated WFs and surface terminations for the different numbers of MgO(100) layers on a Ag(100) substrate. The adhesion energy for the interfaces is calculated using the formula provided by Shan et al. [179]. The adhesion energy for 3 MgO layers is likely incorrect, which is likely due to difficulty during the optimisation of the 3 layer MgO slab.

The photoemission response for the MgO/Ag interface model is calculated using the `adaptive` broadening scheme with a smearing ratio of 0.4, the bin width for the JDOS $bin_{jdos} = 0.05\,\text{eV}$, the scattering is calculated using an IMFP constant $\lambda_{\text{Ag}} = 6.13\,\text{Å}$, which has been previously used [11], and the temperature smearing is set to 300 K. When comparing the calculated QE and MTE curves shown in Figure 5.26 a large increase in the calculated MTE value around $\approx 2.9\,\text{eV}$ is seen in all the MgO interface structures. For the MgO structures with 3L MgO and 6L MgO, however, there is also a dramatic decrease just after. It is informative to consider the exact emission patterns around this high peak of MTE. Figure 5.28 shows three emission maps in the $X \leftarrow \Gamma \rightarrow M$, i.e. $90° \leftarrow \Gamma \rightarrow 45°$ directions for the 6L MgO interface system. At 4.7 eV, i.e. when the drastic increase in MTE starts, a parabolic state along the $\Gamma \rightarrow M$ is starting to emit. This results in a strong increase of the MTE as the emission is relatively far away from Γ. At 4.85 eV, i.e. at the high MTE values, the state is emitting fully and finally at 5.05 eV the flat states $\approx 2.5\,\text{eV}$ below the Fermi energy near the Γ point are emitting. This creates a lot of emission very close to Γ and thus drastically reduces the total MTE. A similar explanation should hold for the large peak for the 16L Ag(100)/3L MgO(100) interface.

This discussion also implies, that the presence of individual states, rather than a continuum, have a big impact on the calculated MTE curve. If the number of explicit layers is increased, it can also be expected, that the distance between the parabolic states in the band structure is also decreased. This should have an overall dampening effect on the "swings" in the MTE curve, but does require the construction of larger and larger slab models. It is also possible, that the choice to not currently consider scattering events during propagation or not having yet implemented the more accurate versions of the 1-step model would help to lessen the impact of finite size effects.

Whether the qualitative comparison with experimental data or more accurate models are required for a specific application, is still to be determined. The insights that can be gained from connecting specific features in the band structure with features in the MTE or QE curves are already a big step towards understanding how surface electronic structure and PE characteristics are linked. With this the specific design of thin films and other surface features can become even more targeted than it is already being done in research organisations today.

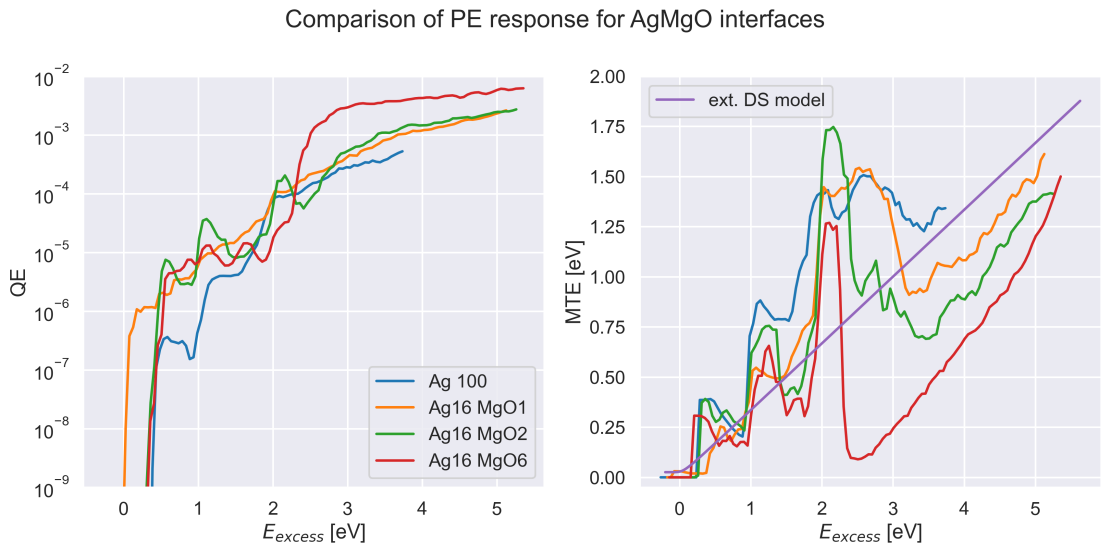


Figure 5.26: Calculated QE and MTE curves for the bare Ag(100) surface compared to the interface structure with one, two, and six layers of MgO on both surfaces. The large MTE jumps for the MgO interfaces at $\approx 2.9\,\text{eV}$ are quite prominent. For more detailed contributions see Figure 5.28 for specific state contributions.

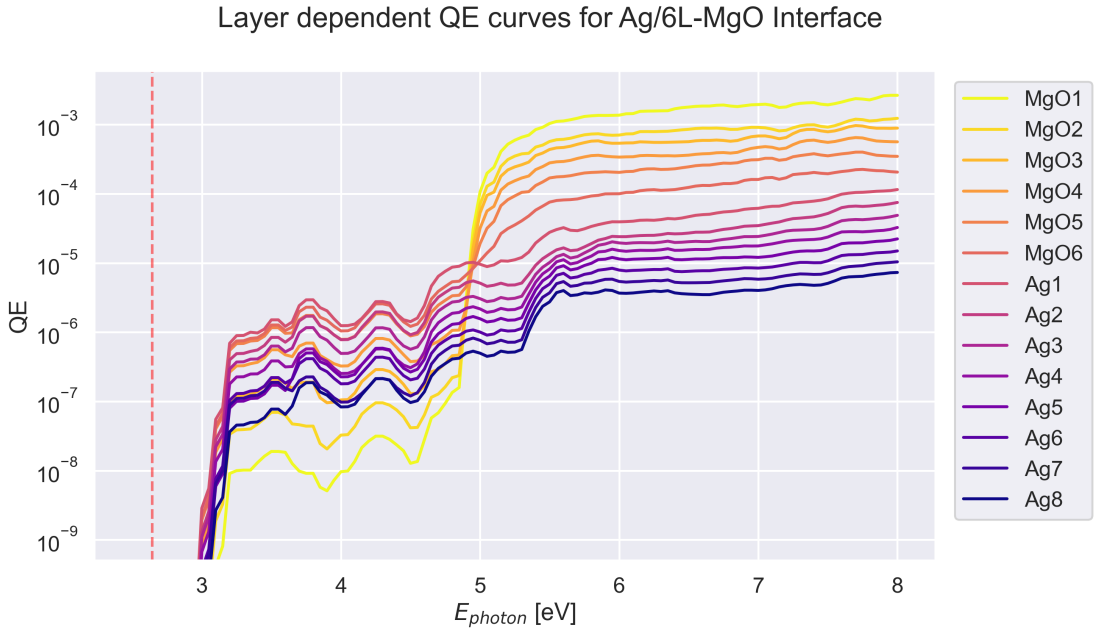


Figure 5.27: Layer QE contributions for 16L Ag(100)/6L MgO interface structure. A clear distinction in the response curve exists and the rule, that the more outer layers contribute more, holds true. Interestingly the MgO layers contribute the majority of QE above $\approx 5\,\text{eV}$, while the Ag metal layers do this below this photon energy.

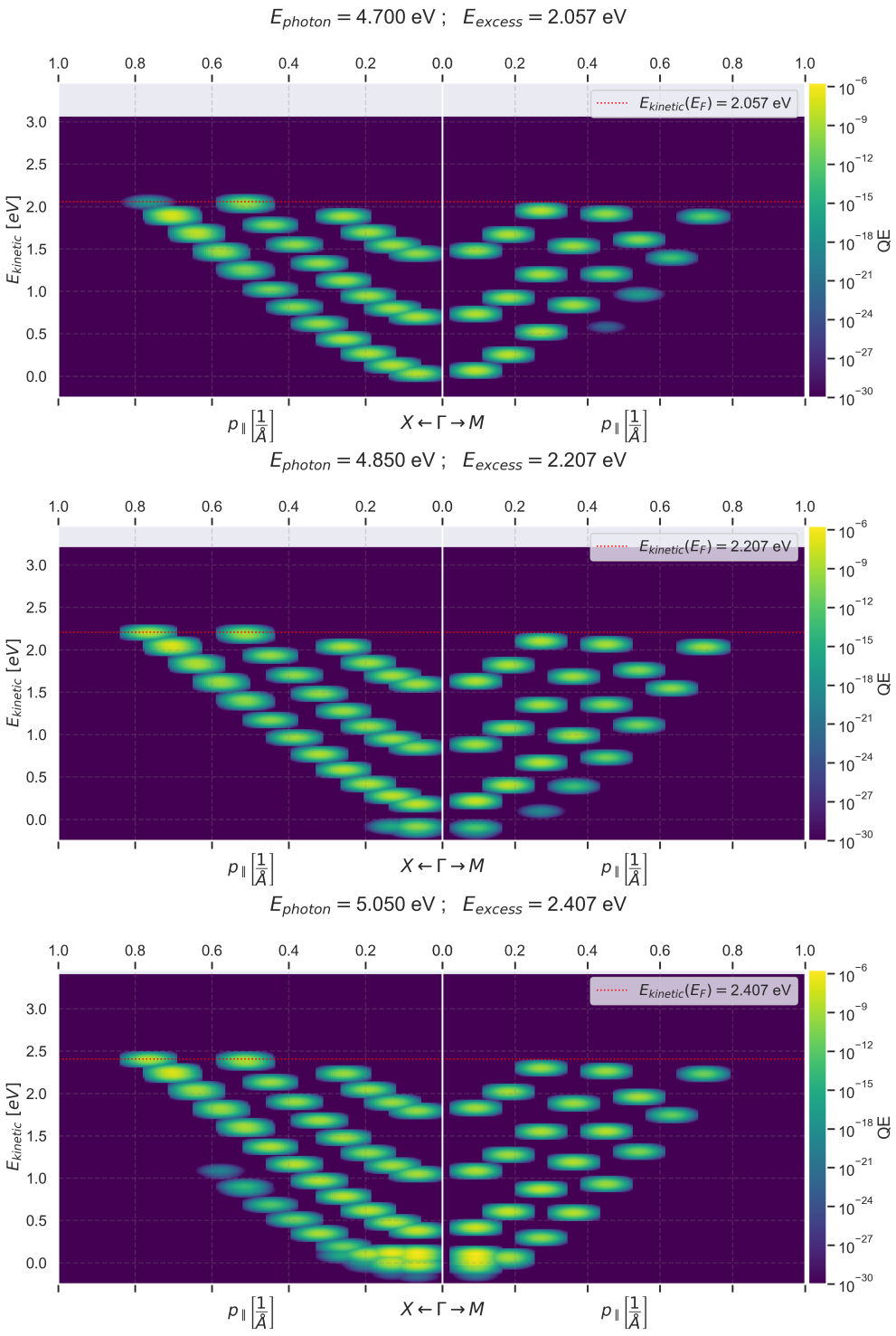


Figure 5.28: Emission Maps of $E_{kinetic}$ vs $p_\parallel$ at energies representative of the large peak in the MTE curve for the 6L MgO(100)/16L Ag(100) model. The parabolic state on the right hand side is starting to emit around 4.7 eV and at 4.85 eV it is able to fully emit. This drastically increases the calculated MTE, as there is little emission around Γ. Once 5.05 eV are reached, however, the flat bands a near Γ are able to emit, which dramatically lowers the MTE, as now a large part of the emission is from near Γ.

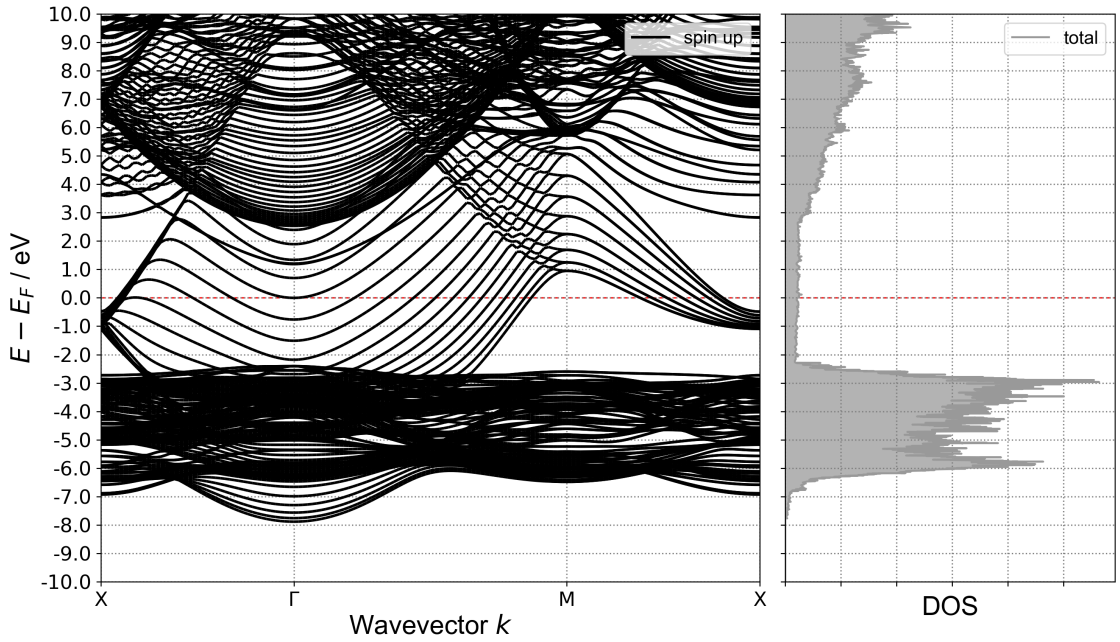


Figure 5.29: Calculated band structure and DOS for the 16L Ag(100)/6L MgO(100) on both surfaces.

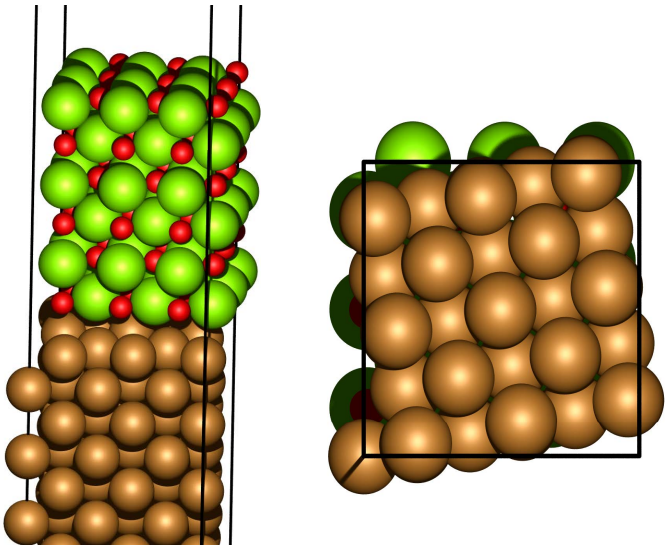


Figure 5.30: left: Render showing the top half of the Cu(100)/MgO(100) interface supercell. right: Top view of the Cu(100) substrate supercell.

5.4.4 MgO(100) on Cu(100)

Compared to the MgO/Ag interface, the difference between the lattice parameters for Cu and MgO is much greater, i.e. $a_{conv}(\mathrm{Cu}) = 3.5630\,\text{Å}$ and $a_{conv}(\mathrm{MgO}) = 4.2384\,\text{Å}$. This represents a difference of almost 19 %, so the interface cannot be made coherent by just stretching one or both surface slab structures. Instead the interface geometry is a supercell structure created using the `CoherentInterfaceBuilder` implemented in the `pymatgen` software package [159]. It uses the algorithm of lattice matching two supercell geometries for the surface developed by Zur and McGill [180]. The smallest interface geometry found has a 3x3 MgO(100) supercell and the Cu(100) substrate is a rotated supercell with 13 atoms. The interface structure has been constructed for number of different MgO layers (0-3,6). The maximum number of layers was informed by the experimental work, which also provided the MTE values measured on the TESS experiment [151, 152] The interface supercell with 6 MgO layers is shown in Figure 5.30. The 3×3 supercell for the MgO is clearly visible and the rotated nature of the Cu supercell is also evident.

The interface models are geometry optimised using a plane wave basis cut-off of 1050 eV using a MP grid of $3 \times 3 \times 1$ **k** points and the optimisation is continued until all force contributions on all atoms are $\leq 5 \times 10^{-3}\,\text{eV Å}^{-1}$. The spectral properties are calculated non-self-consistently on an MP grid of $7 \times 7 \times 1$.

To characterise the interface's electronic structure the band structure is expected to not give useful insights, since the interface is a supercell structure, so instead the PDOS is used. The PDOS contributions broken down layer by layer are given in Figure 5.31. The innermost Cu layer shows good reproduction of the bulk Cu DOS, meaning the slab is able to reproduce both the surface characteristics, as well as the bulk material. The DOS for the MgO layers does represent the bulk MgO better for the middle layers, but never manages to fully approximate the bulk conditions. This is as expected for a 6 layer overlayer slab, but since it does represent the experimentally observed average coverage, further convergence testing with higher coverages is not performed here.

The calculated photoemission response and experimental data for the Cu/MgO interfaces are given in Figure 5.32. Comparing the Cu/6L MgO interface MTE with the experimental MTE data, shows qualitative representation. The difference in the two curves near threshold could be explained by scattered electrons, since these are not included in the current calculations. At photon energies

# MgO layers	WF [eV]	$E_{adhesion}$ [J m^{-2}]
0	4.452	$E_{surface}$ =1.84
1	3.266	1.38
2	3.099	1.06
3	3.050	1.08
6	3.002	1.07

Table 5.3: Table showing the calculated WFs and surface terminations for the different numbers of MgO(100) layers on a Cu(100) substrate. The adhesion energy for the interfaces is calculated using the formula provided by Shan et al. [179]

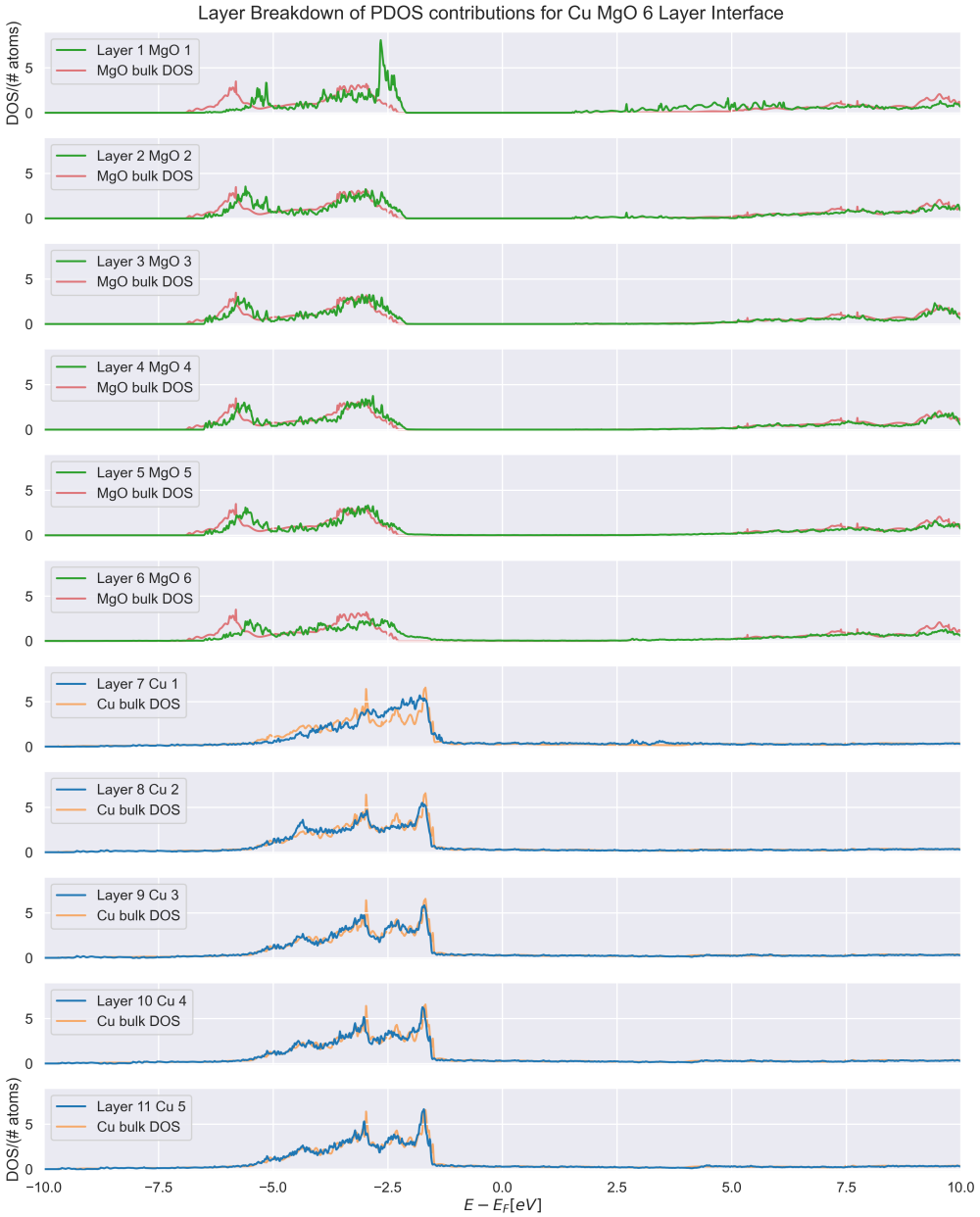


Figure 5.31: PDOS contributions broken down by layer. The innermost Cu layer shows good reproduction of the bulk DOS, while the inner MgO layers never reach good reproduction of the DOS. The number of MgO layers was informed by the collaborators providing the measurements.

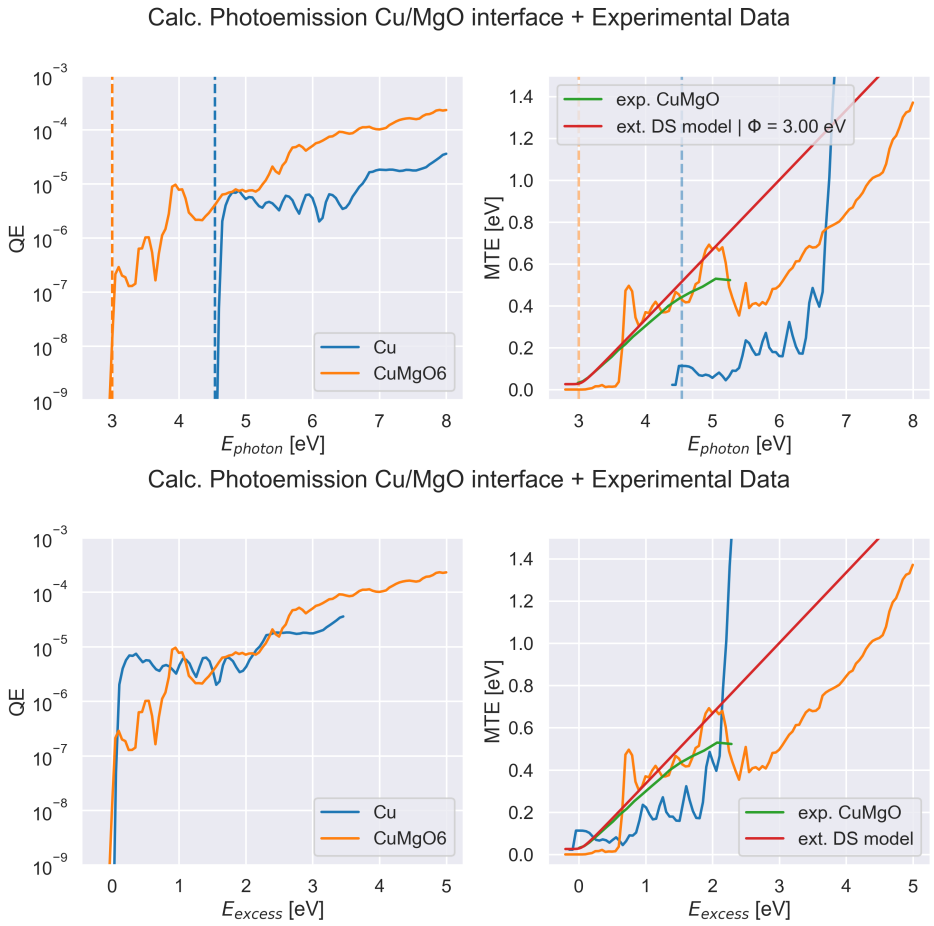


Figure 5.32: Comparison of QE and MTE curves for the bare Cu(100) supercell structure and the interface with 10L Cu/6L MgO, as well as the extended DS model and a set of experimental measurements using the TESS instrument [151, 152]. There is good agreement above $\approx 3.7\,\text{eV}$ for the rest of available experimental data.

above 4 eV the calculated curve is much closer the experimental values, until it shoots up to a plateau at $\approx 4.8\,\text{eV}$. A similar plateau is observed in the experimental data and the photon energy where the calculated MTE shows a drop is also present by a slight decrease of the experimental value. An analogous explanation to the one used in Section 5.4.3 for the strong changes in MTE by Ag/MgO, can be used here. This helps to understand the relatively rapid changes in the MTE curve at $\approx 5.2\,\text{eV}$ for the 10L Cu(100)/6L MgO(100). Starting at $\approx 4.7\,\text{eV}$, or $\approx 1.8\,\text{eV}$, states relatively far away from Γ contribute a large amount of transverse momentum. In the PDOS picture there are clearly Cu based states present at this binding energy. Looking at $\approx 2.1\,\text{eV}$ in the PDOS figure shows the valence band edge for most of the MgO layers. When these states are able to contribute to the overall emission, they lower the overall MTE markedly. This is clearly visible in the MTE curve in Figure 5.32.

With these two examples one can start to formulate a possible approach for lowering the expected MTE. The MTE should decrease rapidly, whenever strongly emitting states close to Γ are starting to contribute. If the band edge of a material can be changed, such that the rapid decrease in MTE is just before the photon energy of interest, then the hetero-junction photocathode should have have much better performance compared to the photocathode without the overlayers.

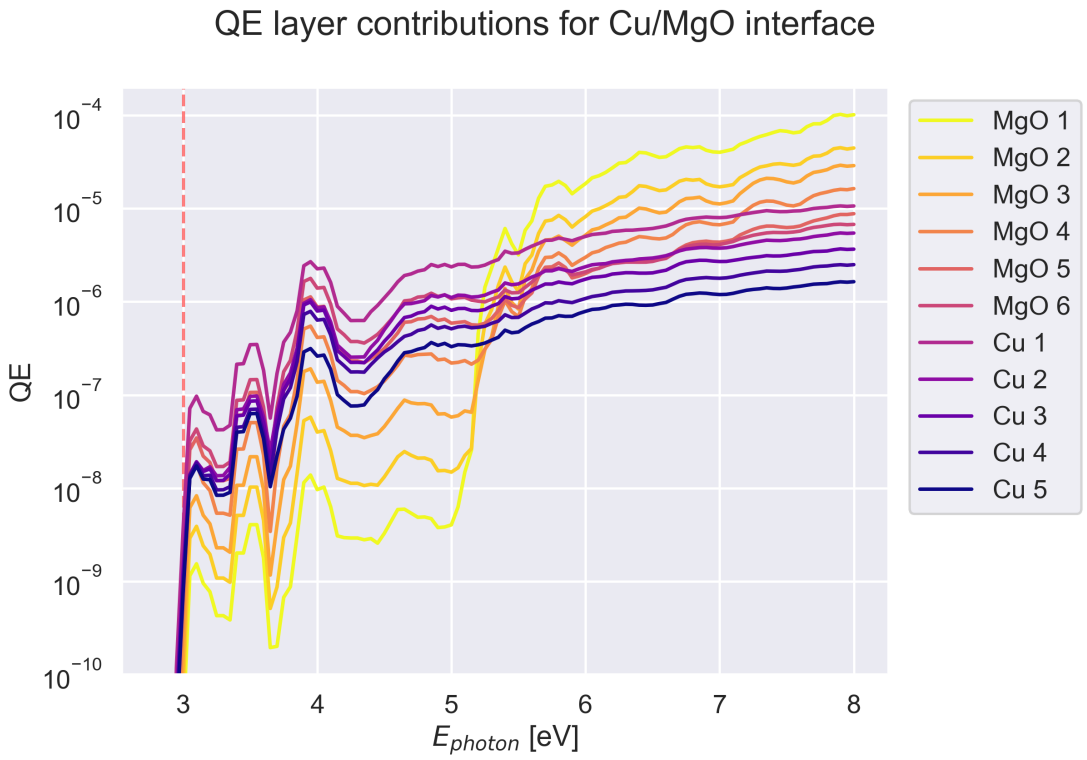


Figure 5.33: Layer based QE contributions. The general rule that layers further out towards the surface, holds true here. Furthermore a distinct structure between the two materials and their response curves is visible, which is to be expected for two materials with very different electronic structure (metal vs semiconductor/insulator.

5.4.5 TiN(100) on Ag(100)

For the given modelling parameters the determined lattice parameters for Ag and TiN are within 3.6 % of each other, i.e. $a_{conv}(\mathrm{Ag}) = 4.0528\,\text{Å}$ and $a_{conv}(\mathrm{TiN}) = 4.2021\,\text{Å}$. Thus the considerations for creating an inherent interface between the two materials are the same as for the MgO/Ag interface.

The interface is built by creating a Ag(100) slab with 16 layers using the `SlabGenerator` in `pymatgen` [159] and making sure the surface normal is as close to 90° as possible. A slab for the TiN part of interface with the appropriate amount of layers (0-3,7) is created using the same approach. This gives a tetragonal cell with $a = 2.9714\,\text{Å}$. The Ag(100) slab's tetragonal cell is scaled to the same lateral dimensions, while not changing the atoms' z coordinates. The two slab structures are then combined in a TiN-Ag-TiN order to form an interface slab, where the N atom sits `atop` the Ag atom below, similar to the Ag/MgO interface.

The interface models are geometry optimised using a plane wave basis cut-off of 827 eV using a MP grid of $9 \times 9 \times 1$ $\mathbf{k}$ points and the optimisation is continued until all force contributions on all atoms are $\leq 5 \times 10^{-3}\,\text{eV}\,\text{Å}^{-1}$. The spectral properties are calculated non-self-consistently on an MP grid of $33 \times 33 \times 1$.

Calculating the band structure for 16L Ag(100)/7L MgO(100), shown here in Figure 5.25 a number of differences compared to the Ag/MgO system become obvious. The MgO had defined regions, where states are contributing to the electronic structure. The TiN, on the other hand has bands throughout the entire binding energy range and shows no clear band edge feature, like it can be seen in the PDOS contributions in Figure 5.31. Looking to the calculated QE and MTE curves, shown in Figure 5.36, the qualitative features a different, but some general inferences are still possible. The calculated MTE curve is markedly lower than the bare Ag100 surface. This can be attributed to the presence of TiN states near Γ throughout the binding energy range from 0 eV to 2.5 eV. At ≈ 2.5 eV excess energy, or ≈ 5.2 eV photon energy, the band structure shows the beginning of a binding energy range with lots of flat states. Comparing this to the MTE curve, it shows the familiar drop in calculated MTE before starting to rise again.

Furthermore, a big difference is evident in the QE curves. The presence of TiN overlayers not only decreases the predicted WF by ≈ 1.5 eV, but also introduces new states near the Fermi level. This can be seen both the band structure and total DOS in Figure 5.25. Since they are located in the surface layers, they are able to contribute significantly to the QE. This is corroborated by the much stronger QE response in the Ag/TiN interface structures compared to the bare Ag surface. The layer based QE contributions shown in Figure 5.35 add to this, showing a much stronger response of the surface TiN layers, compared to the Ag substrate layers.

In comparison the MgO-metal interfaces layer based QE shows the lowest contributions from the MgO film at and near threshold. This is due to the presence of an electronic gap in the material as evident from the PDOS. The MgO layer contributions do rapidly increase, once the photon energy is high enough for the nearly flat MgO valence bands to contribute emissions. The TiN, on the other hand, has a high DOS near E_F and further states at lower energies, making the TiN layer contributions very high directly at threshold. This also keeps the relative layer contributions of TiN above those of Ag across an energy range.

The layer based contributions in all systems also clearly show the impact of the depth based scattering probability. Layers of the same material have very similar response curves, but diminished by the lower emission probability of layers further below the surface. This means, that the QE response of the metal substrate layers is also diminished compared to the bare metal surface, as the thin film increases propagation lengths and thus the scattering probability. This is, however, mostly offset by the thin film response. In the MgO on Cu case a slight QE decrease near threshold can be observed compared to the bare Cu spectrum. This is one aspect to consider when

# TiN layers	W [eV] N *ontop*	$E_{adhesion}$ J m^{-2}
0	4.137	$E_{surface} = 8.12$
1	3.851	4.29
2	2.884	3.08
3	2.789	2.45
7	2.736	2.57

Table 5.4: Table showing the calculated WFs and interface formation energies for TiN(100) layers on a Ag(100) substrate. The adhesion energy for the interfaces is calculated using the formula provided by Shan et al. [179]

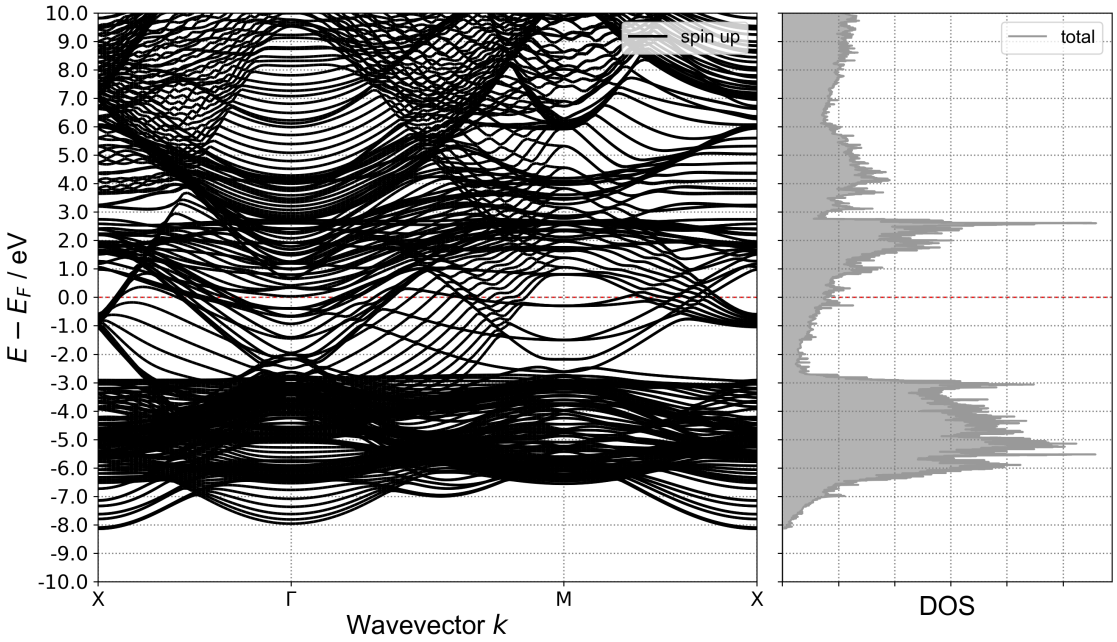


Figure 5.34: Calculated band structure for 16L Ag(100)/6L TiN(100) interface slab and the DOS for the structure.

investigating deposited thin films.

The presence of further density near E_F and its effects on the threshold emission response has already been discussed. Away from threshold a significant change to the calculated MTE response is evident. The thin films contribute flat valence bands near the Γ point and add emissions with little transverse momentum, lowering the overall MTE value. The energies of these nearly flat states relative to existing low dispersion d-states in the metal can have an effect on this change. The MgO on Ag system shows a much stronger response compared to the MgO on Cu system. It is not entirely clear from the available data, how large the MTE contributions for each layer are, as this is not currently calculated in the emission model. Analysing this data could help to understand why in the MgO on Ag case the MTE response is calculated to change much more dramatically.
This change in the calculated MTE spectrum for the TiN on Ag system is also evident as a generally lower MTE value away from threshold. This can be linked to the extra electronic states contributed by the TiN in the interface that contribute low transverse momentum electrons. A similar, but less pronounced lowering of the MTE value $\approx 2.8\,\text{eV}$ above threshold is also observed.

In summary the combination of two materials in an interface model changes its characteristics in a number of important and useful ways. First, the interface's work function is consistently lowered

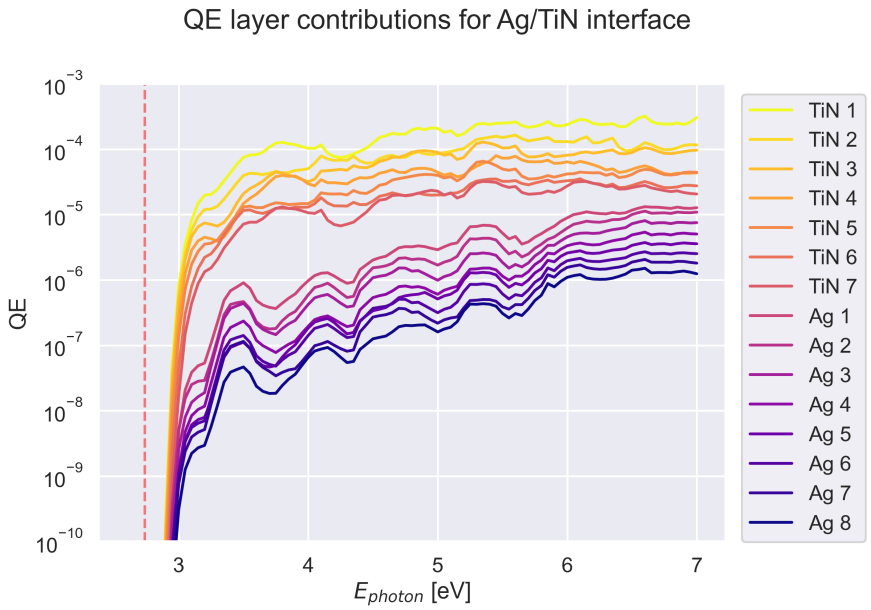


Figure 5.35: Layer QE contributions for the 16L Ag(100)/7L TiN(100) interface. The PE response is stronger from the TiN layers, but the difference is not as stark, as the metal/insulator case in Figure 5.27.

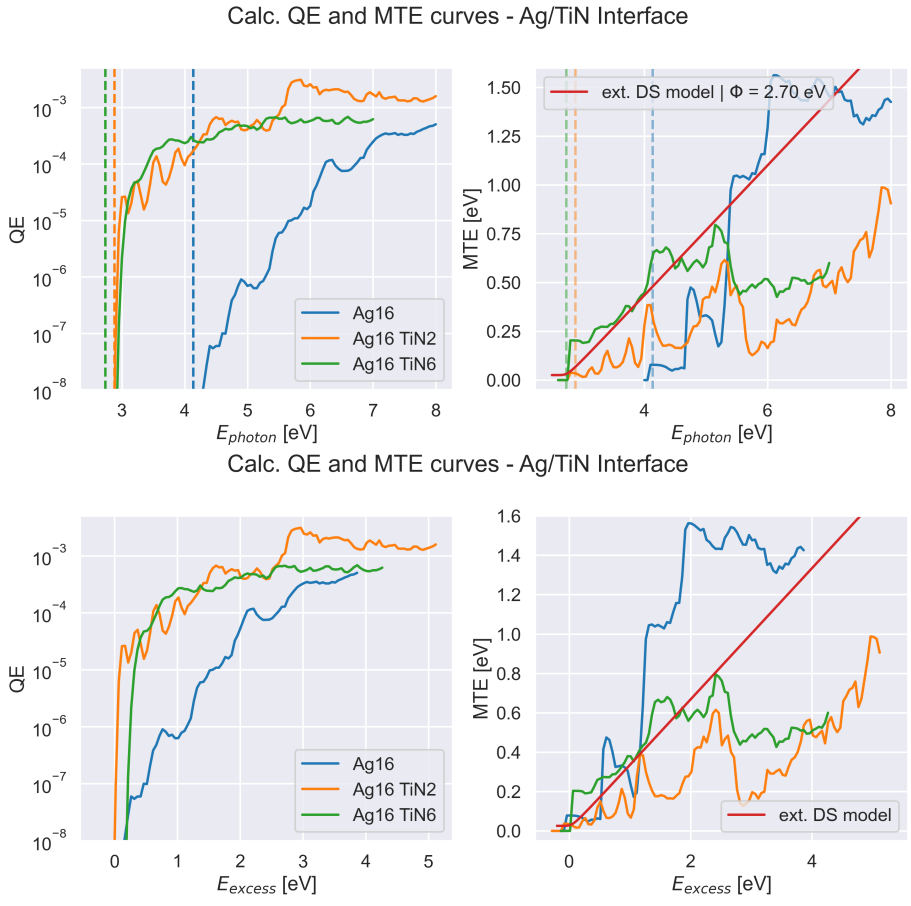


Figure 5.36: Calculated QE and MTE curves for the Ag/TiN interfaces.

when comparing to the bare metal slab. The origin of the work function change is due to the interaction between the metal substrate surface and the thin film. A theoretical study by Prada, Martinez and Pacchioni [181] links the work function changes to a change in the surface dipole. The dipole can be influenced by a charge transfer between materials, compression of the electrons spilling out of the metal surface, and finally the metallic surface having the possibility of partially reconstructing due to the presence of the lattice mismatched thin film. The strength of each of these depend on the exact material the thin film is made of [181].

The reduction of work function has obvious benefits to the use of the material stack as a photocathode. With a lowered emission threshold the QE for a given photon energy is increased. It is also possible that wavelengths with no meaningful QE for a higher workfunction cathode are able to produce useable emission probabilities from the lowered photocathode interface. Longer wavelengths, such as visible wavelengths compared to UV, are generally more easily produced and have less requirements for the optical elements to guide the drive laser. This means a lowering of the work function can potentially simplify the equipment necessary to drive the photocathode for an accelerator.

Secondly, the surface's DOS is modified by the presence of the thin film's electronic states. The flat valence bands from the exemplary MgO film significantly increase the emission contributions with low transverse momentum near their emission threshold. This in turn reduces the overall MTE value, which is a desirable change and demonstrates a possible approach to tune a material's emission characteristics. By changing the electronic structure through deposition or causing a reconstruction in the surface or material through strain, the photoemission response can be changed favourably and the the photocathode be tuned.

Finally, the deposition of a small amount of material can protect the photocathode's surface. By separating the photoactive material from the environment, reactive materials with good photoemission characteristics can have improved stability and thus longevity. While in this thesis transition metal oxides and nitrides are demonstrated, publications also show the option of using graphene [35] or MoS_2 [15] as isolation layers. While the examples in this thesis show improvements to photocathode performance, the thin film's impact on electron emission probability through scattering and other processes must be carefully considered.

6 Conclusion

Within this work a photoemission model for calculation of photoemission (PE) from explicit surface models is described and systems of interest for use as electron sources in free electron lasers (FELs) are studied in detail. These include metallic materials, such as the low index Cu(100,110,111) surfaces and Ag(100), which are representative of low quantum efficiency (QE), but robust cathode materials used in initial FEL designs. The heterogenous interfaces considered are of MgO(100) on Ag(100) and Cu(100), as well as TiN(100) on the Ag(100) surface, and represent protective films for modern photocathode applications. The class of semiconductors as photocathodes has not been included in the calculations of PE spectra, but the model is capable of producing PE spectra for this class of materials, as well.

The calculated PE spectra for Cu surfaces are compared to experimentally measured MTE spectra. The spectra were measured by our collaborators using the TESS instrument in the photocathode group within ASTeC at the STFC Daresbury laboratory. A reasonable agreement between the calculated and measured spectra is observed. It is notable that models assuming indirect (non-electron momentum conserving) transitions show much better alignment with the experimental spectrum. The spectra calculated using OptaDOS photoemission only consider direct transitions and show a lot more features in the spectrum, such as periodic oscillations. These features can be associated with using discrete states rather than a semi-continuous density. The electronic structure of a surface slab model with a finite number of layers has a number of these discrete states. Using these for the emission calculation can then result in the oscillations. One has to balance the goal of creating a model with as many discrete states as possible with the computational demands of very large surface models. Further, it is shown, that by increasing the number of layers in the surface model, the response spectrum is smoothed out. This, however, has the unintended consequence of lowering the calculated emission probability.

The ability to use the PE model on supercell geometries is demonstrated, which are essential for the description of surface adsorbate systems and lattice matched interfaces. Furthermore, the detailed analysis of contributions to the overall QE and MTE spectra carried out. The clear link between emission from a set of high density of states with little transverse momentum to lowering the MTE in the spectrum is established and showcases the advantages of the discussed photoemission model. The model implemented as a computational toolchain will be available as part of the CASTEP plane wave density functional theory (PW-DFT) package to calculate the electronic structure and matrix elements and the open-source OptaDOS tool is used to calculate the optical properties PE spectra. This thesis represents the development of a tool to help interpret experimental data from photoemission experiments and help guide development of better photocathodes in the future.

6.1 Further Work

As discussed throughout this work, a number of challenges remain. First, the calculation of the free electron OME naively assumes the transverse momentum for the excitation to be equal to the transverse $\mathbf{k}_{\parallel}$ point. The "folding" of bands in supercells, however, makes this naive association scheme incorrect. The *Gkgrid* approach is able to give comparable results for the emission probability between PC and SC systems. This means any emission from a folded band is correctly treated, but the excitation probability is not.

Secondly, the *Gkgrid* approach for super-cell (SC) systems has shown to change the relative emission intensities for the emitting states. This is most evident in the suppression of calculated emission intensity from flat d like states near the Γ point in Figure 5.8. The origin of this relative change of calculated emission probability is not currently known and understanding this would allow a user to better compare the results from the *Gkgrid* approach to the *crystal* approach.

Further, the symmetry reduction of the MP grid means, that the calculation of $E_{kinetic}$ vs $p_{\parallel}$ ARPES maps can have missing parts of the spectrum. When the entire range of the emission

angle ϕ is included, this does not matter as all contributions are included, but when limiting ϕ this can become apparent, such as in Figure 5.8. An approach to reverse the symmetry reduction by applying the symmetry element matrices is implemented for some ARPES map calculations, but not for the $E_{kinetic}$ vs $p_{\parallel}$ ARPES map.

The unexpected suppression of the QE response spectrum for a surface slab model with large number of layers will have to be investigated in the future. The exact origin of this behaviour is currently unknown.

Calculating the electron mean free path as a function of electron energy is non-trivial and it has has proven difficult to find am approach suitable for the photon energy ranges of interest. Further work is necessary to find a general approach, which does not rely on experimental data or the fitting of spectra. One such possible approach is the electron loss function, which can be calculated within OptaDOS as an energy dependent quantity directly from the DFT electronic structure. This function describes the probability of an electron-electron scattering event due to electronic excitations. This means, that other possible scattering mechanisms, such as phonons or surface features, are not included, but it would improve on the currently used approach of a user defined spectroscopic constant approach.

Finally the assumption is made in OptaDOS, that the incoming light has normal incidence, so refraction effects at the surface is neglected. The resulting changes in the light propagation direction and polarisation direction are omitted. This normal incidence geometry, however, is normally not used in experimental setups, as the light and the electronic analyser would need to occupy the same space. The light is shone onto the surface at an angle of $< 90°$. While OptaDOS includes the ability to change the polarisation vector for the incoming light, being able to represent incidences away from the surface normal and the resulting polarisation vector changes would allow for better comparisons between experimental data and the spectra predicted by the PE model.

References

[1] A. Claudet, *PHOTOGRAPHIC MINIATURE. TO THE EDITOR OF THE SPECTATOR*, Electronic Article, 1841 (see p. 16).

[2] J. M. Eder, Knapp, Halle (Saale), FOURTH, 1932 (see p. 16).

[3] *Datasheet PHANTOM TMX Series*, Catalog, 2025 (see p. 16).

[4] E. Muybridge, *The horse in motion, illus. by Muybridge. "Sallie Gardner," owned by Leland Stanford, running at a 1:40 gait over the Palo Alto track, 19 June 1878: 2 frames showing diagram of foot movements*, Online Multimedia, 1878 (see p. 16).

[5] S. Boutet, L. Lomb, G. J. Williams et al., *Science*, 2012, **337**, 362 (see p. 16).

[6] A. Rudenko and D. Rolles, *Journal of Electron Spectroscopy and Related Phenomena*, 2015, **204**, 228 (see p. 16).

[7] K. Baumgärtner, M. Reuner, C. Metzger et al., *Nature Communications*, 2022, **13**, DOI: 10.1038/s41467-022-30404-6 (see p. 16).

[8] A. Hofmann, *The physics of synchrotron radiation*, Cambridge university press, 2004, vol. 20 (see p. 16).

[9] D. H. Dowell, I. Bazarov, B. Dunham et al., *Nuclear Instruments and Methods in Physics Research Section A: Accelerators, Spectrometers, Detectors and Associated Equipment*, 2010, **622**, 685 (see p. 17).

[10] P. Musumeci, J. Giner Navarro, J. B. Rosenzweig et al., *Nuclear Instruments and Methods in Physics Research Section A: Accelerators, Spectrometers, Detectors and Associated Equipment*, 2018, **907**, 209 (see pp. 17, 19, 20).

[11] B. Camino, Thesis, 2017 (see pp. 17, 70, 96).

[12] V. C. Lee, Thesis, 2021 (see p. 17).

[13] H. Motz, *Journal of Applied Physics*, 1951, **22**, 527 (see p. 17).

[14] J. M. J. Madey, *Journal of Applied Physics*, 1971, **42**, 1906 (see p. 17).

[15] J. Schaber, R. Xiang and N. Gaponik, *Journal of Materials Chemistry C*, 2023, **11**, 3162 (see pp. 17, 20, 43, 107).

[16] P. Michel, H. Buettig, F. Gabriel et al., Proc. FEL, p. 488 (see p. 17).

[17] C. Pellegrini, *The European Physical Journal H*, 2012, **37**, 659 (see pp. 17–19).

[18] C. M. Pierce, M. B. Andorf, E. Lu et al., *Physical Review Accelerators and Beams*, 2020, **23**, DOI: 10.1103/PhysRevAccelBeams.23.070101 (see pp. 17, 20).

[19] J. Rönsch-Schulenburg, E. Hass, A. Kuhl et al., *Short SASE-FEL Pulses at FLASH*, 2013, pp. 379–382 (see p. 17).

[20] L. Monaco, D. Sertore, M. Baylac et al., *arXiv preprint arXiv:2304.09951*, 2023 (see p. 17).

[21] M. Ferrario, *Proc. EPAC'06*, 2006, 2733 (see p. 17).

[22] B. D. Patterson and R. Abela, *Physical Chemistry Chemical Physics*, 2010, **12**, 5647 (see pp. 17, 18).

[23] Z. Huang and K.-J. Kim, *Physical Review Special Topics - Accelerators and Beams*, 2007, **10**, 034801 (see p. 18).

[24] C. Patel, *IEEE Journal of Quantum Electronics*, 1984, **20**, 561 (see p. 18).

[25] T. H. Johnson and I. Hunter, Allen M., *Journal of Applied Physics*, 1980, **51**, 2406 (see p. 18).

[26] F. P. Schäfer, *Dye lasers*, Springer-Verlag, Berlin ; Third, 1990 (see p. 18).

[27] V. Ayvazyan, N. Baboi, J. Bähr et al., *The European Physical Journal D - Atomic, Molecular, Optical and Plasma Physics*, 2006, **37**, 297 (see p. 19).

[28] D. Reschke and D. Hamburg, *SFR, Canada, USA*, 2015, **2015** (see p. 19).

[29] P. Emma and L. C. Team, *Proceedings of PAC09, Vancouver, to be published in http://accelconf. web. cern. ch/AccelConf*, 2009 (see p. 19).

[30] K. Togawa, T. Hara and H. Tanaka, *Physical Review Special Topics - Accelerators and Beams*, 2009, **12**, 080706 (see p. 19).

[31] A. Todd, *Nuclear Instruments and Methods in Physics Research Section A: Accelerators, Spectrometers, Detectors and Associated Equipment*, 2006, **557**, 36 (see p. 19).

[32] R. Xiang and J. Schaber, *Micromachines*, 2022, **13**, 1241 (see p. 20).

[33] C. T. Parzyck, A. Galdi, J. K. Nangoi et al., *Physical Review Letters*, 2022, **128**, 114801 (see pp. 20, 43).

[34] C. Benjamin, R. Valizadeh, H. M. Churn, L. B. Jones and T. C. Q. Noakes, *RUBIDIUM TELLURIDE PHOTOCATHODES FOR HIGH QUANTUMEFFICIENCY AND LOW MEAN TRANSVERSE ENERGY ACCELERATORAPPLICATIONS*, Conference Paper, 2024 (see p. 20).

[35] C. J. Knill, H. Yamaguchi, K. Kawahara et al., *Physical Review Applied*, 2023, **19**, DOI: 10.1103/PhysRevApplied.19.014015 (see pp. 20, 43, 107).

[36] Y. Zhang, J. Zhan, S. Li et al., *Journal of Materials Research and Technology*, 2022, **21**, 3767 (see pp. 20, 43).

[37] J. Biswas, M. Gaowei, A. Liu et al., *APL Materials*, 2022, **10**, DOI: 10.1063/5.0122937 (see pp. 20, 43).

[38] V. Chang, T. C. Q. Noakes and N. M. Harrison, *Physical Review B*, 2018, **97**, DOI: 10.1103/physrevb.97.155436 (see pp. 20, 95).

[39] S. Karkare, *Photoemission and Bright Beams Lab - Experimental Facility*, Web Page (see p. 20).

[40] L. B. Jones, H. Panuganti, C. Benjamin et al., *Physical Review Accelerators and Beams*, 2024, **27**, 023402 (see p. 20).

[41] R. Schier, H.-D. Saßnick and C. Cocchi, *Physical Review Materials*, 2022, **6**, 125001 (see p. 21).

[42] R. Schier, D. Guo, H.-D. Saßnick and C. Cocchi, *Advanced Theory and Simulations*, 2024, **7**, DOI: 10.1002/adts.202400680 (see p. 21).

[43] P. Schindler, E. R. Antoniuk, G. Cheon, Y. Zhu and E. J. Reed, "Discovery of materials with extreme work functions by high-throughput densityfunctional theory and machine learning", Unpublished Work, 2020 (see p. 21).

[44] H.-D. Saßnick and C. Cocchi, *npj Computational Materials*, 2024, **10**, 38 (see p. 21).

[45] P. Saha, O. Chubenko, J. Kevin Nangoi et al., *Journal of Applied Physics*, 2023, **133**, DOI: 10.1063/5.0135629 (see pp. 21, 36, 43, 84).

[46] E. R. Antoniuk, Y. Yue, Y. Zhou et al., *Physical Review B*, 2020, **101**, 235447 (see pp. 21, 38, 39).

[47] P. Puschnig and D. Lüftner, *Journal of Electron Spectroscopy and Related Phenomena*, 2015, **200**, 193 (see pp. 21, 41, 42, 56).

[48] W. A. Schroeder, *Ultrafast Sub-threshold One-photon Photoemission*, Generic, 2022 (see p. 21).

[49] E. R. Antoniuk, P. Schindler, W. A. Schroeder et al., *Advanced Materials*, 2021, **33**, 2104081 (see p. 21).

[50] H.-D. Saßnick and C. Cocchi, *Advanced Theory and Simulations*, 2025, **8**, DOI: 10.1002/adts.202401344 (see p. 21).

[51] L. Hedin, *Physical Review*, 1965, **139**, A796 (see p. 21).

[52] E. Schrödinger, *Annalen der Physik*, 1926, **384**, 361 (see p. 22).

[53] E. Schrödinger, *Physical Review*, 1926, **28**, 1049 (see p. 22).

[54] A. Szabo and N. Ostlund, *Modern Quantum Chemistry: Introduction to Advanced Electronic Structure Theory*, Dover Publications, 1996 (see pp. 22, 23).

[55] M. Born and R. Oppenheimer, *Annalen der Physik*, 1927, **389**, 457 (see p. 22).

[56] D. R. Hartree, *Mathematical Proceedings of the Cambridge Philosophical Society*, 1928, **24**, 89 (see pp. 23, 24).

[57] V. Fock, *Zeitschrift für Physik*, 1930, **61**, 126 (see p. 23).

[58] R. M. Martin, *Electronic Structure: Basic Theory and Practical Methods*, Cambridge University Press, Cambridge, 2004 (see pp. 23–25).

[59] P. Hohenberg and W. Kohn, *Physical Review*, 1964, **136**, B864 (see p. 23).

[60] W. Kohn and L. J. Sham, *Physical Review*, 1965, **140**, A1133 (see p. 23).

[61] J. P. Perdew and K. Burke, *International Journal of Quantum Chemistry*, 1996, **57**, 309 (see p. 25).

[62] J. P. Perdew, K. Burke and M. Ernzerhof, *Physical Review Letters*, 1996, **77**, 3865 (see p. 25).

[63] J. P. Perdew, A. Ruzsinszky, G. I. Csonka et al., *Physical Review Letters*, 2008, **100**, 136406 (see pp. 25, 72).

[64] H.-D. Saßnick and C. Cocchi, *Electronic Structure*, 2021, **3**, 027001 (see p. 25).

[65] P. Haas, F. Tran, P. Blaha, K. Schwarz and R. Laskowski, *Physical Review B*, 2009, **80**, 195109 (see pp. 25, 26).

[66] A. J. Garza and G. E. Scuseria, *The Journal of Physical Chemistry Letters*, 2016, **7**, 4165 (see p. 25).

[67] J. Heyd, G. E. Scuseria and M. Ernzerhof, *The Journal of Chemical Physics*, 2003, **118**, 8207 (see p. 25).

[68] C. Adamo and V. Barone, *The Journal of Chemical Physics*, 1999, **110**, 6158 (see p. 25).

[69] W. Gao, T. A. Abtew, T. Cai et al., *Solid State Communications*, 2016, **234-235**, 10 (see p. 25).

[70] J. Paier, M. Marsman, K. Hummer et al., *The Journal of Chemical Physics*, 2006, **124**, 154709 (see p. 25).

[71] F. Jensen, *Introduction to computational chemistry*, John Wiley and Sons, Chichester, England ; SECOND, 2007 (see p. 26).

[72] M. D. Segall, P. J. D. Lindan, M. J. Probert et al., *Journal of Physics: Condensed Matter*, 2002, **14**, 2717 (see pp. 26–28).

[73] S. J. Clark, M. D. Segall, C. J. Pickard et al., *Zeitschrift für Kristallographie - Crystalline Materials*, 2005, **220**, 567 (see pp. 27, 28, 30, 56, 65, 93).

[74] D. Vanderbilt, *Physical Review B*, 1990, **41**, 7892 (see p. 27).

[75] C. Lee, D. Vanderbilt, K. Laasonen, R. Car and M. Parrinello, *Physical Review B*, 1993, **47**, 4863 (see p. 27).

[76] C. Pickard, *On-the-fly pseudopotential generation in CASTEP*, Manuscript, 2006 (see pp. 28, 47, 72).

[77] D. J. Chadi and M. L. Cohen, *Physical Review B*, 1973, **7**, 692 (see p. 28).

[78] G. Gilat, *Journal of Computational Physics*, 1972, **10**, 432 (see p. 28).

[79] H. J. Monkhorst and J. D. Pack, *Physical Review B*, 1976, **13**, 5188 (see p. 28).

[80] J. D. Pack and H. J. Monkhorst, *Physical Review B*, 1977, **16**, 1748 (see p. 28).

[81] A. J. Morris, R. J. Nicholls, C. J. Pickard and J. R. Yates, *Computer Physics Communications*, 2014, **185**, 1477 (see pp. 28–30, 48, 49, 69, 74).

[82] A. J. Morris, R. J. Nicholls, C. J. Pickard and J. R. Yates, *Computer Physics Communications*, 2012 (see p. 28).

[83] R. J. Nicholls, A. J. Morris, C. J. Pickard and J. R. Yates, *Journal of Physics: Conference Series*, 2012, **371**, 012062 (see p. 28).

[84] M. D. Segall, C. J. Pickard, R. Shah and M. C. Payne, *Molecular Physics*, 1996, **89**, 571 (see pp. 29, 50).

[85] J. E. Müller and J. W. Wilkins, *Physical Review B*, 1984, **29**, 4331 (see p. 30).

[86] J. Hook and H. Hall, *Solid State Physics*, Wiley, 2013 (see pp. 30, 50, 72).

[87] A. Einstein, *Ann. Phys*, 1905, **17**, 4 (see p. 32).

[88] C. N. Berglund and W. E. Spicer, *Physical Review*, 1964, **136**, A1030 (see pp. 32–34, 84).

[89] C. N. Berglund and W. E. Spicer, *Physical Review*, 1964, **136**, A1044 (see p. 32).

[90] A. Damascelli, *Physica Scripta*, 2004, **2004**, 61 (see p. 32).

[91] D. H. Dowell, F. K. King, R. E. Kirby, J. F. Schmerge and J. M. Smedley, *Physical Review Special Topics - Accelerators and Beams*, 2006, **9**, 063502 (see pp. 32, 34).

[92] D. H. Dowell and J. F. Schmerge, *Physical Review Special Topics - Accelerators and Beams*, 2009, **12**, 074201 (see pp. 32, 34–36, 39).

[93] J. F. Schmerge, J. M. Castro, D. H. Dowell et al., *International Free-Electron Laser Conference*, 2004, 205 (see p. 34).

[94] R. H. Fowler, *Physical Review*, 1931, **38**, 45 (see p. 35).

[95] T. Vecchione, D. H. Dowell, W. Wan, J. Feng and H. A. Padmore, FEL 2013 (see pp. 36, 74, 75, 80, 81, 84, 86).

[96] M. Gajdoš, K. Hummer, G. Kresse, J. Furthmüller and F. Bechstedt, *Physical Review B*, 2006, **73**, 045112 (see p. 39).

[97] I. Adawi, *Physical Review*, 1964, **134**, A788 (see p. 40).

[98] G. D. Mahan, *Physical Review B*, 1970, **2**, 4334 (see p. 40).

[99] C. Caroli, D. Lederer-Rozenblatt, B. Roulet and D. Saint-James, *Physical Review B*, 1973, **8**, 4552 (see p. 40).

[100] A. Liebsch, *Physical Review Letters*, 1974, **32**, 1203 (see p. 40).

[101] J. B. Pendry, *Surface Science*, 1976, **57**, 679 (see p. 40).

[102] J. F. L. Hopkinson, J. B. Pendry and D. J. Titterington, *Computer Physics Communications*, 1980, **19**, 69 (see p. 40).

[103] S. Karkare and I. Bazarov, *Applied Physics Letters*, 2011, **98**, 094104 (see pp. 40, 41).

[104] P. O. Nilsson, J. Kanski and C. G. Larsson, *Solid State Communications*, 1980, **36**, 111 (see p. 41).

[105] P. Puschnig, S. Berkebile, A. J. Fleming et al., *Science*, 2009, **326**, 702 (see pp. 41, 42, 56).

[106] D. Lüftner, S. Weiß, X. Yang et al., *Physical Review B*, 2017, **96**, DOI: 10.1103/PhysRevB.96.125402 (see pp. 41, 42).

[107] W. A. Schroeder and G. Adhikari, *New Journal of Physics*, 2019, **21**, DOI: 10.1088/1367-2630/ab0ce2 (see p. 43).

[108] E. R. Antoniuk, Thesis, 2021 (see p. 43).

[109] J. K. Nangoi, S. Karkare, R. Sundararaman, H. A. Padmore and T. A. Arias, *Physical Review B*, 2021, **104**, DOI: 10.1103/PhysRevB.104.115132 (see p. 43).

[110] W. Liu, Y. Chen, W. Lu et al., *Applied Physics Letters*, 2016, **109**, 252104 (see p. 43).

[111] Z. Shu, Y. Zhang, L. Ren et al., *Optik*, 2021, **232**, 166555 (see p. 43).

[112] C. J. Fall, N. Binggeli and A. Baldereschi, *Journal of Physics: Condensed Matter*, 1999, **11**, 2689 (see p. 44).

[113] S. Hüfner, *Photoelectron Spectroscopy*, Springer Berlin, Heidelberg, Third, 2003, pp. XV, 662 (see pp. 47, 56).

[114] A. F. Starace, *Physical Review A*, 1971, **3**, 1242 (see p. 47).

[115] O. Rubel and P. Blaha, *Computation*, 2022, **10**, DOI: 10.3390/computation10020022 (see p. 47).

[116] M. S. Hybertsen and S. G. Louie, *Phys Rev B Condens Matter*, 1987, **35**, 5585 (see pp. 47, 48).

[117] A. J. Read and R. J. Needs, *Phys Rev B Condens Matter*, 1991, **44**, 13071 (see p. 47).

[118] M. Dressel and G. Grüner, *Electrodynamics of Solids: Optical Properties of Electrons in Matter*, Cambridge University Press, Cambridge, 2002 (see p. 48).

[119] C. J. Pickard, Thesis, 1997 (see p. 49).

[120] A. J. Morris, R. J. Nicholls, C. J. Pickard and J. R. Yates, *OptaDOS User Guide 1.2*, Online Multimedia, 2015 (see pp. 49, 74).

[121] P. W. Atkins and J. De Paula, *Atkins' Physical chemistry*, Oxford University Press, Oxford, United Kingdom, Ninth edition., 2010 (see p. 50).

[122] D. Sanchez-Portal, E. Artacho and J. M. Soler, *Solid State Communications*, 1995, **95**, 685 (see p. 50).

[123] N. Marzari, A. A. Mostofi, J. R. Yates, I. Souza and D. Vanderbilt, *Reviews of Modern Physics*, 2012, **84**, 1419 (see p. 50).

[124] S.-P. Daniel, A. Emilio and M. S. José, *Journal of Physics: Condensed Matter*, 1996, **8**, 3859 (see p. 50).

[125] J. Aarons, L. G. Verga, N. D. M. Hine and C. K. Skylaris, *Electronic Structure*, 2019, **1**, 035002 (see p. 50).

[126] S. Tanuma, C. J. Powell and D. R. Penn, *Surface and Interface Analysis*, 1991, **17**, 911 (see pp. 52, 54).

[127] S. Tanuma, C. J. Powell and D. R. Penn, *Surface and Interface Analysis*, 2003, **35**, 268 (see pp. 52, 54).

[128] I. Nagy and P. M. Echenique, *Physical Review B*, 2012, **85**, 115131 (see pp. 52–54).

[129] J. D. Bourke and C. T. Chantler, *Physical Review Letters*, 2010, **104**, 206601 (see p. 53).

[130] B. Ziaja, R. A. London and J. Hajdu, *Journal of Applied Physics*, 2006, **99**, DOI: 10.1063/1.2161821 (see p. 53).

[131] S. Hüfner, in *Photoelectron Spectroscopy: Principles and Applications*, ed. S. Hüfner, Springer Berlin Heidelberg, Berlin, Heidelberg, 2003, ch. Chapter 6, pp. 347–409 (see p. 55).

[132] K. L. Jensen, D. W. Feldman and P. G. O'Shea, *Applied Physics Letters*, 2004, **85**, 5448 (see p. 56).

[133] H. I. Starnberg, H. E. Brauer and P. O. Nilsson, *Physical Review B*, 1993, **48**, 621 (see p. 56).

[134] J. Feng, J. Nasiatka, W. Wan et al., *Applied Physics Letters*, 2015, **107**, DOI: 10.1063/1.4931976 (see p. 56).

[135] S. Karkare, G. Adhikari, W. A. Schroeder et al., *Physical Review Letters*, 2020, **125**, 054801 (see p. 56).

[136] K. L. Jensen, P. G. O'Shea and D. W. Feldman, *Physical Review Special Topics - Accelerators and Beams*, 2010, **13**, 080704 (see p. 56).

[137] G. Koller, S. Berkebile, M. Oehzelt et al., *Science*, 2007, **317**, 351 (see p. 56).

[138] L. W. Nordheim, *Proceedings of the Royal Society of London. Series A, Containing Papers of a Mathematical and Physical Character*, 1928, **121**, 626 (see p. 58).

[139] R. G. Forbes and J. H. B. Deane, *Proceedings of the Royal Society A: Mathematical, Physical and Engineering Sciences*, 2007, **463**, 2907 (see pp. 58–60).

[140] J. H. B. Deane and R. G. Forbes, *Journal of Physics A: Mathematical and Theoretical*, 2008, **41**, DOI: 10.1088/1751-8113/41/39/395301 (see p. 58).

[141] R. G. Forbes, *Journal of Applied Physics*, 2008, **103**, DOI: 10.1063/1.2937077 (see pp. 58, 59).

[142] W. Schottky, *Physikalische Zeitschrift*, 1914, **15**, 872 (see p. 58).

[143] R. G. Forbes, *Applied Physics Letters*, 2006, **89**, 113122 (see p. 60).

[144] W. Ku, T. Berlijn and C. C. Lee, *Phys Rev Lett*, 2010, **104**, 216401 (see p. 65).

[145] I. Deretzis, G. Calogero, G. G. N. Angilella and A. La Magna, *EPL (Europhysics Letters)*, 2014, **107**, DOI: 10.1209/0295-5075/107/27006 (see p. 65).

[146] B. Zhu, S. R. Kavanagh and D. Scanlon, *Journal of Open Source Software*, 2024, **9**, DOI: https://doi.org/10.21105/joss.05974 (see p. 65).

[147] M. Chen and M. Weinert, *Physical Review B*, 2018, **98**, DOI: 10.1103/PhysRevB.98.245421 (see p. 65).

[148] T. Kosugi, H. Nishi, Y. Kato and Y.-i. Matsushita, *Journal of the Physical Society of Japan*, 2017, **86**, 124717 (see p. 65).

[149] S. G. Mayo, F. Yndurain and J. M. Soler, *Journal of Physics: Condensed Matter*, 2020, **32**, 205902 (see p. 65).

[150] Valgrind Developers, *Valgrind*, Web Page, 2025 (see p. 70).

[151] A. Terekhov, H. Scheibler, B. Militsyn et al., *Cockcroft Preprints*, 2013 (see pp. 72, 74, 75, 80, 81, 84, 86, 100, 102).

[152] L. B. Jones, D. P. Juarez-Lopez, H. E. Scheibler et al., *Rev Sci Instrum*, 2022, **93**, 113314 (see pp. 72, 74, 75, 80, 81, 84, 86, 100, 102).

[153] M. K. Horton, P. Huck, R. X. Yang et al., *Nature Materials*, 2025, **24**, 1522 (see pp. 72, 89, 93, 94).

[154] R. H. Byrd, J. Nocedal and R. B. Schnabel, *Mathematical Programming*, 1994, **63**, 129 (see p. 73).

[155] W. P. Davey, *Physical Review*, 1925, **25**, 753 (see p. 73).

[156] N. K. Nepal, S. Adhikari, J. E. Bates and A. Ruzsinszky, *Physical Review B*, 2019, **100**, 045135 (see p. 73).

[157] W. C. Overton and J. Gaffney, *Physical Review*, 1955, **98**, 969 (see p. 73).

[158] G. I. Csonka, J. P. Perdew, A. Ruzsinszky et al., *Physical Review B*, 2009, **79**, 155107 (see p. 73).

[159] S. P. Ong, W. D. Richards, A. Jain et al., *Computational Materials Science*, 2013, **68**, 314 (see pp. 73, 90, 95, 100, 104).

[160] G. N. Derry, M. E. Kern and E. H. Worth, *Journal of Vacuum Science and Technology A*, 2015, **33**, DOI: 10.1116/1.4934685 (see pp. 74, 80, 84).

[161] P. O. Gartland, S. Berge and B. J. Slagsvold, *Physical Review Letters*, 1972, **28**, 738 (see pp. 74, 80, 84).

[162] A. Patra, J. E. Bates, J. Sun and J. P. Perdew, *Proc Natl Acad Sci U S A*, 2017, **114**, E9188 (see pp. 74, 80, 84).

[163] C. J. Knill, S. S. Karkare and H. A. Padmore, 12th Int. Particle Acc. Conf. JACoW Publishing (see p. 85).

[164] L. A. Angeloni, I. J. Shan and W. A. Schroeder, *AIP Advances*, 2022, **12**, DOI: 10.1063/5.0099779 (see p. 85).

[165] V. A. Lubarda, *Mechanics of Materials*, 2003, **35**, 53 (see p. 89).

[166] A. Ambrosetti and P. L. Silvestrelli, *Physical Review B*, 2016, **94**, 045124 (see p. 89).

[167] C. D. Group, *Spectral - Keywords*, Web Page, 2023 (see p. 93).

[168] V. I. Anisimov, J. Zaanen and O. K. Andersen, *Physical Review B*, 1991, **44**, 943 (see p. 93).

[169] A. I. Liechtenstein, V. I. Anisimov and J. Zaanen, *Physical Review B*, 1995, **52**, R5467 (see p. 93).

[170] V. I. Anisimov, F. Aryasetiawan and A. I. Lichtenstein, *Journal of Physics: Condensed Matter*, 1997, **9**, 767 (see p. 93).

[171] M. O. Lynn, D. Ologunagba, B. B. Dangi and S. Kattel, *Physical Chemistry Chemical Physics*, 2023, **25**, 5156 (see p. 94).

[172] F. D. Murnaghan, *Proceedings of the National Academy of Sciences*, 1944, **30**, 244 (see p. 94).

[173] A. Hjorth Larsen, J. Jørgen Mortensen, J. Blomqvist et al., *Journal of Physics: Condensed Matter*, 2017, **29**, 273002 (see p. 94).

[174] C. L. Fu and K. M. Ho, *Physical Review B*, 1983, **28**, 5480 (see p. 94).

[175] S. Heo, E. Cho, H.-I. Lee et al., *AIP Advances*, 2015, **5**, DOI: 10.1063/1.4927547 (see p. 94).

[176] V. Begum, M. E. Gruner, C. Vorwerk, C. Draxl and R. Pentcheva, *Physical Review B*, 2021, **103**, 195128 (see p. 94).

[177] W. Lengauer, *Journal of Alloys and Compounds*, 1992, **186**, 293 (see pp. 94, 95).

[178] K. Chen, L. R. Zhao, J. Rodgers and J. S. Tse, *Journal of Physics D: Applied Physics*, 2003, **36**, 2725 (see p. 95).

[179] T.-R. Shan, B. D. Devine, S. R. Phillpot and S. B. Sinnott, *Physical Review B*, 2011, **83**, 115327 (see pp. 96, 101, 105).

[180] A. Zur and T. C. McGill, *Journal of Applied Physics*, 1984, **55**, 378 (see p. 100).

[181] S. Prada, U. Martinez and G. Pacchioni, *Physical Review B*, 2008, **78**, DOI: 10.1103/physrevb.78.235423 (see p. 107).

A Output from a Photoemission Calculation

The following lines are taken from the output file of a photoemission calculation of a Cu(100) slab with 16 layers to represent. The surface model is identical to the one described in Section 5.3.2.

The following output is the QE and MTE specific section from a 3-Step calculation:

```
+-------------------------------------------------------------------------+
| Work Function              4.6095 eV         Photon Energy     5.0000 eV   |
| Effective Work Function    4.6095 eV         Electric Field    0.0000 V/A  |
| Final State : Bloch State                                                 |
+-------------------------------------------------------------------------+
| Atom |  Atom Order  |   Layer   |             Quantum Efficiency           |
|  Cu          1            1                     0.2707E-005              |
|  Cu          2            2                     0.2468E-018              |
|  Cu          3            3                     0.1084E-006              |
|  Cu          4            4                     0.2403E-006              |
|  Cu          5            5                     0.3335E-006              |
|  Cu          6            6                     0.2204E-006              |
|  Cu          7            7                     0.1068E-006              |
|  Cu          8            8                     0.3187E-007              |
| Bulk                                            0.8486E-007              |
| Total Quantum Efficiency (electrons/photon):         0.3833E-005          |
| Weighted Mean Transverse Energy (eV):                0.9447E-001          |
+-------------------------------------------------------------------------+
```

The following output is the QE and MTE specific section from a 1-Step calculation:

```
+-------------------------------------------------------------------------+
| Work Function              4.6095 eV         Photon Energy     5.0000 eV   |
| Effective Work Function    4.6095 eV         Electric Field    0.0000 V/A  |
| Final State : Free Electron State                                         |
+-------------------------------------------------------------------------+
| Atom |  Atom Order  |   Layer   |             Quantum Efficiency           |
|  Cu          1            1                     0.7227E-007              |
|  Cu          2            2                     0.3858E-026              |
|  Cu          3            3                     0.2867E-008              |
|  Cu          4            4                     0.6335E-008              |
|  Cu          5            5                     0.8768E-008              |
|  Cu          6            6                     0.5784E-008              |
|  Cu          7            7                     0.2790E-008              |
|  Cu          8            8                     0.8288E-009              |
| Bulk                                            0.1811E-008              |
| Total Quantum Efficiency (electrons/photon):         0.1015E-006          |
| Weighted Mean Transverse Energy (eV):                0.9766E-001          |
+-------------------------------------------------------------------------+
```